$CD4^+$ T cells promote renal fibrosis after acute kidney injury

Dissertation

for the acquisition of the Doctorate of Natural Sciences (Dr. rer. nat.)

Faculty of Mathematics, Informatics and Natural Sciences
Department of Biology
University of Hamburg

Lena Henneken

Hamburg, 2025

This work has been conducted in the research groups and under the guidance of Prof. Dr. med. Jan-Eric Turner and Prof. Dr. med. Ulf Panzer at the III. Department of Medicine of the University Medical Center Hamburg-Eppendorf.

Reviewers

1st Reviewer: **Prof. Dr. Wolfgang Streit**, University of Hamburg, Institute for Plant Science and Microbiology, Department of Biology

2nd Reviewer: **Prof. Dr. med. Jan-Eric Turner**, University Medical Center Hamburg-Eppendorf, III. Department of Medicine

Committee Members

Chairman of committee: Prof. Dr. Tobias Lenz

Deputy chairman of committee: Prof. Dr. Wolfgang Streit

3rd Member: Prof. Dr. Jan-Eric Turner

4th Member: Prof. Dr. Ulf Panzer

Date of disputation

21.05.2026

I hereby confirm that this doctoral thesis is identical in all additionally printed copies with the copies of the thesis submitted to the faculty and in electronic form via Docata.

Hamburg, 10.09.2025

Lena Henneken

Table of contents

1 Summary

Acute kidney injury (AKI) is a syndrome defined by a sudden decrease in kidney function, primarily manifesting in impaired glomerular filtration [1]. In high-income countries, AKI constitutes a major challenge for the health care system. Although kidney function impairment clinically resolves in most cases of AKI, emerging evidence indicates that AKI frequently leads to long-term structural damage within the kidney parenchyma, resulting in an increased risk for development of chronic kidney disease (CKD), a leading cause of global mortality [2]. Despite recent research efforts, immunological mechanisms underlying AKI to CKD progression are still incompletely understood and effective therapeutic interventions to attenuate this progression are still lacking [3].
To investigate the role of the immune system in progression of AKI to CKD, and to identify cell types involved in initiation of profibrotic processes responsible for long-term kidney failure, a mouse model of nephrotoxic AKI was established for this thesis. The cytotoxic drug cisplatin, a chemotherapeutic drug widely used in the clinic for cancer therapies, was employed to induce kidney injury, as it is known to cause damage to renal proximal tubular epithelial cells (PTECs) as a major off-target effect.

Analysis of clinical markers showed that two low doses of cisplatin induced severe AKI while allowing long-term survival of mice. Excretory kidney function recovered by week 4, indicating clinical resolution of AKI. From week 10 onwards, histological fibrosis staining revealed progressive kidney fibrosis, a hallmark of CKD, in cisplatin-treated mice, despite apparent functional recovery from AKI. Notably, $CD3^+$ immune cell infiltration, particularly by $CD4^+$ T cells, into kidney tissue preceded the onset of kidney fibrosis by weeks, identifying a potential therapeutic window post-AKI. Gain- and loss-of-function experiments provided functional evidence that $CD4^+$ T cells are critical drivers of fibrosis development after resolving AKI. Single-cell RNAseq analyses further revealed a stress response in cisplatin-treated tubular cells and a shift in the $CD4^+$ T cell compartment from regulatory / Tr1-like cells to pro-inflammatory TNF^+ and $IFN\gamma^+$ tissue-resident memory T cells during AKI to CKD transition.

In conclusion, this study provides evidence for a working model in which an AKI-induced population of $CD4^+$ T_{RM} cells contributes to a persistent inflammatory niche in the kidney tissue by producing pro-inflammatory and profibrotic cytokines. This might

promote ongoing immune activation, tissue injury, and fibrotic remodelling. Through direct crosstalk with resident fibroblasts, T_{RM} cells may drive the differentiation of fibroblasts into myofibroblasts, promoting maladaptive repair even after apparent recovery of injured PTECs. These findings suggest that targeting $CD4^+$ T_{RM} cells could represent a promising therapeutic strategy to prevent AKI to CKD progression.

2 Zusammenfassung

Das akute Nierenversagen (ANV) ist ein Syndrom, welches durch eine plötzliche Verschlechterung der Nierenfunktion definiert ist und sich hauptsächlich in einer Beeinträchtigung der glomerulären Filtrationsrate äußert [1]. In Ländern mit hohem Einkommen stellt ANV eine große Herausforderung für das Gesundheitssystem dar. Obwohl die Beeinträchtigung der Nierenfunktion in den meisten Fällen von ANV wieder ausheilt, deuten neue Erkenntnisse darauf hin, dass ANV häufig zu langfristigen strukturellen Schäden im Nierenparenchym führt, was ein erhöhtes Risiko für die Entwicklung eines chronischen Nierenversagens (CNV), einer der weltweit häufigsten Todesursachen, zur Folge hat [2]. Trotz Forschungsbemühungen in den letzten Jahren sind die immunologischen Mechanismen, die dem Fortschreiten vom ANV zum CNV zugrunde liegen, noch immer nicht vollständig erforscht, und es fehlen nach wie vor wirksame therapeutische Maßnahmen, um dieses Fortschreiten zu attenuieren [3].
Zur Untersuchung der Rolle des Immunsystems bei der Progression vom ANV zum CNV sowie zur Identifikation der Zelltypen, die an der Initiierung profibrotischer Prozesse beteiligt sind, welche langfristig zu Nierenversagen führen, wurde für diese Arbeit ein Mausmodell des nephrotoxischen ANV entwickelt. Das Zytostatikum Cisplatin, ein in der Klinik häufig eingesetztes Chemotherapeutikum zur Behandlung von Krebserkrankungen, wurde verwendet um einen akuten Nierenschaden zu induzieren, da Cisplatin unter anderem Schäden an den proximalen Tubulusepithelzellen der Niere verursacht.

Eine Analyse klinischer Marker zeigte, dass zwei niedrig dosierte Cisplatin-Dosen schweres ANV induzieren, wobei ein langfristiges Überleben der Mäuse ermöglicht wurde. Die Nierenfunktion erholte sich innerhalb von vier Wochen, eine histologische Färbung fibrotischer Strukturen zeigte jedoch trotz des Rückgangs der klinischen Symptome ab Woche 10 eine Zunahme der renalen Fibrose als Hinweis für CNV bei den mit Cisplatin behandelten Mäusen. Auffallend war, dass die Infiltration von $CD3^+$-Immunzellen, insbesondere von $CD4^+$ T-Zellen, ins Nierengewebe dem Auftreten der renalen Fibrose um Wochen vorausging, was ein potenzielles therapeutisches Behandlungsfenster identifiziert. Gain- und Loss-of-Function-Experimente lieferten funktionelle Hinweise darauf, dass $CD4^+$ T-Zellen entscheidend für die Entwicklung von Fibrose nach Ausheilung des ANV sind. Einzelzell-RNA-Sequenzierungsanalysen

wiesen darüber hinaus Stressreaktionen in den Tubuluszellen Cisplatin-behandelter Mäuse nach, sowie eine Veränderung im $CD4^+$ T-Zell-Kompartiment von regulatorischen/Tr1-ähnlichen Zellen hin zu proinflammatorischen TNF^+- und $IFN\gamma^+$-geweberesidenten Gedächtnis-T-Zellen während des Übergangs vom ANV zum CNV.

Zusammenfassend liefern die Ergebnisse dieser Studie Belege für ein Arbeitsmodell, in dem eine durch ANV induzierte Population von $CD4^+$ Gedächtnis-T-Zellen durch die Produktion proinflammatorischer und profibrotischer Zytokine zur dauerhaften Erhaltung einer entzündlichen Mikroumgebung in der Niere beiträgt, was wiederum eine anhaltende Immunaktivierung, Gewebeschädigung und fibrotische Remodellierung fördern könnte. Durch direkte Wechselwirkungen können Gedächtnis-T-Zellen die Differenzierung von residenten Fibroblasten zu Myofibroblasten vorantreiben und so eine fehlerhafte Reparatur des Nierengewebes fördern, auch dann noch, wenn sich die geschädigten proximalen tubulären Epithelzellen bereits wieder erholt haben.
Diese Erkenntnisse legen nahe, dass die gezielte Eliminierung von $CD4^+$ Gedächtnis-T-Zellen eine vielversprechende therapeutische Strategie darstellen könnte, um das Fortschreiten vom ANV zum CNV zu verhindern.

3 List of figures

4 List of tables

5 Introduction

5.1 The kidney

The main function of the kidneys is to filter blood, eliminate waste products and maintain balanced electrolyte levels and plasma volume by highly regulated retention or excretion of water, salts, and minerals. Furthermore erythropoiesis, blood pressure, vitamin D production, and bone mineralisation are regulated by the kidneys [4, 5].

The kidney is composed of the cortex and medulla (Figure 1). The renal cortex consists of afferent arterioles upstream of glomeruli, glomeruli, efferent arterioles downstream of glomeruli, proximal and distal convoluted tubules, collecting ducts, and general vasculature, being responsible for the filtration of blood. The medulla is comprised of Loops of Henle, peritubular capillary networks, and terminal parts of collecting ducts, regulating the reabsorption of fluid, electrolytes, and metabolites [6].

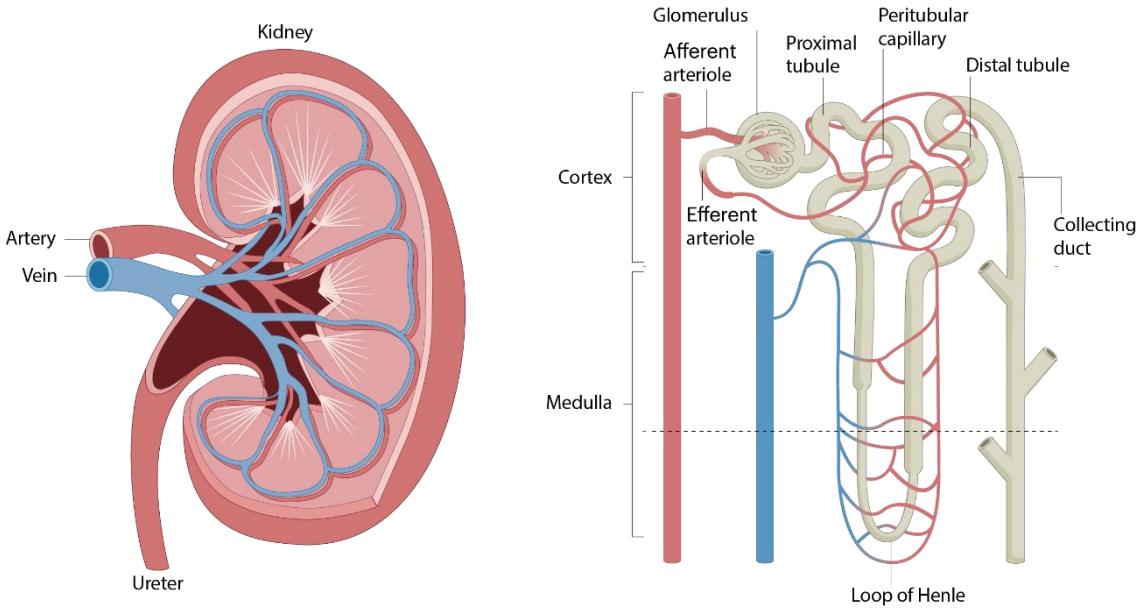

Figure 1: Anatomical and physiological structure of the kidney.
The kidney parenchyma is comprised of several pyramid-shaped lobes, each consisting of an outer renal cortex and an inner renal medulla. Nephrons are the functional units of the kidney, spanning the renal cortex and medulla and consisting of two main parts, the glomeruli-containing corpuscles and tubules. Figure adapted from Kurts *et al.*, 2025 [5].

Nephrons are the structural and functional units of the kidney. Per adult human kidney there are approximately one to two million nephrons, per adult mouse kidney about 14.000-16.000 [5, 7, 8].

Glomeruli are part of nephrons and responsible for glomerular filtration. An afferent arteriole is forming a network of glomerular capillaries which are surrounded by fenestrated endothelial cells, the glomerular basement membrane and are encased by podocytes (Figure 2) [4]. Podocytes extend into podocyte foot processes leaving small spaces between them which are called filtration slits. These filtration slits are covered by the slit diaphragm consisting of nephrin and other proteins and enable filtration of toxins and macromolecules from the blood. Podocytes are situated in the bowman space, which is lined by parietal epithelial cells and a second basement membrane [9-11]. The glomerulus is drained by an efferent arteriole transporting the filtered blood back to the systemic circulation. The bowman space opens up into a proximal tubule which is lined by proximal tubule epithelial cells [12].

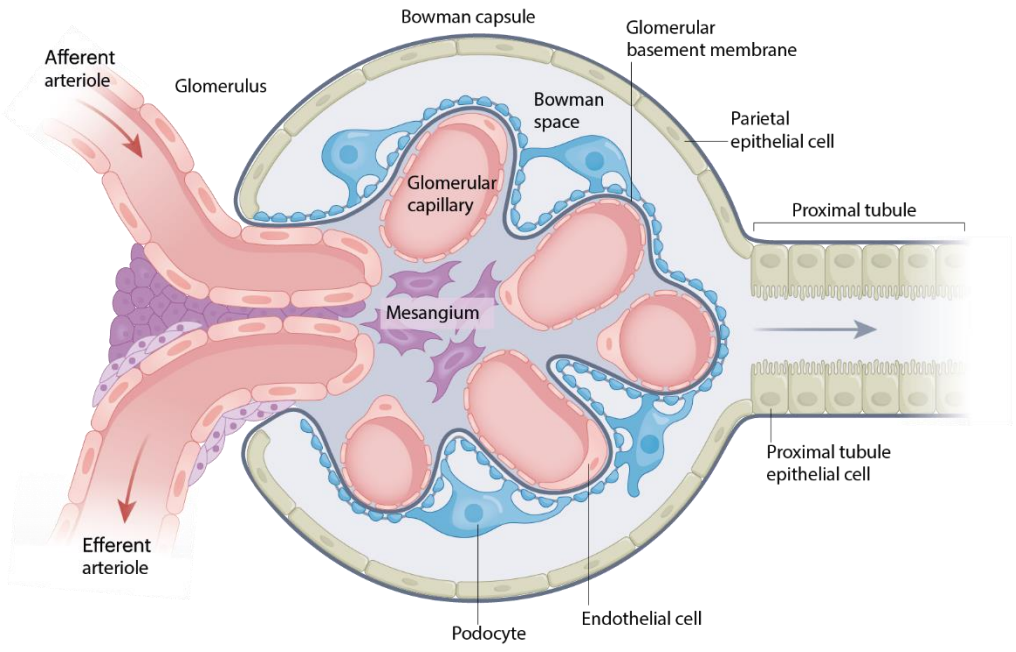

Figure 2: Anatomical and physiological structure of the glomerulus.
The glomerulus is a loop of capillaries surrounded by the Bowman's capsule located at the beginning of a renal nephron. In the glomerulus, ultrafiltration of blood through the glomerular filtration barrier takes place, resulting in filtrate entering the renal tubule. Figure from Kurts *et al.*, 2025 [5].

The first step of urine production is called glomerular filtration. Blood is entering the glomerulus via the afferent arteriole and blood pressure forces small substances such as water, nitrogenous waste products (urea, uric acid) and other metabolic waste products, amino acids, glucose, electrolytes, and drug metabolites out of the blood through filtration slits into the bowman space. Plasma proteins, such as albumin, and blood cells are retained due to size and charge constraints [4, 13, 14]. The filtered fluid passing from the bowman's capsule into the proximal convoluted tubule is called ultrafiltrate [15].

During tubular reabsorption, useful substances, such as selected electrolytes, peptides, and glucose are reabsorbed by active transport from renal tubules back into the peritubular capillary system [16, 17], while water is reabsorbed via passive diffusion in the distal section of the tubular system [18].

The final step of urine production is the tubular secretion. Active transporters in the proximal and distal convoluted tubules clear solutes, such as protein-bound molecules and drugs from the peritubular capillaries, which were not filtered by the glomerular basement membrane. These waste solutes are then secreted into the tubular fluid [4, 13, 19]. The reabsorption of sodium in the distal nephron is controlled by levels of the hormone aldosterone in order to regulate sodium and volume homeostasis [18].

5.2 Acute kidney injury

Definition and clinical relevance of AKI

Acute kidney injury (AKI) is a syndrome defined by a sudden decrease in kidney function, manifesting in impaired glomerular filtration that develops within seven days [1]. In high-income countries AKI occurs in one in five hospitalised adults and in every second patient in intensive care units, in total affecting over 13 million patients annually [2]. An estimated two million people worldwide die of AKI every year. Even in hospitalised patients that are not treated in intensive care units, mortality is on average between 10-20% [1, 20].

Acute kidney injury results in electrolyte imbalance, retention of waste products and an unspecific activation of the immune system which also affects organs other than the kidney [20]. The exposure to an AKI-initiating event is associated with poor outcomes. The syndrome causes significant acute morbidity and mortality, an increased risk of

complications and is associated with longer hospital stays and higher health care costs. In addition, even patients who survived AKI are at a higher risk of long-term morbidity and death even if kidney function recovers, indicating long-lasting subclinical alterations in the kidney tissue induced by AKI [21, 22]. This is further supported by the fact that patients who were diagnosed with AKI had an almost nine-fold higher adjusted risk of developing chronic kidney disease (CKD) compared to patients without AKI [23].

The spectrum of injury in AKI ranges from mild to severe [24]. The global non-profit organisation Kidney Disease Improving Global Outcomes (KDIGO) classifies AKI into three stages of severity based on increases in serum creatinine level, decreased urine output, or need for renal replacement therapies [25]. Current efforts and ongoing studies are furthermore investigating the implementation of renal damage biomarkers in addition to the longstanding KDGIO defined criteria for a more precise categorisation of AKI and improved patient care, including effective management of subclinical AKI patients [26].

Causes of AKI are classified as either prerenal, postrenal or intrarenal. Decreased blood flow to the kidney, e.g. in cases of dehydration or excessive blood loss, leads to prerenal injury. Postrenal is defined as an obstruction of urine flow, which can be the result of kidney stones or cancer in the urinary tract. Intrarenal injury occurs when the kidney parenchyma itself is damaged, the most common causes being severe systemic infections or the application of nephrotoxic drugs [27, 28].

Nephrotoxic AKI induced by the chemotherapeutic drug cisplatin

The agent cisplatin is a platinum-based chemotherapeutic drug widely used in the treatment of carcinomas and sarcomas such as ovarian, breast, head and neck, and testicular cancer [29]. Cisplatin is used for nearly 50% of all tumor chemotherapies [30], however the use of cisplatin in the clinic causes numerous toxic side effects, such as severe kidney damage, allergic reactions, gastrointestinal disorders, and hearing loss, with nephrotoxicity being the dose-limiting side effect [31, 32]. Almost one in three patients develops AKI after cisplatin treatment [33] and some patients, especially those who receive high doses or repeated courses of cisplatin, are at risk for long-term decline in kidney function (development of CKD), even if they do not develop AKI by clinical standards [34, 35].

Cisplatin is removed by the kidneys through both glomerular filtration and tubular secretion and accumulates in renal tubular cells either via passive diffusion or via transporter-mediated processes, resulting in intracellular concentrations that are five times higher than serum concentrations. The main membrane transporter mediating cisplatin uptake is CTR1, which is highly expressed in the basolateral membrane of proximal tubule cells [36, 37].

Following uptake into renal cells, chloride ions contained in the cisplatin structure are displaced by water in a process called aquation. This results in the generation of a highly electrophile molecule which preferentially binds to nucleophile structures as nitrogen donor atoms in nucleic acids, leading to inter- and intrastrand crosslinking of DNA [38-40].

The mode of action of cisplatin is based on interfering with DNA replication and repair, causing mitochondrial dysfunction, oxidative stress, arrest of cell-cycles, and activation of apoptosis [31, 37]. By this mechanism, cisplatin affects especially rapidly proliferating cells, in particular cancer cells [41], but also proximal tubule cells (Figure 3), which are characterised by a high regenerative capacity [42].

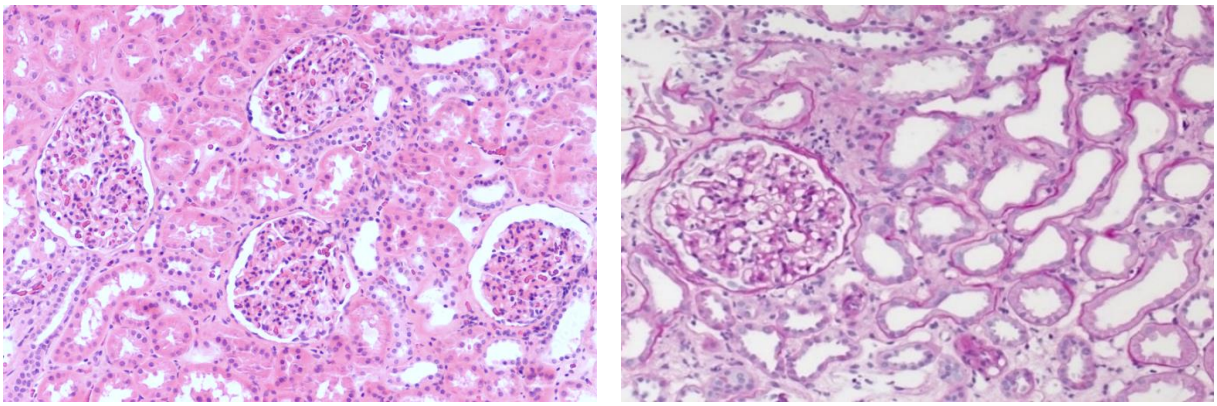

Figure 3: Histological pictures of kidneys of healthy and cisplatin-treated patients.
Healthy kidney tissue (left) shows normal structures of glomeruli and tubules. Renal biopsy tissue of a cisplatin-treated patient (right) shows damaged tubules with flattening of the proximal tubule cells, but intact glomerulus. The histology picture of healthy kidney tissue was acquired by Dr. David A. Litman (pathology, Salinas Valley Health Medical Center). The picture of kidney tissue from a cisplatin-treated patient was acquired by Prof. Dr. med. Thorsten Wiech (Nephropathology Unit, University Medical Center Hamburg-Eppendorf).

Therapeutic options in AKI

Current treatment options of AKI focus on elimination of underlying causes, and supportive care. The latter includes avoidance of nephrotoxins (wherever possible), optimal fluid management, vasopressor therapy to increase blood pressure and, if necessary, renal replacement therapy (RRT) [43]. Elimination of the cause of AKI might allow for spontaneous regeneration of damaged tubular cells, but therapeutic options that actively support kidney regeneration or amelioration of progression to CKD are, to date, not available [44, 45].

A variety of therapies to promote kidney regeneration by targeting specific pathways are currently under development. Potential therapeutic options include renal blood flow modifiers managing hemodynamics, antioxidants reducing free radicals, anti-inflammatory mediators manipulating inflammatory pathways, as well as transcription modifiers changing gene expression [43].

5.3 Long-term consequences of acute kidney injury

Until recently, acute kidney injury was perceived as a self-limited condition with a high potential for complete recovery, if the underlying cause could be eliminated. However, in recent years, it has become evident that AKI is frequently associated with long-term structural alterations in the kidney tissue with the clinical consequence of increased risk for CKD development and death. These structural alterations are the result of maladaptive repair processes after AKI which are characterised by chronic interstitial inflammation, fibrosis, and vascular rarefaction, ultimately leading to tubular loss and glomerulosclerosis [46, 47].

To emphasize that renal pathophysiologic processes are ongoing after the classical AKI span of seven days, the concept of a continuum was developed, in which AKI is followed by acute kidney disease (AKD), followed after three months by chronic kidney disease (CKD). AKD describes acute or subacute alterations of regular kidney function and/or structure for a duration of between seven and 90 days after exposure to an AKI-initiating event, whereas CKD is defined by the persistence of kidney disease for a period of over 90 days (Figure 4) [1, 20].

Persistent kidney disease is associated with an increased risk of adverse outcomes, especially cardiovascular events, premature deaths, and the development of end-stage renal disease (ESRD) [48, 49].

The leading causes for the development of CKD in developed countries are hypertension, diabetes mellitus, and vascular diseases [50, 51]. Transition of AKI via AKD to CKD is now seen as another major cause of CKD. Despite recent research efforts, there are to date no therapies to prevent AKI to CKD transition. Furthermore, suitable biomarkers that predict the risk or onset of AKI to CKD transition are lacking, rendering potential preventive therapies challenging [44].

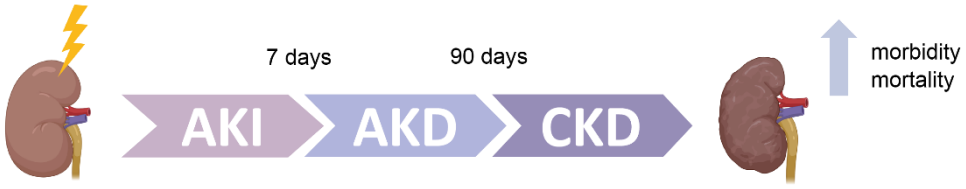

Figure 4: The continuum of acute kidney injury, acute kidney disease, and chronic kidney disease.
After an AKI-initiating event, a decrease in kidney function develops within seven days. Maladaptive repair after AKI leads to AKD which after three months transitions to CKD and persistent kidney disease. Figure adapted from Chawla *et al.*, 2017 [1].

The current generally recognised state of research is that CKD ultimately and inevitably leads to the development of ESRD through continuous and progressive loss of estimated glomerular filtration rate (GFR) and therefore renal function, while ESRD can also occur in an uneven and unpredictable manner if AKI-causing events were taking place beforehand [52].

Molecular mechanisms for the development and progression of CKD to ESRD comprise among others oxidative stress, persistent low-grade inflammation and fibrotic processes including the emergence of myofibroblasts, resulting in tubulointerstitial fibrosis [53, 54]. Oxidative stress is defined as disturbances in the pro- and anti-oxidant balance, leading to disruption of redox signalling, molecular damage and oxidation of biological molecules like DNA and proteins.

Several uremic toxins are associated with increased levels of oxidative stress in CKD leading to worsening of renal function and progression to ESRD by altering renal blood flow, causing inflammation and fibrotic changes and onsetting proteinuria [54].

Fibrotic processes are manifested by presence of myofibroblasts in the interstitial space. Myofibroblasts are defined by the combined expression of fibroblast markers (fibroblast-specific protein 1 (FSP1)), smooth muscle cell markers (α-smooth muscle actin (α-SMA)) and endothelial cell markers (platelet and endothelial cell adhesion molecule 1 (PECAM1), platelet-derived growth factor receptor β (PDGFRβ)) [55]. The majority of renal myofibroblasts originates from epithelial-mesenchymal transition (EMT), where fully differentiated epithelial cells fail to restore epithelial cell properties and functions after the acute phase of AKI (Figure 5). These cells lose their polarity, undergo phenotypic transition and change their expression profiles to become collagen-producing myofibroblasts [44, 55, 56]. EMT is closely associated with fibrosis by contributing to excessive deposition of fibrous connective tissue and extracellular matrix (ECM), resulting in tissue scarring and organ failure [57-59]. As the terminal consequence, irreversibly injured kidney tissue, more precisely dead epithelial cells, gets replaced with connective tissue, leading to progressive loss of kidney function [5].

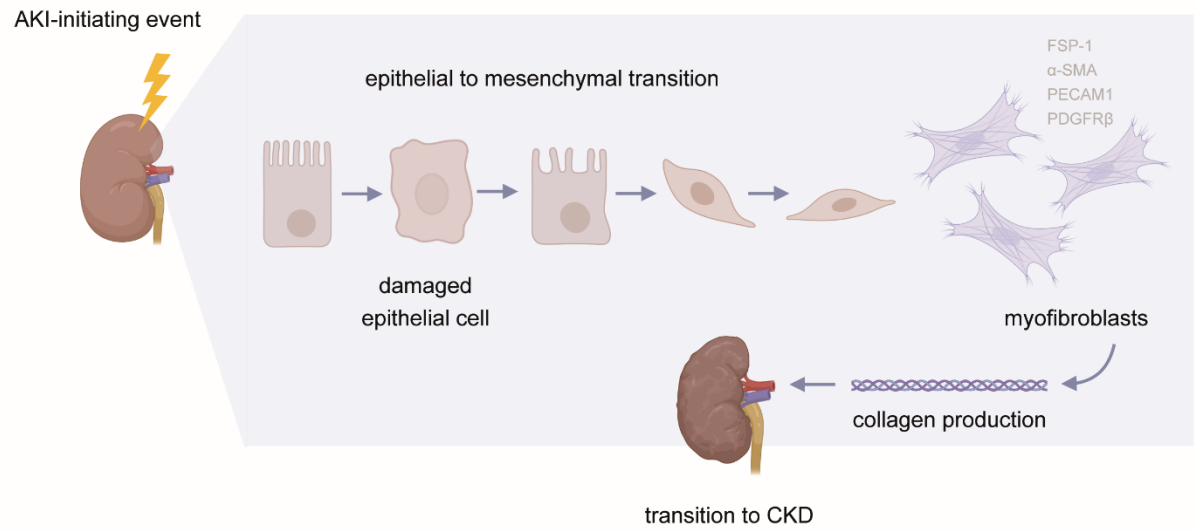

Figure 5: Epithelial to mesenchymal transition after an AKI-initiating event.
After the acute phase of AKI, damaged epithelial cells fail to restore cell properties and functions and become collagen-producing myofibroblasts, participating in fibrosis and transition from AKI to CKD.

5.4 Immune cells in acute kidney injury and progression to chronic kidney disease

The immune system can be subdivided into the innate and the adaptive immune system, which are working closely together. The innate immune response is considered to be the first line of defense against invading pathogens. Innate immune cells recognise a limited number of pathogenic molecules through pattern recognition receptors like Toll-like receptors and start a cascade of rapid response mechanisms.
Subsequent to this broad initial response of the innate immune system, the adaptive immune system comes into play. The high level of specificity of the adaptive immune system is based on T and B lymphocytes, which are equipped with highly diverse and unique antigen receptors. This diversity is generated through genetic reorganisation in the form of DNA recombination of T and B cell antigen receptors during lymphocyte development in the thymus and bone marrow, resulting in a vast repertoire of receptor sequences, each with a distinct specificity for a particular antigen. Furthermore, the adaptive immune system develops memory of encountered pathogens for long-lasting protection from repeated infections [60-64].
A variety of both innate and adaptive immune cells are recruited to the kidney and activated during AKI and participate in chronic inflammatory processes that promote the progression of AKI to CKD. In the following, several immune cell populations involved in this progression will be introduced, with a special focus on effector $CD4^+$ T cells.

5.4.1 Cells of the innate immune system

The majority of cells from the innate immune system belong to the myeloid lineage that develops from a common myeloid progenitor (CMP) in the bone marrow. The inflammatory infiltrate involved in the AKI to CKD transition includes neutrophils, as well as mononuclear phagocytes, such as monocytes and macrophages. Natural killer (NK) cells, although derived from a common lymphoid progenitor (CLP) in the bone marrow, are also classified as innate immune cells due to their rapid, antigen-independent effector functions. Innate immune cells either directly cause damage during AKI or recruit cells of the adaptive immune system.

Neutrophils

Neutrophils represent key effector cells in the acute inflammatory response, typically constituting the first leukocyte population recruited to sites of inflammation and being the predominant leukocytes infiltrating the kidney immediately following ischemia-reperfusion injury (IRI). Neutrophil recruitment is facilitated by membrane adhesion molecules that are expressed and upregulated both on the endothelium and the neutrophils [65-68]. Neutrophils are activated by different cytokines, growth factors, and bacterial products and are important for pathogen clearance by mechanisms such as degranulation of antimicrobial proteins and production of neutrophil extracellular traps [65].

During AKI, neutrophils migrate from the circulation into the kidney, where they adhere to endothelial cells and transmigrate into the renal interstitium. They promote kidney damage by secreting proinflammatory cytokines and producing reactive oxygen species and proteases. Depending on the renal microenvironment, infiltrated monocytes differentiate either into phagocytic macrophages or antigen-presenting dendritic cells [69-72].

Mononuclear phagocytes

The reaction of macrophages to tissue damage is dependent on the respective microenvironment, underscoring the great phenotypic plasticity of macrophages. Long-lived tissue macrophages reside within tissues and act as first responders of the innate immune defence to infectious agents. In the kidney, macrophages represent the most abundant resident immune cell type. After kidney injury, circulating bone marrow-derived monocytes are rapidly recruited to the tubulointerstitium, where they are activated and differentiated into macrophages [44, 73, 74]. The number of infiltrated macrophages in the kidney is directly associated with severity of fibrosis and kidney injury [75]. M1 macrophages secrete pro-inflammatory cytokines including IL-6, TNFα and IL-1β, supporting Th1-type adaptive immune responses, favouring tubulointerstitial inflammation and worsening kidney damage. M2 macrophages, on the other hand, are predominant at later time points during the resolution phase of kidney injury and are, among other cell types, responsible for kidney tissue repair and regeneration by secreting anti-inflammatory and tissue repair mediators, such as IL-4 and IL-13, which induce Th2-type immune responses [44, 75-78]. In contrast, M2 macrophages derived from bone marrow cells, can also transform into myofibroblasts via macrophage-to-myofibroblast

transition, produce profibrotic mediators including TGF-β and might thereby contribute to tissue fibrosis and progression of AKI to CKD [65, 74].

Furthermore, under inflammatory conditions, macrophages are producing Wingless and Int-1 (Wnt) ligands and therefore enable Wnt signalling, a profibrotic pathway that also gets activated by AKI-induced unrestored apicobasolateral polarity in proximal tubular epithelial cells (see 5.3), resulting in fibroproliferative effects exerted by myofibroblasts [75, 79].

Natural killer cells

NK cells belong to the extensive family of innate lymphoid cells and exert cytotoxic functions by detecting and eliminating damaged and virus-infected cells, as well as tumor cells. Additionally, they have immune regulatory properties through secretion of cytokines and chemokines [80-82]. Within four hours after IRI, NK cells traffic from blood to the kidneys. Injured tubular epithelial cells release chemokines that attract cells via the CC chemokine receptor 5 (CCR5) receptor such as NK cells, which in turn produce chemokines attracting neutrophils to the kidney, worsening inflammation and kidney damage [80, 83, 84]. NK cells can also directly kill tubular epithelial cells by the release of cytotoxic granules [85]. In line with a pathogenic effect of NK cells, total depletion of NK cells by antibody injection protects against AKI induced by IRI [86]. Whether NK cells in cisplatin-induced acute kidney injury have a protective or detrimental effect is yet to be examined in detail [87].

5.4.2 Cells of the adaptive immune system

The adaptive immune system consists of T and B lymphocytes, both of which originate from a common lymphoid progenitor (CLP) in the bone marrow. T cells undergo maturation in the thymus and primarily mediate cell-mediated immunity through diverse functional roles. In contrast, B cells mature within the bone marrow and are the main effector cells of humoral immunity by producing antibodies. These antibodies specifically recognise and bind to antigens, neutralising pathogens or facilitating their elimination by other immune effector cells [63, 88].

The following sections focus on different subsets of T cells and their roles in transition of AKI to CKD.

CD4⁺ T cells

Following selection and maturation in the thymus, naïve CD4⁺ T cells migrate to the periphery, where they are activated through the interaction of their T cell receptors (TCRs) and the CD4 co-receptor with antigen-loaded major histocompatibility complex class II (MHC II) molecules presented by antigen presenting cells (APCs) such as dendritic cells, macrophages, and B cells. The subsequent activation of the TCR and CD3 triggers a cascade of downstream signalling pathways, ultimately resulting in activation, clonal expansion, and differentiation of naïve CD4⁺ T cells [89, 90]. Upon activation, naïve CD4⁺ T cells differentiate either into memory or effector CD4⁺ T cells. Memory CD4⁺ T cells protect tissues from reinfection and cancer, but can also participate in autoimmunity and chronic infection [91]. Short lived effector CD4⁺ T cells are executing immune functions by activating other immune cells and producing cytokines which orchestrate responses of tissue cells [89, 92]. Depending mainly on the cytokine milieu of the respective microenvironments in which they get activated, CD4⁺ effector T cells differentiate into different subsets. The three main T helper (T_h) cell subsets in the kidney comprise T_h1, T_h2, and T_h17 cells, as well as T_{reg} cells (Figure 6) [87, 89].

Effector CD4⁺ T cells

The differentiation of naïve T cells into T_h1 cells is promoted by the cytokines IFNγ and IL-12. T_h1 cells are regulated by the transcription factor T-box expressed in T cells (T-bet), which suppresses T_h2 and T_h17 lineages, and characteristically express CXC motif chemokine receptor 3 (CXCR3) on their surface [93, 94]. Through the production of IFNγ and TNFα, T_h1 cells fight intracellular pathogens, such as bacteria and viruses, which leads to the implication of T_h1 cells in the pathogenesis of kidney injury [95]. T_h1 cells circulate within the periphery but can also express tissue-resident phenotypes [96]. T_h2 cells are induced by cytokine IL-2 and IL-4 signalling, express the transcription factor GATA3 and present the chemokine receptor CCR4 on their surface [97]. By secreting IL-4, IL-5 and IL-13 they exert protective roles in response to parasitic infections, are associated with chronic inflammation such as asthma and allergic diseases, but also facilitate tissue repair. Knockdown of T_h2 transcription factor STAT6 is associated with markedly worse renal function and tubular injury following IRI, likely because of IL-4 deficiency [73, 94, 98, 99].

T_h17 differentiation is driven by the cytokines IL-6 and TGF-β. T_h17 cells are controlled by the transcription factor retinoic acid-related orphan receptor γt (RORγt), can be iden-

tified by the surface marker CCR6 and secrete IL-17 and IL-22 [89, 100]. In response to fungal and extracellular bacterial infections, especially at mucosal tissue, T_h17 cells mediate immunity mainly by neutrophil recruitment and IL-1-driven epithelial activation. Additionally, T_h17 cells protect against chronic inflammation and autoimmune diseases [94, 101]. In recent years, research has increasingly focused on the detailed role of T_h17 cells in AKI pathophysiology. T_h17 cells represent the predominant lymphocyte population infiltrating the kidney following AKI in mice. During the early phase of renal IRI, T_h17 cells are expanded and activated through IL-1 secreted by resident dendritic cells, macrophages and TEC [73, 102, 103]. Within seven days, T_h17 cells return to baseline levels [104].

Functionally, effector $CD4^+$ T cells exert pathogenic effects in early renal injury. In IRI- and cisplatin-induced AKI mouse models, depletion of $CD4^+$ T cells confers protection [105, 106]. Furthermore, postischemic injury was restored when CD4-deficient mice were reconstituted with $CD4^+$ T cells [105]. Further evidence suggests that $CD4^+$ T cells also promote interstitial fibrosis, manifested in increased collagen deposition and *Col1* mRNA levels [107]. In early kidney injury, T_h1 cells mount a strong IFNγ response, which subsequently gets replaced by T_h17 cells perpetuating injury and tissue fibrosis [73].

Regulatory $CD4^+$ T cells

$CD4^+$ $CD25^+$ regulatory T cells express both the transcription factor forkhead box P3 (FOXP3) and surface marker CD25 and have a key role in the maintenance of peripheral immunologic self-tolerance [73, 108]. T_{regs} act as immunosuppressive cells by expressing the inhibitory cytokines IL-10 and TGFβ, exert protective functions early in AKI and help with resolution of inflammation by dampening pro-inflammatory responses [87, 94, 109]. Two primary subsets of T_{regs} can be distinguished based on their origin: thymic T_{regs}, also referred to as natural T_{regs}, which develop in the thymus, and induced T_{regs}, which differentiate from conventional $CD4^+$ T cells in the periphery following antigen exposure while IL-2 and TGF-β are present [94].

Both in IRI- and cisplatin-induced AKI models, it was shown that there is significant T_{reg} trafficking into the post-ischemic kidney. T_{regs} reduce the production of proinflammatory cytokines by $CD4^+$ T cells, lower leukocyte infiltration, suppress the innate immune system via IL-10 production, and improve repair of renal damaged tissue, which overall results in attenuated AKI [110-113]. T_{reg}-mediated reduction of ischemia reperfusion-

induced inflammation and injury depended on the presence of programmed death ligand 1 and 2 (PD-L1/2) on the surface of T_{regs} [114]. Interestingly, there are first hints that during the chronic phase after kidney injury resident T_{regs} exhibit heterogeneity. A recent study identified two transcriptionally different T_{reg} subsets, one of which has a pro-regenerative signature, while the other subset shows profibrotic properties [115].

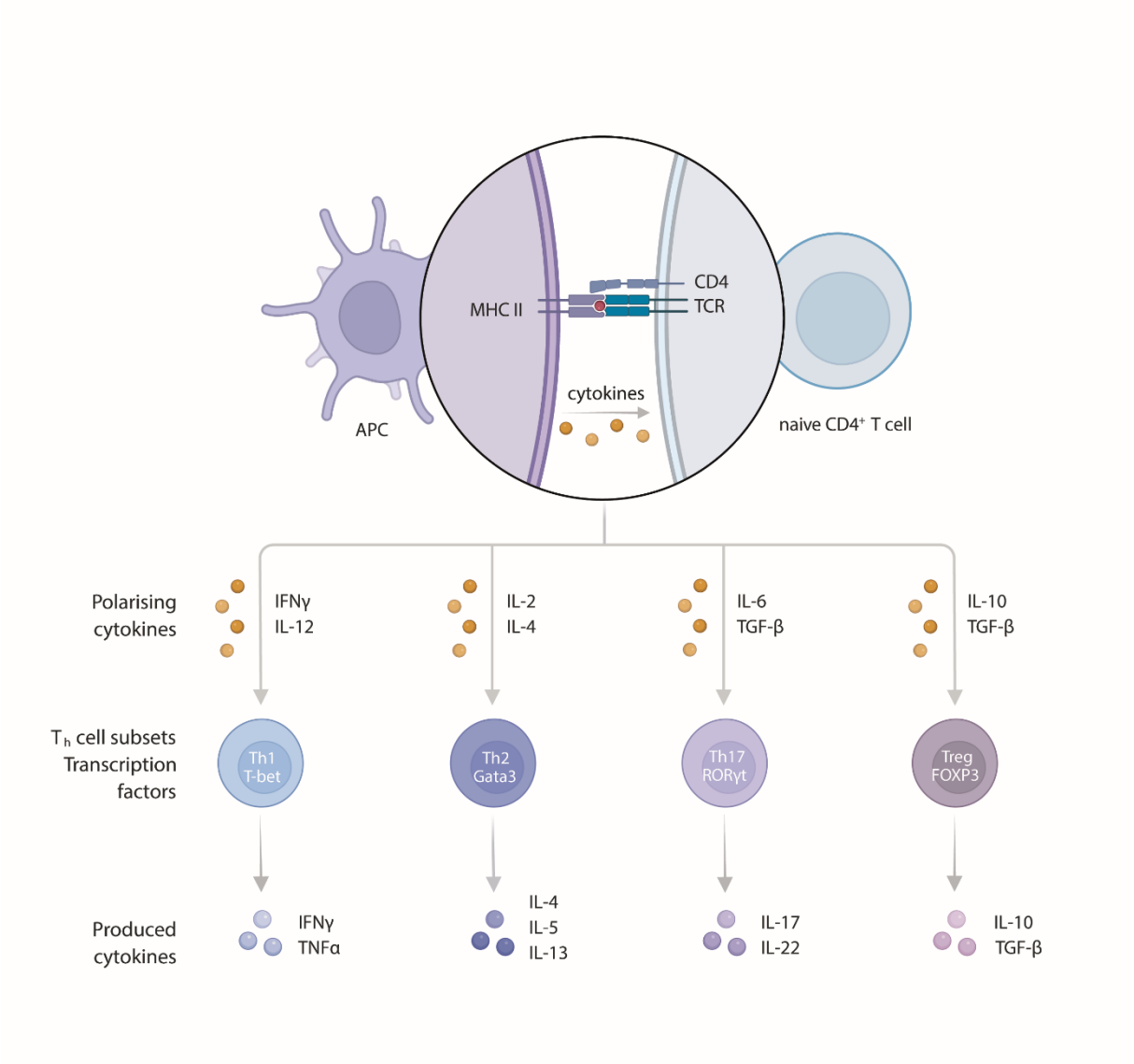

Figure 6: Characteristics of main effector CD4⁺ T helper cell subsets.
CD4⁺ effector T cells differentiate into various helper cell subsets, each polarised by specific cytokines, controlled by distinct transcription factors, and characterised by the production of unique cytokine profiles. Different T helper cell subsets participate either in pro-inflammatory processes worsening kidney damage and promoting the progression of AKI to CKD or contribute to anti-inflammatory mechanisms initiating kidney repair and regeneration.

$CD8^+$ T cells

Activation of $CD8^+$ T cells is primarily initiated by recognition of antigenic peptides presented on MHC class I molecules which are ubiquitously expressed on all nucleated cells. These MHC class I molecules present fragments of intracellular proteins, including viral or tumor-derived peptides, to $CD8^+$ T cells, enabling immune surveillance throughout the body [116, 117]. Similar to $CD4^+$ T cells, naïve $CD8^+$ T cells differentiate into memory or effector $CD8^+$ T cells after encountering an antigen. Memory $CD8^+$ T cells exert protective functions following antigen reencounter, resulting in efficient long-term immunity. Effector $CD8^+$ T cells are cytotoxic T cells and can induce apoptosis of target cells directly by interaction of Fas with its ligand FasL and through secretion of perforin, a protein with cytolytic properties [87, 94]. During AKI, the cytotoxic function of $CD8^+$ T cells seems to be dispensable, but the secretion of pro-inflammatory cytokines IFNγ and TNF by $CD8^+$ T cells after renal injury still worsens the outcome of AKI [110, 118].

Although deficiency in $CD8^+$ T cells ameliorates kidney injury and protects from cisplatin-induced renal dysfunction [106], $CD8^+$ T cell deficient mice were not protected from renal IRI to an extent comparable with the protection conveyed by depletion of $CD4^+$ T cells [105]. $CD8^+$ T cells infiltrate into the kidney shortly after kidney injury. Their recruitment is mediated by macrophages through the CXCL16-CXCR6 pathway. In a mice model of unilateral IRI (uIRI) it was shown that $CD8^+$ T cells closely interact with endothelial cells at day 14 and 18 after injury via the Fas ligand-Fas signalling pathway, which promotes apoptosis of endothelial cells, loss of peritubular capillaries and kidney fibrosis during transition of AKI to CKD [119].

6 Aims of this doctoral thesis

Acute kidney injury is a syndrome defined by a sudden decrease in kidney function manifesting in impaired glomerular filtration [1]. In high-income countries AKI occurs in one in five hospitalised adults and in every second patient receiving intensive care [2]. AKI is one of the major causes of CKD [120], a condition affecting more than 10% of the general population worldwide, resulting in over 800 million affected individuals [121]. CKD has become apparent as one of the leading causes of mortality worldwide [122], underlining the urgent need for research targeting the processes that are responsible for development of severe kidney damage.

Since the immunological mechanisms underlying the transition of AKI to CKD are incompletely understood, the objective of this thesis is to investigate the renal immunological processes contributing to transition of cisplatin-induced AKI to CKD. In particular, the research work will focus on elucidating the role of $CD4^+$ T cells in initiating profibrotic processes in chronic 'subclinical' inflammation after onset of AKI, resulting in fibrosis development and sustained kidney function impairment.

To achieve a better understanding of the corresponding mechanisms, this study comprises three specific aims:

1) Using a low-dose cisplatin mouse model causing damage to proximal tubular epithelial cells (AKI) with complete resolution of kidney damage in the acute phase, but ultimately resulting in progressive interstitial fibrosis and chronic kidney disease, to investigate AKI to CKD transition.
2) Identification of immune cells that are involved in the transition of AKI to CKD by histological analysis, flow cytometry, and single-cell RNA sequencing.
3) Functional validation of $CD4^+$ T cells as candidate cell types potentially responsible for AKI to CKD transition via gain-of-function and loss-of-function approaches.

Achieving these aims will provide insights that might contribute to development of treatment approaches targeting the transition of AKI to CKD.

7 Materials

7.1 Laboratory equipment

Table 1: List of utilised laboratory equipment

Laboratory equipment	Provider
AxioCam MRc	Zeiss (Oberkochen, Germany)
Axio Scope A1 microscope	Zeiss (Oberkochen, Germany)
Biofuge fresco (85 mm rotor)	Heraeus (Hanau, Germany)
Chromium Controller	10x Genomics (Pleasanton, US)
Chromium X	10x Genomics (Pleasanton, US)
COBAS Integra 400 plus	Roche (Basel, Switzerland)
Dako Pen	Agilent Technologies (Santa Clara, US)
DS-11 Spectrophotometer	DeNovix (Wilmington, US)
Eclipse TS100 microscope	Nikon (Amstelveen, Netherlands)
EL808 Ultra Microplate Reader	Biotek (Winooski, US)
FACS Aria Fusion	BD Biosciences (Franklin Lakes, US)
FACSymphony A3	BD Biosciences (Franklin Lakes, US)
GentleMACS Dissociator	Miltenyi Biotec (Bergisch Gladbach, Germany)
HistoCore Autocut	Leica (Wetzlar, Germany)
HistoCore Water Bath	Leica (Wetzlar, Germany)
MACSmix Tube Rotator	Miltenyi Biotec (Bergisch Gladbach, Germany)
MACS MultiStand	Miltenyi Biotec (Bergisch Gladbach, Germany)
Microscale R160P	Sartorius (Göttingen, Germany)
Multifuge X3R Centrifuge	Thermo Fisher Scientific (Waltham, US)
NanoDrop 2000 Spectrophotometer	Thermo Fisher Scientific (Waltham, US)
Neubauer Cell Counting Chamber	Carl Roth (Karlsruhe, Germany)
QuadroMACS Separator	Miltenyi Biotec (Bergisch Gladbach, Germany)
QuantStudio Real-Time PCR System	Thermo Fisher Scientific (Waltham, US)

TC20 Automated Cell Counter	Bio-Rad (Hercules, US)
Thermocycler T3	Biometra (Göttingen, Germany)
TissueLyser II	Qiagen (Venlo, Netherlands)
Waterbath 1004	GFL (Berlin, Germany)

7.2 Consumables

Table 2: List of utilised consumables

Consumable	**Provider**
96 Fast PCR Plate Halbrand	Sigma Aldrich (St. Louis, US)
Cell strainers (40 µm, 70 µm, 100 µm)	Corning (Corning, US)
CellTrics strainers (50 µm)	Sysmex Partec (Görlitz, Germany)
COBAS Sample Cups	Roche (Basel, Switzerland)
Falcon tubes (15 ml, 50 ml)	Greiner Bio-One (Kremsmünster, Austria)
Filter tips (10 µl, 20 µl, 200 µl, 1000 µl)	Sarstedt (Nümbrecht, Germany)
GentleMACS C Tubes	Miltenyi Biotec (Bergisch Gladbach, Germany)
LS Columns	Miltenyi Biotec (Bergisch Gladbach, Germany)
Microtubes EDTA	Sarstedt (Nümbrecht, Germany)
MS Columns	Miltenyi Biotec (Bergisch Gladbach, Germany)
Omnifix-F syringes	B. Braun (Melsungen, Germany)
PCR film free from DNase/RNase transparent	Sarstedt (Nümbrecht, Germany)
Präzisa scalpels	Dahlhausen (Köln, Germany)
Reaction tubes (0.5 ml, 1.5 ml, 2 ml, 5 ml)	Sarstedt (Nümbrecht, Germany)
SafeSeal reaction tubes (1.5 ml)	Sarstedt (Nümbrecht, Germany)
Serological pipettes (5 ml, 10 ml, 25 ml, 50 ml)	Sarstedt (Nümbrecht, Germany)
Sterican cannulas (0.30 mm, 0.40 mm, 0.60 mm)	B. Braun (Melsungen, Germany)
Tissue culture plates 96 well (Standard F, Standard C)	Sarstedt (Nümbrecht, Germany)
Tungsten Carbide Beads 3 mm	Qiagen (Venlo, Netherlands)

7.3 Chemicals, solutions and buffers

Table 3: List of utilised chemicals, solutions and buffers

Chemical, solution or buffer	Provider
Aluminium potassium sulfate dodeca-hydrate ($AlH_{24}KO_{20}S_2$)	Merck (Darmstadt, Germany)
Ammonium chloride (NH_4Cl)	Sigma Aldrich (St. Louis, US)
Antibody Diluent	Zytomed Systems (Berlin, Germany)
Anti-mouse CD4 antibody clone GK1.5	Bio X Cell (Lebanon, US)
Aqua dest.	B. Braun (Melsungen, Germany)
autoMACS Running Buffer / MACS Separation Buffer	Miltenyi Biotec (Bergisch Gladbach, Germany)
Bovine Serum Albumin	GE Healthcare (Chicago, US)
Cis-Diamineplatinum(II)dichloride (Cisplatin)	Sigma Aldrich (St. Louis, US)
Cleaved Caspase-3 (5A1E) Rabbit mAb	Cell Signaling Technology (Danvers, US)
Collagenase D	Roche (Basel, Switzerland)
CountBright Absolute Counting Beads	Invitrogen AG (Waltham, US)
Dako Target Retrieval Solution (pH 6, pH 9)	Agilent Technologies (Santa Clara, US)
Direct Red 80 (Sirius Red F3b)	Sigma Aldrich (St. Louis, US)
Di-sodium hydrogen phosphate dihydrate ($Na_2HPO_42H_2O$)	Merck (Darmstadt, Germany)
DNase I	Roche (Basel, Switzerland)
DNTP Set (100 mM)	Invitrogen (Waltham, US)
DreamTaq DNA Polymerase	Thermo Fisher Scientific (Waltham, US)
Dulbecco’s Phosphate Buffered Saline 1-fold (DPBS)	Gibco (Darmstadt, Germany)
Dulbecco’s Phosphate Buffered Saline 10-fold (DPBS)	Biowest (Bradenton, US)
Ethylenediaminetetraacetic acid (EDTA)	Invitrogen (Waltham, US)
Eukitt mounting medium	Sigma Aldrich (St. Louis, US)
FACS Clean Solution	BD Biosciences (Franklin Lakes, US)
FACS Flow Sheath Fluid	BD Biosciences (Franklin Lakes, US)
Fast Green FCF	Sigma Aldrich (St. Louis, US)
Fetal Bovine Serum (FBS)	Gibco (Darmstadt, Germany)

Fixation / Permeabilization Concentrate	Invitrogen (Waltham, US)
Fixation / Permeabilization Diluent	Invitrogen (Waltham, US)
Formaldehyde solution 37%	Merck (Darmstadt, Germany)
Glacial acetic acid (CH_3CO_2H)	Sigma Aldrich (St. Louis, US)
Gum arabic	Sigma Aldrich (St. Louis, US)
Hematoxylin	SERVA Electrophoresis (Heidelberg, Germany)
HEPES	Gibco (Darmstadt, Germany)
Hydrochloric acid (HCl)	Merck (Darmstadt, Germany)
Isotype control rat IgG2b, anti-keyhole limpet hemocyanin	Bio X Cell (Lebanon, US)
Naphthol AS-BI phosphate ($C_{18}H_{15}BrNO_6P$)	Sigma Aldrich (St. Louis, US)
New Fuchsin	Sigma Aldrich (St. Louis, US)
N,N-Dimethylformamide ($HCON(CH_3)_2$)	Carl Roth (Karlsruhe, Germany)
Normal Mouse Serum	Biozol (Eching, Germany)
Normal Mouse Serum	Jackson ImmunoResearch (West Grove, US)
Penicillin/Streptomycin (5000 units / ml Penicillin, 5000 µg / ml Streptomycin)	Gibco (Darmstadt, Germany)
Percoll PLUS	Cytiva (Marlborough, US)
Permeabilization Buffer	Invitrogen (Waltham, US)
Picric acid solution	Sigma Aldrich (St. Louis, US)
Polyclonal Rabbit Anti-Human CD3	Agilent Technologies (Santa Clara, US)
PowerUp SYBR Green Master Mix	Applied Biosystems (Foster City, US)
Random Hexamer Primers	Thermo Fisher Scientific (Waltham, US)
RevertAid Reverse Transcriptase	Thermo Fisher Scientific (Waltham, US)
RNaseOUT Ribonuclease Inhibitor	Invitrogen (Waltham, US)
RNase ZAP	Sigma Aldrich (St. Louis, US)
RPMI 1640 medium	Gibco (Darmstadt, Germany)
Sedaconda (isoflurane) 100%	Sedana Medical (Stockholm, Sweden)
Sodium dihydrogen phosphate monohydrate ($NaH_2PO_4H_2O$)	Merck (Darmstadt, Germany)
Sodium chloride (NaCl)	Sigma Aldrich (St. Louis, US)

Sodium iodate ($NaIO_3$)	Sigma Aldrich (St. Louis, US)
Sodium nitrate ($NaNO_3$)	Sigma Aldrich (St. Louis, US)
TaqMan Fast Universal PCR Master Mix	Applied Biosystems (Foster City, US)
TaqMan Gene Expression Assay	Applied Biosystems (Foster City, US)
Tris-hydrochloride (Tris-HCl)	Carl Roth (Karlsruhe, Germany)
Trizma base	Sigma Aldrich (St. Louis, US)
Trypan Blue Stain 0.4%	Gibco (Darmstadt, Germany)
Tween 20	MP Biomedicals (Santa Ana, US)

7.4 Self-produced solutions, buffers and media

Table 4: List of self-produced solutions, buffers and media

Solution or buffer	**Composition**
Böhmer's hematoxylin solution A	200 ml aqua dest., 10 g aluminium potassium sulfate dodecahydrate, 0.1 g sodium iodate
Acidified aqua dest.	300 ml glacial acetic acid, 660 ml aqua dest.
Böhmer's hematoxylin solution B	0.5 g hematoxylin, 10 g *N,N*-Dimethylformamide
Complete medium	RPMI 1640, 10% Fetal Bovine Serum, 1% HEPES, 1% Penicillin/Streptomycin
Erythrocyte lysis buffer I	21.10 g Tris-hydrochloride, 1000 ml H_2O, pH 7.6
Erythrocyte lysis buffer II	8.54 g ammonium chloride, 1000 ml H_2O
Fast Green solution	200 ml Fast Green stock 0.1%, 10 ml glacial acetic acid
Fast Green stock 0.1%	1 g Fast Green FCF, 1000 ml water saturated picric acid
Fixation / Permeabilization buffer	75% Fixation / Permeabilization Diluent, 25% Fixation / Permeabilization Concentrate
Formalin 4%	160 ml Sörensen buffer, 20 ml formaldehyde solution
New Fuchsin solution	300 mg sodium nitrate, 7.5 ml aqua dest., 300 µl New Fuchsin stock solution, 150 ml TNT buffer, 800 µl naphthol AS-BI phosphate
New Fuchsin stock solution	2.5 g New Fuchsin, 50 ml 2 N hydrochloric acid

Percoll 37%	20 ml 10-fold PBS, 74 ml Percoll PLUS, 106 ml aqua dest.
Permeabilization buffer	90% aqua dest., 10% Permeabilization Buffer
Sirius Red solution	200 ml Sirius Red stock 0.1%, 10 ml glacial acetic acid
Sirius Red stock 0.1%	1 g Direct Red 80, 1000 ml water saturated picric acid
Sörensen buffer	3.03 g sodium dihydrogen phosphate monohy-drate, 14.14 g di-sodium hydrogen phosphate dihydrate, aqua dest.
TNT buffer	9 g sodium chloride, 6.35 g Trizma base, 25 ml hydrochloric acid, 1000 ml H_2O, 1 ml Tween 20
Washing buffer	1-fold PBS, 1% FCS, 1% EDTA (0.5 M)

7.5 Kits

Table 5: List of utilised kits

Kit	**Provider**
$CD4^+$ T Cell Isolation Kit mouse	Miltenyi Biotec (Bergisch Gladbach, Germany)
Chromium Next GEM Chip K Single Cell Kit	10x Genomics (Pleasanton, US)
Chromium Next GEM Single Cell 5’ Kit v2	10x Genomics (Pleasanton, US)
Dead Cell Removal Kit	Miltenyi Biotec (Bergisch Gladbach, Germany)
Dual Index Kit TT Set A	10x Genomics (Pleasanton, US)
Library Construction Kit	10x Genomics (Pleasanton, US)
Mouse TIM-1 (HAVCR1) ELISA Kit	Thermo Fisher Scientific (Waltham, US)
Multi Tissue Dissociation Kit 2	Miltenyi Biotec (Bergisch Gladbach, Germany)
NucleoSpin RNA Plus RNA isolation Kit	Macherey-Nagel (Düren, Germany)
ZytoChem Plus (AP) Polymer Kit	Zytomed Systems (Berlin, Germany)

7.6 RT-qPCR primers

Table 6: List of utilised RT-qPCR primers

Gene	Assay ID	Provider
Col1α1	Mm00801666 g1	Thermo Fisher Scientific (Waltham, US)

7.7 FACS antibodies

Table 7: List of utilised FACS antibodies

Antibody	Fluorochrome	Clone	Dilution	Provider
CD11b	AF700	M1/70	1000	BioLegend (San Diego, US)
	BV711	M1/70	200 250	BioLegend (San Diego, US)
CD11c	BV650	HL3	250	BD Biosciences (Franklin Lakes, US)
CD117	BV421	2B8	200	BioLegend (San Diego, US)
CD125 (IL-5Rα)	PE	DIH37	200	BioLegend (San Diego, US)
CD127	AF700	A7R34	250	eBioscience (San Diego, US)
CD161 (NK1.1)	Biotin	PK136	200	BioLegend (San Diego, US)
CD170 (SiglecF)	APC	E50-2440	200	BD Biosciences (Franklin Lakes, US)
	PE	E50-2440	200	BD Biosciences (Franklin Lakes, US)
CD183 (CXCR3)	BV450	CXCR3-173	100	BioLegend (San Diego, US)
CD19	BV785	1D3	250	BD Biosciences (Franklin Lakes, US)
	BV605	6D5	200	BioLegend (San Diego, US)
CD195 (CCR5)	PE	HM-CCR5	200	BioLegend (San Diego, US)
CD196 (CCR6)	APC	29-2L17	200	BioLegend (San Diego, US)
CD25	PE Cy7	PC61	200	BioLegend (San Diego, US)
	BV650	PC61	200	BioLegend (San Diego, US)
CD3	BV421	500A2	50	BD Biosciences (Franklin Lakes, US)
	BUV563	500A2	200	BD Biosciences (Franklin Lakes, US)

	PE	145-2C11	50	BioLegend (San Diego, US)
CD4	BUV496	RM4-5	200	BD Biosciences (Franklin Lakes, US)
	BUV740	GK1.5	200	Bio X Cell (Lebanon, US)
	BV421	RM4-4	200	BioLegend (San Diego, US)
	BV510	RM4-5	400	BioLegend (San Diego, US)
	BV650	RM4-5	200 400	BioLegend (San Diego, US)
CD44	BV785	IM7	330	BioLegend (San Diego, US)
CD45	AF700	HI30	100	BioLegend (San Diego, US)
	PerCP	30-F11	1000 1400	BioLegend (San Diego, US)
CD49b	PE Cy7	HMα2	800	BioLegend (San Diego, US)
CD62L	FITC	MEL-14	250	BioLegend (San Diego, US)
CD8	BV780	RPA-T8	400	BioLegend (San Diego, US)
	BUV805	53-6.7	200 330	BD Biosciences (Franklin Lakes, US)
F4/80	FITC	BM8	200	Invitrogen (Waltham, US)
	APC	BM8	200	eBioscience (San Diego, US)
Gr-1	PE Dazzle 594	RB6-8C5	250	BioLegend (San Diego, US)
IL-33R	BUV737	U29-93	200	BD Biosciences (Franklin Lakes, US)
Ly6C	APC Cy7	HK1.4	200	BioLegend (San Diego, US)
Ly6G	PE Cy7	1A8	200	BioLegend (San Diego, US)
γδTCR	BV605	GL3	250 330	BioLegend (San Diego, US)
	FITC	eBioGL3	100	eBioscience (San Diego, US)
NIR	APC Cy7	-	1000	Thermo Fisher Scientific (Waltham, US)
Zombie Aqua Dye	BV510	-	1000	BioLegend (San Diego, US)

7.8 Mouse lines

Table 8: List of utilised mouse lines

Mouse line	Description	Origin
C57BL/6J (strain 000664)	no genetic modifications	Jackson Laboratory (Maine, US)
C57Bl6/J_2019 wild type	no genetic modifications	Jackson Laboratory (Maine, US), bred by UKE animal facility (Hamburg, Germany)
C57Bl6/J_2022 wild type	no genetic modifications	Jackson Laboratory (Maine, US), bred by UKE animal facility (Hamburg, Germany)
Rag1KO_2018 (strain 002216)	homozygous for *Rag1*^{tm1Mom} mutation, no mature lymphocytes (T cells or B cells)	Jackson Laboratory (Maine, US), bred by UKE animal facility (Hamburg, Germany)

7.9 Softwares and databases

Table 9: List of utilised softwares and databases

Software or Database	Application
Adobe Illustrator	Design of figures
BioRender	Design of figures
Cell Ranger 10x Genomics	Single-cell sequencing data processing pipeline
FlowJo V10.10.0	Analysis of flow cytometry data, generation of UMAPs
GraphPad Prism V10	Generation of graphs, performance of statistical analyses
ImageJ	Calculation of percentage of fibrosis area in microscopy pictures
Illustrator 27.7	Design of graphs and figures
QuantStudio Design & Analysis 2	Analysis of real-time PCRs
RStudio V2023.3.1	Analysis of single-cell sequencing data
R package Seurat V5.2.1	Quality control and analysis of single-cell sequencing data

8 Methods

8.1 Animal experiments

8.1.1 Mouse models

C57BL/6J and Rag1KO mice were obtained from Jackson Laboratory and transferred to and bred in the animal facility of the University Medical Centre Hamburg-Eppendorf (UKE). Experimental mice and controls were bred separately in the same animal facility. In all experiments adult male and female mice older than 8 weeks were used. All animals were raised under specific pathogen-free conditions in an animal facility on a 12 h light / 12 h dark cycle. Standard animal feed and water were provided *ad libitum*, in case of critical weight loss mice additionally received supportive care in the form of fruit puree until the weights stabilised again. All animal experiments were performed according to national and institutional animal care and ethical guidelines and were approved by the local committees (approval number N024/2022, Behörde für Gesundheit und Verbraucherschutz, Freie und Hansestadt Hamburg).

8.1.2 Reproducibility

Animals were randomly assigned to different treatment groups without consideration for gender distribution, and all animal experiments were performed at least twice with similar results. Group allocations were known during the experiments, but analysis of histological samples was performed in a blinded fashion.

8.2 Application of DPBS or cisplatin

Kidney damage was induced by the application of 6 mg cisplatin per kg bodyweight to mice. Dissolved cisplatin was prepared by assuming an average weight of 25 g per mouse and calculating the amount of cisplatin needed for the total number of mice. The calculated amount of cisplatin was weighed in on a microscale and dissolved in the equal amount of 1-fold DPBS overnight on a rocking shaker. The next morning, the mice were weighed, and the weight was taken times six to calculate the individual final amount of cisplatin or respectively 1-fold DPBS. For injections cisplatin or DPBS was

slowly injected intraperitoneally into the lower left disinfected part of the mouse abdomen with a 0.30 mm diameter cannula.

8.3 Cell isolation from mouse kidneys

To isolate leukocytes from mouse kidneys, mice were killed by cervical dislocation whilst being under deep isoflurane anaesthesia. Mouse kidneys without the capsule were cut into small pieces and put in 5 ml complete medium. 20 µl Collagenase D and 10 µl DNase I were added, and the kidneys were enzymatically digested for 45 min at 37 °C while rotating on a MACSmix tube rotator. The cell suspension was further dispersed with the use of programs mSpleen 1.01 and mLung 2.01 of a GentleMACS dissociator and centrifuged at 360 g at 4 °C for 7 min. The supernatant was discarded, and the pellet resuspended in 5 ml Percoll. The next centrifugation step of 500 g brake 7 at RT for 10 min created a gradient allowing for leukocyte purification. Subsequent resuspension of the pellet with 1 ml erythrocyte lysis buffer, incubation for 8 min and stopping the reaction with DPBS enriched the leukocytes in the cell suspension. After filtering through a 50 µm nylon filter and washing with DPBS by centrifuging at 360 g at 4 °C for 7 min the cells were resuspended in 300-800 µl DPBS, depending on the pellet size.

8.4 Molecular methods

8.4.1. RNA isolation from mouse kidney tissue

RNA isolation was performed using the NucleoSpin RNA Plus Kit. About 30 mg of mouse kidney tissue were defrosted on ice and transferred to a 1.5 ml reaction tube. Per sample one Carbide Bead and 300 µl LBP buffer were added and on the Tissue Lyser II program 2 was used with a frequency of 30/s for 1 min. Reaction tubes were left on ice for 15 min until the foam was nearly gone. The following steps were done according to the kits protocol with using 40 µl of RNA-free water in the last step to eluate the RNA. The flow through was added a second time onto the column to increase RNA yield. The isolated RNA was stored at -80 °C.

8.4.2 Synthesis of complementary DNA

Hexamer primers were diluted 1:30 with aqua dest. The deoxynucleotide triphosphates (dNTP) mix was prepared by adding 5 µl adenosine triphosphate *(*ATP), guanosine triphosphate (GTP), cytidine triphosphate (CTP) and thiamine pyrophosphate (TPP) respectively to 80 µl aqua dest. RNA concentration was determined using a DS-11 Spectrophotometer and adjusted to 100 ng/µl with aqua dest. 4 µl of RNA per sample were added to the first mastermix consisting of 16 µl H_2O, 2 µl Random Hexamer Primers and 2 µl dNTP-Mix. A Thermocycler T3 was used to anneal primers to the RNA at 65 °C for 5 min. Samples were kept on ice and per sample 16 µl of the second mastermix, consisting of 8 µl 5-fold Reaction Buffer, 4 µl H_2O, 2 µl RevertAid Reverse Transcriptase and 2 µl RNaseOUT Ribonuclease Inhibitor, were added. Primers were further annealed and extended at 25 °C for 10 min, followed by DNA polymerisation at 42 °C for 1 h and enzyme deactivation at 70 °C for 15 min. Complementary DNA (cDNA) was stored at 4 °C or at -20 °C for longer time periods.

8.4.3 Real-time quantitative reverse transcription polymerase chain reaction

To quantify the amount of cDNA in the respective samples, 5 µl of PowerUp SYBR Green Master Mix or TaqMan Fast Universal PCR Master Mix were pipetted with 3.5 µl H_2O, 0.5 µl of specific murine primers and 1 µl of cDNA samples into 96 Fast PCR Plates. Plates were sealed and centrifuged at 100 RPM for 1 min. Real-time quantitative reverse transcription polymerase chain reaction (RT-qPCR) was performed for 45 cycles with initial denaturation at 95 °C for 10 min, followed by cycles of denaturation at 95 °C for 15 s, and primer annealing and elongation at 60 °C for 1 min. The analysis of RT-qPCRs was done with QuantStudio Design & Analysis 2.

8.4.4 Enzyme-linked immunosorbent assay KIM-1

Enzyme-linked immunosorbent assay (ELISA) for kidney injury molecule-1 (KIM-1) was performed using the Mouse TIM-1 (HAVCR1) ELISA Kit by Thermofisher Scientific. As a preparation all buffers, diluents, conjugates and solutions were diluted and put on RT. The standard was put in serial dilution according to the kits protocol. Urine from mice was obtained by putting the mice into metabolic cages for 4 hours and subsequently collecting the urine. Urine samples from mice that got injected with DPBS

were used in an undiluted manner, samples from mice that received cisplatin treatment were diluted according to the time point of urine collection (acute model dilution 1:50, transition from acute to chronic model dilution 1:10, chronic model dilution 1:5 or undiluted). 100 µl of samples and standard serial dilution were pipetted into the respective wells of the 96-well plate. The wells were covered and incubated for 2.5 h at RT while shaking at 350 rpm. The solutions were discarded, and the plate was washed four times with 300 µl washing buffer, making sure that the plate was tapped out thoroughly in between washing steps. 100 µl of biotin conjugate were added to each well, the wells were again covered, and the plate incubated for 1 h at RT while shaking at 350 rpm. The solutions were discarded, and the plate was washed four times with 300 µl washing buffer. 100 µl of Streptavidin-Horseradish peroxidase (HRP) were added to each well and the covered plate incubated for 45 min at RT while shaking at 350 rpm. The solutions were discarded, and the plate was washed four times with 300 µl washing buffer. After 100 µl of TMB substrate were added to each well, the plate was incubated for 20-30 min at RT in the dark, monitoring every 5 min whether a reaction of the substrate turning blue was visible in well S5. As soon as the sample in S5 turned blue, 50 µl Stop Solution was added to each well and the plate was analysed with a EL808 Ultra Microplate Reader at 450 nm wavelength.

8.4.5 Measurement of clinical parameters in blood

Blood was taken from mice under deep isoflurane anaesthesia with a 0.60 mm diameter cannula, subsequently mice were killed by cervical dislocation. The blood was quickly transferred into EDTA-coated microtubes. EDTA is acting as an anticoagulant and is therefore interrupting the clotting of the blood sample. Blood samples were centrifuged at 4000 rpm for 15 min at RT and the plasma was transferred into reaction tubes, which were stored at -20 °C until further analysis. For measurement at the COBAS Integra 400 plus blood samples were defrosted, vortexed and 120 µl of plasma per sample were transferred into COBAS samples cups. For samples not containing 120 µl of plasma, 60 µl of plasma were diluted with 60 µl aqua dest. The COBAS Integra 400 plus is a fully automated biochemical analyser which was used to measure levels of cholesterol, creatinine and urea (UREAL). By taking the UREAL values times 0.46 blood urea nitrogen (BUN) levels were obtained.

8.5 Flow cytometry

To characterise different immune cell subsets, cell suspensions obtained from cell isolation from mouse kidneys (9.3) were analysed using flow cytometry. Absolute $CD45^+$ cell numbers in cell suspension were determined by staining with fluorochrome-coupled anti-CD45 antibody combined with CountBright Absolute Counting Beads. For staining of surface and intranuclear markers 50 µl or 150 µl of each cell suspension were transferred onto a 96-well plate and washed two times with DPBS. Washing steps were performed by centrifuging at 360 g for 2 min at 8 °C. Dead cells were stained for 12 min at RT in the dark using NIR or Zombie Dye. After washing two times with MACS buffer, nonspecific antibody binding was prevented by incubation with 10% normal mouse serum for 10 min at 4 °C. Following another centrifugation step, the cells were incubated with surface staining antibodies for 25 min at 4 °C. Cell suspensions undergoing surface staining were washed with MACS buffer once, resuspended in 100 µl MACS buffer and analysed at FACSymphony A3. Cell suspensions being stained for intranuclear markers were washed with MACS buffer two times and incubated in Fixation / Permeabilization buffer for 25 min at RT in the dark to fixate the cells and enable antibodies to reach intracellular targets. Subsequent to two washing steps with Permeabilization buffer, the cells were incubated with intranuclear staining antibodies (diluted in Permeabilization buffer) for 45 min at 4 °C. Cell suspensions were washed once with DPBS, once with MACS buffer, resuspended in 100 µl MACS buffer and analysed at FACSymphony A3.

8.6 Cell sorting & transfer of sorted $CD4^+$ T cells

Mice homozygous for the *Rag1*^{tm1Mom} mutation (Rag1KO_2018 mice), containing no mature lymphocytes, were transferred with isolated $CD4^+$ T cells. To isolate the $CD4^+$ T cells, spleens from healthy wildtype B6 donor mice were isolated without fat and put into 1.5 ml reaction tubes filled with DPBS on ice, pooling two spleens per reaction tube. The spleens were then mashed with pistons of 5 ml syringes through 70 µm nylon meshes into 50 ml falcon tubes. Meshes were rinsed with MACS buffer and after centrifugation at 360 g for 7 min at 4 °C supernatants were discarded. Pellets were resuspended in 2 ml erythrocyte lysis buffer each and incubated for 8 min. The cell suspensions were filtered through 50 µm nylon filters into new 15 ml falcons, old tubes

and meshes were washed with 9 ml DPBS. After another centrifugation step at 360 g for 7 min at 4 °C, the supernatants were discarded again, and the cells resuspended in 20 ml DPBS. The number of alive cells within a size range of 4-16 µm was determined using the TC20 Automated Cell Counter. For this purpose, 10 µl of each of the pooled samples were mixed with 10 µl Trypan Blue stain 0.4% and measured. The $CD4^+$ T Cell Isolation Kit mouse by Miltenyi Biotec was used for manual magnetic labelling and subsequent manual separation with LS MACS columns (maximal number of labelled cells 10^8) via magnetic activated cell sorting (MACS). The samples were resuspended in 40 µl MACS buffer per 10^7 cells, and 10 µl Biotin-Antibody Cocktail per 10^7 cells were added to label all immune cells except for $CD4^+$ T cells. After incubation in the fridge for 5 min, 30 µl MACS buffer per 10^7 cells and 20 µl Anti-Biotin MicroBeads per 10^7 cells were added and the cell suspensions were incubated in the fridge for 10 min. For subsequent manual cell separation, LS Columns were placed in the magnetic field of a QuadroMACS Separator on a MACS MultiStand. Columns were rinsed with 3 ml of MACS buffer and the cell suspensions were applied onto the columns. The flow-throughs containing unlabelled enriched $CD4^+$ T cells were collected in falcons; the columns were washed with 3 ml MACS buffer and the flow-throughs collected.
Rag1KO_2018 mice received 1.000.000 of the sorted enriched $CD4^+$ T cells each. For preparation, the tails were warmed up with a red-light lamp. Cell suspensions were slowly injected into the tail vein with a 0.30 mm diameter cannula.
The sorting purity was checked via flow cytometry. For this an aliquot of sorted cells was transferred onto a 96-well plate, washed two times with DPBS and stained with NIR antibody for 12 min at RT in the dark for cell viability. The plate was washed twice with MACS buffer and nonspecific antibody binding was prevented by incubation with MS for 10 min at 4 °C. After a centrifugation step, cells were stained with fluorochrome-coupled antibodies against CD45, CD3, CD4, CD8 and CD11b for 25 min at 4 °C, washed with MACS buffer and after resuspension in 100 µl of MACS buffer analysed at FACSymphony A3.

8.7 Single-cell RNA sequencing

8.7.1 Sequencing of total kidney cells

For cell isolation of total kidney cells, the Multi Dissociation Kit 2 was used. Kidneys were removed without capsules, quartered on a glass surface and transferred into C tubes with 4.8 ml Buffer X on ice. 50 µl Enzyme P, 50 µl Buffer Y, 100 µl Enzyme D and 20 µl Enzyme A were added and GentleMACS Dissociator programme 37C Multi E01 was used for 30 min to enzymatically digest the kidney tissues. Cell suspensions were filtered through a 100 µm nylon filter into new 50 ml falcons and C tubes and filters were washed with 15 ml DPBS. After centrifugation at 150 g at 4 °C for 10 min, supernatants were discarded. Cells were resuspended in 2 ml of erythrocyte lysis buffer, incubated for 5 min, filtered through 40 µm filters and washed with 15 ml DPBS + 0.04% BSA. After a centrifugation step at 150 g at 4 °C for 10 min, supernatants were discarded and cells resuspended in PBS + 0.04% BSA (week 15 PBS mice in 2 ml and cisplatin mice in 3 ml, month 8 PBS mice in 3 ml and cisplatin mice in 4 ml). The number of alive cells in the respective samples was determined with a Neubauer chamber. 10 µl of cells from each sample were mixed with 90 µl Trypan Blue stain 0.4% and counted on an Eclipse TS100 microscope with 10-fold magnification. The average alive cell number after cell isolation was calculated as in the following: cell number/ml = average x dilution factor x 10^4 cells/ml.

To reduce the percentage of dead cells in the samples, the Dead Cell Removal Kit was deployed. Cell suspensions were centrifuged at 150 g at 4 °C for 10 min and supernatants were discarded. 100 µl of MicroBeads were added per 10^7 cells, samples were topped up to 500 µl with onefold Binding Buffer and incubated at RT for 15 min. LS Columns were placed in the magnetic field of a QuadroMACS Separator on a MACS MultiStand and prepared with 3 ml of onefold binding buffer. Cell suspensions were added onto the columns and flow-throughs containing unlabelled cells were collected. Columns were washed four times with 3 ml binding buffer and flow-throughs again collected. The percentage of dead cells was checked with a Neubauer chamber and the whole dead cell removal procedure was repeated a second time to get the percentage of alive cells to a minimum of 70%. Cell stock concentrations were adjusted to 700-1200 cells/µl.

8.7.2 Sequencing of CD45$^+$ leukocytes

Cell isolation from mouse kidneys took place as described in detail in 9.3. Kidney pieces were enzymatically digested in complete medium with added Collagenase D (final concentration 0.4 mg/ml) and DNase I (final concentration 100 µg/ml) for 45 min at 37 °C. After further dispersion in a GentleMACS, cells were pooled into four groups (week 15 three PBS and four cisplatin samples, month 8 four PBS and six cisplatin samples) by pooling 1.5 ml from every sample included in one group into a 15 ml falcon. No Percoll gradient was used for cell isolation of CD45$^+$ leukocytes for single-cell RNA sequencing as it would exclude myeloid cells. Following centrifugation at 360 g at 4 °C for 7 min, the supernatants were discarded, and the respective pellets resuspended in 5 ml of erythrocyte lysis buffer. After 5 min the cell suspensions were filtered through a 50 µm nylon filter into new 15 ml falcons and the old tubes and meshes were washed with 9 ml DPBS. Cell suspensions were centrifuged at 360 g at 4 °C for 7 min and resuspended in 900 µl DPBS / FCS for subsequent staining of surface proteins.
Cells were stained with NIR antibody for 12 min at RT in the dark for cell viability. The plate was washed twice with DPBS / FCS and nonspecific antibody binding was prevented by incubation with MS for 15 min at 4 °C. After a centrifugation step, cells were stained with fluorochrome-coupled antibodies against CD19, SiglecF, CD45, Ly6G, F4/80, CD4, γδTCR, CD11b, CD8, MHCII and CD3 for 25 min at 4 °C and washed once with DPBS / FCS. Cells were filtered through a 40 µm filter, old tube and filter were washed with 9 ml DPBS / FCS, centrifuged and the supernatant was taken off. Cell pellets were resuspended in 1.5 ml PBS / FCS.
Sorting was performed at a FACS Aria Fusion Flow Cytometer with a 100 µm nozzle at the lowest flow rate. For each of the four groups approximately 60.000 cells were sorted.

8.7.3 Barcoding of cells and Gene Expression Library construction

The UKE Single Cell Core Facility used the 10X Genomics Chromium Controller and the Chromium Next GEM Single Cell 5’ Reagent Kits v2 to prepare the samples for single-cell sequencing (protocol CG000331). For the total kidney cells samples the number of input cells was 40.000 with an estimated number of 12.000 recovered cells, corresponding to 30% recovery, for the CD45$^+$ leukocytes samples the number of input

cells was 30.000 with an estimated number of 9.000 recovered cells, likewise corresponding to 30% recovery. Per cell 20.000 reads were performed.
The first step was the generation of Gel Beads-in-emulsion (GEMs) by combining barcoded Single Cell VDJ 5' Gel Beads, a master mix with cells, and partitioning oil onto a Chromium Next GEM Chip K. Incubation of the GEMs in a Chromium Controller produced 10x barcoded full-length cDNA from poly-adenylated mRNA, which was amplified via PCR in a thermocycler. The amplified cDNA was used to generate single-cell 5' Gene Expression (GEX) Libraries. Finally, eight generated GEX Libraries were sent to Novogene for single cell sequencing.

8.8 Histological stainings

Mice were killed by cervical dislocation whilst being under deep isoflurane anaesthesia. Per mouse a small piece of one of the kidneys was cut and put into 5 ml of formalin 4% overnight. On the next day the kidney pieces were washed with DPBS three times. After fixation the kidney pieces were embedded in paraffin and hardened. For different immunological stainings 3 µm thick sections were cut from each of the paraffin blocks.

8.8.1 Caspase 3 staining

Paraffin-embedded sections were deparaffinised with a descending series of alcohol and washed with aqua dest. three times for 5 min. 1-fold Dako buffer (pH 9.0) for antigen unmasking and epitope recovery was heated for 30 min in a steam cooker and sections were placed inside for 15 min at 90 °C. After sections cooled down for 30 min at RT, they were washed with aqua dest. three times for 5 min and the tissue cuts were framed with a Dako Pen to keep the solutions on top of the tissue. Sections were incubated with DPBS + 0.2% Tween 20 three times for 5 min, blocked for 5 min using 50 µl of the blocking buffer from the ZytoChem Plus (AP) Polymer Kit and then washed two times for 4 min with PBS + 0.2% Tween 20. The primary Caspase 3 antibody was diluted 1:200 in Zytomedbuffer from the ZytoChem Plus (AP) Polymer Kit and the sections were incubated with 50 µl of the antibody overnight in a wet chamber in the fridge. The next morning the sections were washed with DPBS + 0.2% Tween three times for 5 min. 40 µl of secondary antibody undiluted Anti-Rabbit AP Komplex from the Polap Kit 1 were applied for 30 min at RT onto the sections. Sections were washed with DPBS

+ 0.2% Tween three times for 5 min, kept under running water for 1-2 min and incubated in Neufuchsin solution for 10-15 min in the dark. Slides were washed with running water and incubated in Böhmer's hematoxylin solution for 2-3 min to stain cell nuclei. Slides were washed with running water until it became clear, shortly swivelled three times in hydrochloric acid for differentiation, washed with running water for 2 min and covered with gum arabic and coverslips.
Tissue sections were analysed using an Axio Scope A1 microscope. Using 20-fold magnification, in each tissue section Caspase 3 positive cells, which were stained in dark red, were counted in ten fields of vision around the cortex. The average number of Caspase 3 positive cells per sample was then plotted in a graph using GraphPad Prism.

8.8.2 CD3 staining

Paraffin-embedded sections were deparaffinised with a descending series of alcohol and washed with aqua dest. three times for 5 min. 1-fold Dako buffer (pH 9.0) for antigen unmasking and epitope recovery was heated for 30 min in a steam cooker and sections were placed inside for 15 min at 90 °C. After sections cooled down for 30 min at RT, they were washed with aqua dest. three times for 5 min and the tissue cuts were framed with a Dako Pen to keep the solutions on top of the tissue. Sections were incubated with DPBS + 0.2% Tween 20 three times for 5 min, blocked for 5 min using 50 µl of the blocking buffer from the ZytoChem Plus (AP) Polymer Kit and then washed two times for 4 min with PBS + 0.2% Tween 20. The primary polyclonal rabbit anti-human CD3 antibody was diluted 1:1000 in Zytomedbuffer from the ZytoChem Plus (AP) Polymer Kit and the sections were incubated with 50 µl of the antibody overnight in a wet chamber in the fridge.
The next morning the sections were washed with DPBS + 0.2% Tween three times for 5 min. 50 µl of secondary antibody undiluted Anti Rabbit AP Komplex from the Polap Kit 1 were applied for 30 min at RT onto the sections. Sections were washed with DPBS + 0.2% Tween three times for 5 min, kept under running water for 1-2 min and incubated in Neufuchsin solution for 15-20 min in the dark. Slides were washed with running water and incubated in Böhmer's hematoxylin solution for 2-3 min to stain cell nuclei (incubation was repeated up to three times depending on staining result). Slides were washed with running water until it became clear, shortly swivelled three times in

hydrochloric acid for differentiation, washed with running water for 2 min and covered with gum arabic and coverslips.
Tissue sections were analysed using an Axio Scope A1 microscope. Using 20-fold magnification, in each tissue section CD3 positive cells, which were stained in dark red, were counted in 20 fields of vision around the cortex. The average number of CD3 positive cells per sample was then plotted in a graph using GraphPad Prism.

8.8.3 Sirius Red staining

Paraffin-embedded sections were deparaffinised with a descending series of alcohol and washed with aqua dest. three times for 5 min. Slides were incubated in Sirius Red solution for 60 min, afterwards the staining rack holding the slides was dipped five times first into acidified aqua dest, then into aqua dest for 10 sec respectively. Slides were incubated in Fast Green solution for 60 min, then the staining rack was washed with acidified aqua dest for 60 sec, followed by washing in aqua dest for 10 sec. For dehydration, slides were dipped once shortly in 70% ethanol until streaks disappeared, then three times in 96% ethanol. Incubations in 100% ethanol for 2 min, 5 min and 10 min were followed by incubation in 3-fold xylene for 5 min. Slides were covered with Eukitt as a water-free mounting medium and coverslips.
Tissue sections were analysed using an Axio Scope A1 microscope and an AxioCam MRc to take pictures of the stained tissue sections. Using 20-fold magnification, in each tissue section ten images around the cortex were taken. Additionally, one test image with clearly positive Sirius Red staining (e.g., near arteries) and one image with no stained collagen were taken. Pictures were saved in a Tagged Image File Format (tif format). Collagen was stained red, erythrocytes were stained yellow, and muscle, cytoplasm and mucus were stained green.
To quantify the extension of fibrosis in different samples, the image editing programme ImageJ with the plugin Color Deconvulution2 and the macro Sirius Red was used. ImageJ was started and the positive test image opened in the programme. The path used was Image → Color → Color Deconvulution2 → Vectors H HRP-Green New Fuchsin → Output RGB_Keep_C2 → Simulated LUTs, Cross product for colour 2, Hide legend → OK. Under Image the type was set to 8 Bit, so that the picture appeared grey. For setting the threshold, the upper scale was set to 0, the lower scale was set to a number at which collagen fibers were stained in dark red, but nuclei and glomeruli were negative for Sirius Red staining. The above steps were repeated with the test

image taken from an area of the cortex without Sirius Red stained collagen fibers. The macro Sirius Red was opened in ImageJ and the threshold numbers were changed to the ones determined with the two test images. The ten pictures that were taken around the cortex were opened in ImageJ and the macro was run for each of them individually. The average area of fibrosis per sample was then plotted in a graph using GraphPad Prism.

Sirius Red stainings have a high signal to noise ratio, meaning that background staining and nonspecific binding of the staining antibody is negligible [123].

8.9 In silico methods

8.9.1 Analysis of single-cell RNA sequencing

The Cell Ranger software pipeline (10x Genomics) was utilised to perform demultiplexing of cellular barcodes and mapping of reads to the reference genome (refdata-gex-mm10-2020-A, function cellranger count). The matrices of cells and the unique molecular identifier (UMI) count were obtained and further processed by the R package Seurat. As a quality control step cells with less than 50 genes (in the total kidney approach) or less than 100 genes (in the $CD45^+$ cells approach), more than 3.000-4.000 genes (to remove potential doublets) and more than 40% (total kidney approach) or more than 5% ($CD45^+$ cells approach) mitochondrial genes were filtered out. The Seurat package was used to perform unsupervised clustering analysis on scRNA-seq data. Gene counts for cells that passed quality control were normalised by library size and log-transformed (function NormalizeData, normalization.method = "LogNormalize", scale.factor = 10000). Then, highly variable genes were detected (function FindVariableFeatures, selection.method = "vst", nfeatures = 3000). Batch effects were reduced via Seurat integration method (harmony package). The integrated matrix was scaled by the ScaleData function (default parameters), and principal-component analysis was performed to reduce dimensionality (function RunPCA, npcs of 10-30).

Principal components were determined by using the ElbowPlot function and used to compute the KNN graph based on the Euclidean distance (function FindNeighbors), which then generated cell clusters using the function FindClusters (resolution = 0.01-1). Unsupervised Uniform Manifold Approximation and Projection (UMAP) clustering

was used to visualize clustering results. The top differential expressed genes in each cluster were found using the FindAllMarkers function (min.pct = 0.1) and running Wilcoxon rank-sum tests. The differential expression between clusters or groups was calculated by the FindMarkers function (min.pct = 0.1), which also included Wilcoxon rank-sum tests. To assess the stress signalling score, the function AddModuleScore was used, which calculates a composite expression score by averaging the gene expression of a pre-defined gene set including genes *Havcr1* [124], *Lcn2* [125], *Wnt4* [126], *Hmox1* [127], *Casp3* [128], *Trp53* [129], *Cdkn1a* [130], *Slc25a21* [131], *Tead1* [132], *Cldn16* [133], *Apobec1* [134], *Gsta3* [135], *Ambp* [136], *Clu* [137] and subtracting the average expression of 100 randomly selected control gene sets.

8.9.2 Statistical analysis

For the generation of graphs and statistical analysis of data the software GraphPad Prism V10 was used. For comparison between two groups the unpaired Student's *t* test was used, which compares the means of two groups. In case of three or more groups an ordinary one-way ANOVA was applied (no matching or pairing, comparison of the mean of each column with the mean of every other column as a follow up test), which works by comparing the differences among group means with the pooled standard deviations of the groups. If not stated otherwise data distribution was assumed to be normal without it being formally tested. Data collection and analysis was performed blind to the conditions of the experiments. No data points were excluded.
The respective significances were displayed in graphs with asterisks. A p value of < 0.05 was considered to be statistically significant (*), accordingly $p < 0.01$ equals to **, $p < 0.001$ equals to *** and $p < 0.0001$ equals to ****.

9 Results

9.1 Experimental setup of cisplatin-induced AKI to CKD mouse model

The cisplatin dose-finding process was performed in the laboratory prior to the start of the doctoral thesis at hand. Kidney damage was induced by two intraperitoneal applications of 6 mg cisplatin per kg bodyweight to B6 mice with an interval of 7 days, a control group of B6 mice treated with DPBS was included. Kidneys were harvested at six different time points (Figure 7).

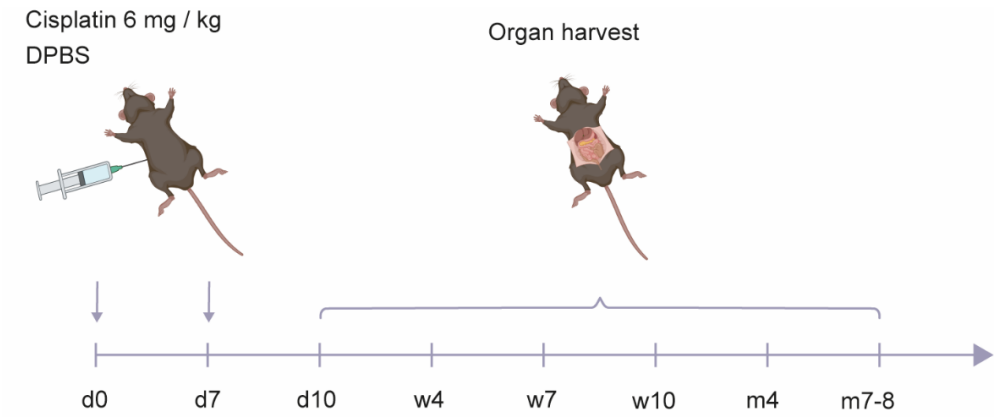

Figure 7: Experimental setup of cisplatin-induced AKI to CKD mouse model.
Timepoints of organ harvests indicate respective timepoints after the first cisplatin injection at day 0 (d = day, w = week, m = month).

9.2 Low-dose cisplatin application induces severe AKI that resolves

Several clinical markers were used to characterise kidney injury and functional impairment induced by two low-dose cisplatin injections.

In the healthy kidney, kidney injury molecule-1 (KIM-1), a transmembrane glycoprotein, is expressed at very low levels [138], but after toxic or ischemic renal damage, its expression is markedly upregulated on renal proximal tubule epithelial cells (PTECs) undergoing regeneration. Since the extracellular domain of KIM-1 is cleaved following injury, the soluble form of KIM-1 is detected in higher amounts in urine, rendering KIM-1 a

suitable biomarker for AKI which is classically characterised by proximal tubular damage [139, 140].

In comparison to DPBS-treated control mice, levels of KIM-1 in the urine of cisplatin-treated mice were significantly upregulated by a factor of 10 at the day 10 time point (Figure 8a), demonstrating that the chosen cisplatin concentration was suitable to cause severe damage to renal proximal tubule epithelial cells.

The time course of urine KIM-1 ELISAs (Figure 8b) showed that this initial kidney injury improved between the day 10 and week 4 time points, indicating that PTECs were recovering from injury after the second cisplatin hit [141]. From the week 10 time point on, levels of KIM-1 detectable in the urine of cisplatin-treated mice returned back to control levels, implying that the recovery of renal tissue from acute injury was finalised (Figure 8a, b).

Blood urea nitrogen (BUN) is a waste product of protein metabolism. It is commonly used as an indirect marker of renal excretory function, reflecting glomerular filtration rate (GFR) among other factors, that is routinely used in clinical settings [142, 143].

In the low-dose cisplatin-induced AKI to CKD mouse model, BUN levels were elevated in cisplatin mice compared to DPBS control mice (Figure 8c), demonstrating a functional impairment of excretory kidney function as a hallmark feature of severe AKI. From the time point of 4 weeks on, BUN levels of cisplatin mice returned back to the levels of DPBS control mice, again indicating resolution of AKI.

To demonstrate the cell-damaging effects of two low-dose cisplatin injections histologically in renal tissue samples, caspase-3 staining was used (Figure 8d). Activated caspase-3, a cysteine-aspartic acid protease, is a key player in the apoptotic pathway. After activation by upstream initiator caspases, caspase-3 cleaves a broad range of cellular targets, coordinating the degradation of cellular components and consequently executing programmed cell death [144]. The detection of activated caspase-3 is therefore a highly sensitive method for identifying apoptotic cells in tissues, even before other morphological features of apoptosis occur [145].

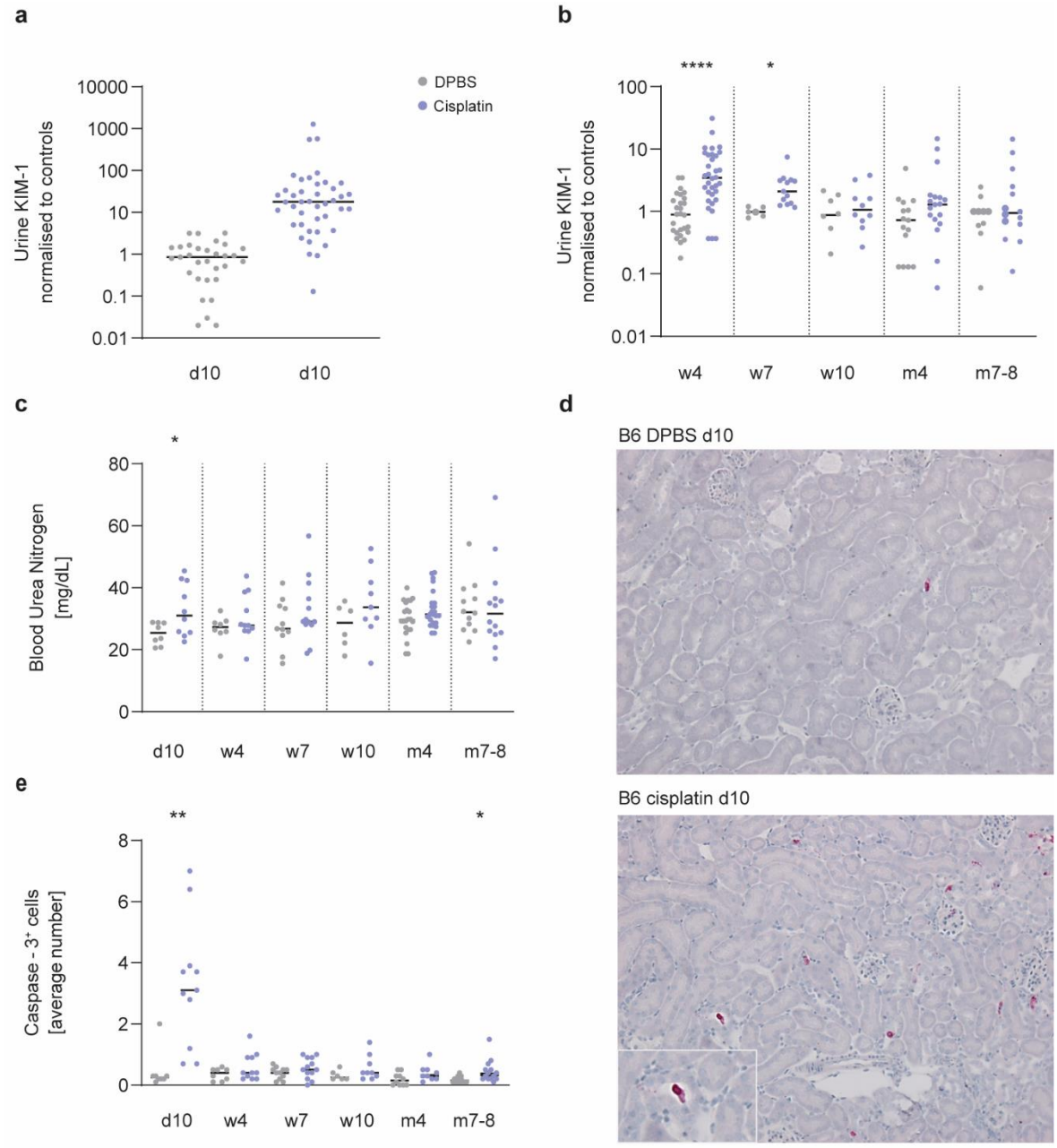

Figure 8: Low-dose cisplatin application induces severe AKI that resolves.
a-b KIM-1 levels in urine of DPBS- and cisplatin-treated B6 mice, measured by ELISA. DBPS samples were used undiluted, cisplatin samples were diluted according to respective time points (d10 DPBS *n* = 31, cisplatin *n* = 42, w4 DPBS *n* = 28, cisplatin *n* = 34, w7 DPBS *n* = 6, cisplatin *n* = 13, w10 DPBS *n* = 8, cisplatin *n* = 10, m4 DPBS *n* = 15, cisplatin *n* = 18, m7-8 DPBS *n* = 10, cisplatin *n* = 14). **c** BUN levels in blood of DPBS- and cisplatin-treated B6 mice, determined by COBAS analyser (d10 DPBS *n* = 8, cisplatin *n* = 10, w4 DPBS *n* = 8, cisplatin *n* = 11, w7 DPBS *n* = 11, cisplatin *n* = 13, w10 DPBS *n* = 6, cisplatin *n* = 9, m4 DPBS *n* = 16, cisplatin *n* = 17, m7-8 DPBS *n* = 12, cisplatin *n* = 14). **d** Representative photomicrographs of kidney sections from DPBS- and cisplatin-treated B6 mice on day 10 stained with caspase-3 staining, 20-fold magnification, zoomed in section 40-fold magnification. **e** Quantification of caspase-3 staining in kidney tissue of DPBS- and cisplatin-treated B6 mice (d10 DPBS *n* = 8, cisplatin *n* = 11, w4 DPBS *n* = 8, cisplatin *n* = 11, w7 DPBS *n* = 11, cisplatin *n* = 13, w10 DPBS *n* = 6, cisplatin *n* = 9, m4 DPBS *n* = 10, cisplatin *n* = 9, m7-8 DPBS *n* = 12, cisplatin *n* = 14). *n* represents number of biologically independent animals, symbols represent individual animals. Bars represent median. Unpaired Student's *t* test was used to compare treatment groups at respective time points.

Quantification of caspase-3 positive cells showed a significant increase in apoptotic tubular cells at day 10 after the first cisplatin injection (Figure 8e). As indicated by normalisation of caspase-3-positive cell numbers at week 4, damaged proximal tubule cells rapidly recovered from acute injury induced by low-dose cisplatin injections.
Notably, a significant increase in the number of caspase-3-positive cells was observed again 7-8 months following the initial cisplatin administration. The increase in apoptotic cells suggests the presence of secondary tissue damage which appears to be independent of the direct cytotoxic effects of cisplatin treatment.

In total, analysis of clinical markers demonstrated that the cisplatin injections were sufficient to cause severe AKI, while still enabling mice to survive beyond 72 hours, which is the end-point of standard dosing models using >20 mg of cisplatin [146]. The acute kidney injury induced by the cisplatin model of this thesis seemed to clinically resolve in the timeframe between the day 10 and week 4 time points, resulting in kidney function levels of cisplatin-treated mice that were comparable to DPBS-treated control mice.

9.3 Long-term consequences of cisplatin-induced AKI

In order to investigate potential long-term consequences of cisplatin-induced AKI beyond the initial resolution phase (AKI to CKD transition), kidney tissue was analysed at late time points following cisplatin injections.
Interstitial fibrosis is one of the critical components for progression of chronic kidney disease and is characterised by excessive production and deposition of ECM proteins (mainly various isoforms of collagen) at the fibrotic site [147]. Kidney fibrosis throughout the 8 month time course was assessed for deposition of collagen, especially collagen I and III fibrils, via Sirius Red staining (Figure 9a) [148].

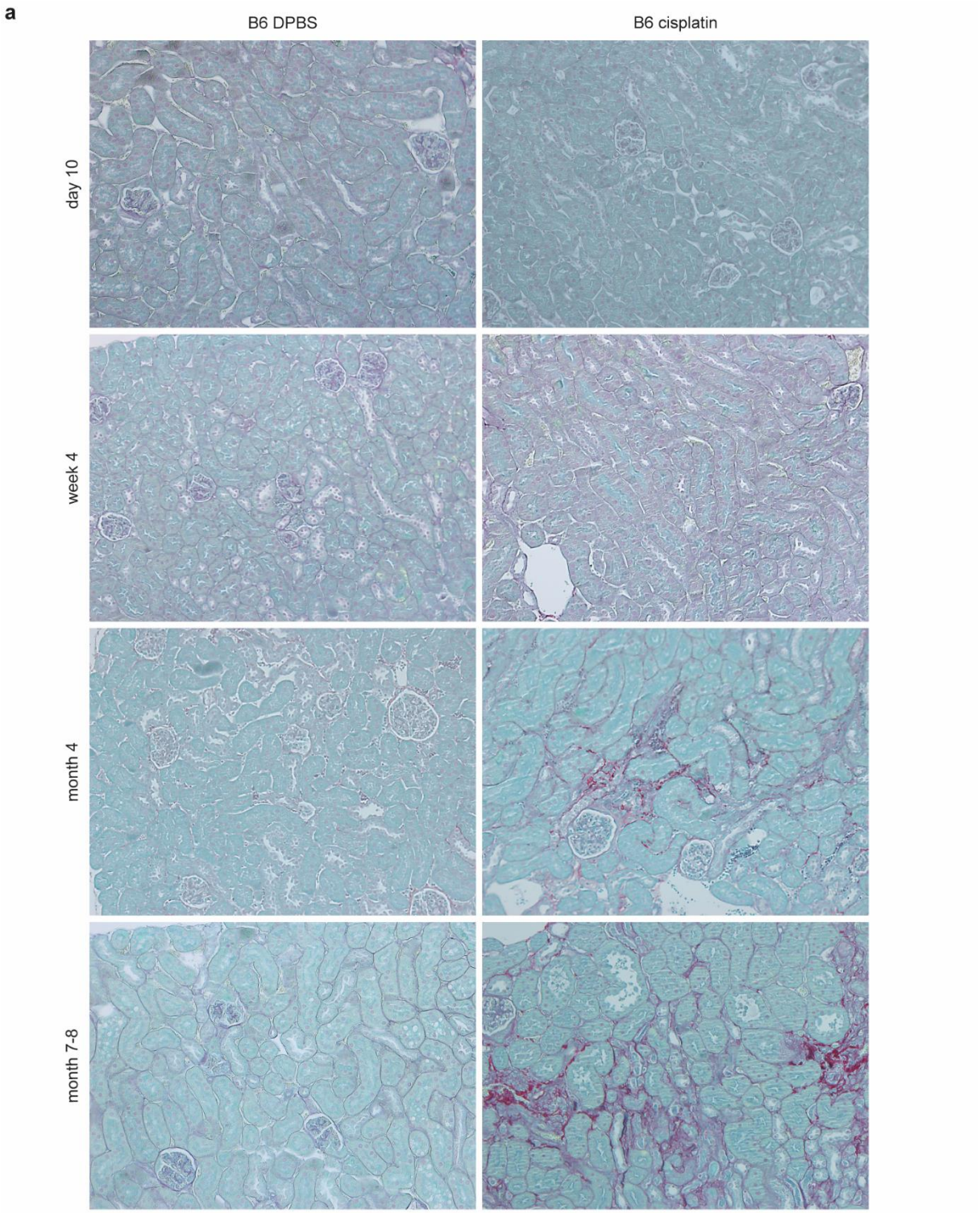
a
B6 DPBS
B6 cisplatin
day 10
week 4
month 4
month 7-8

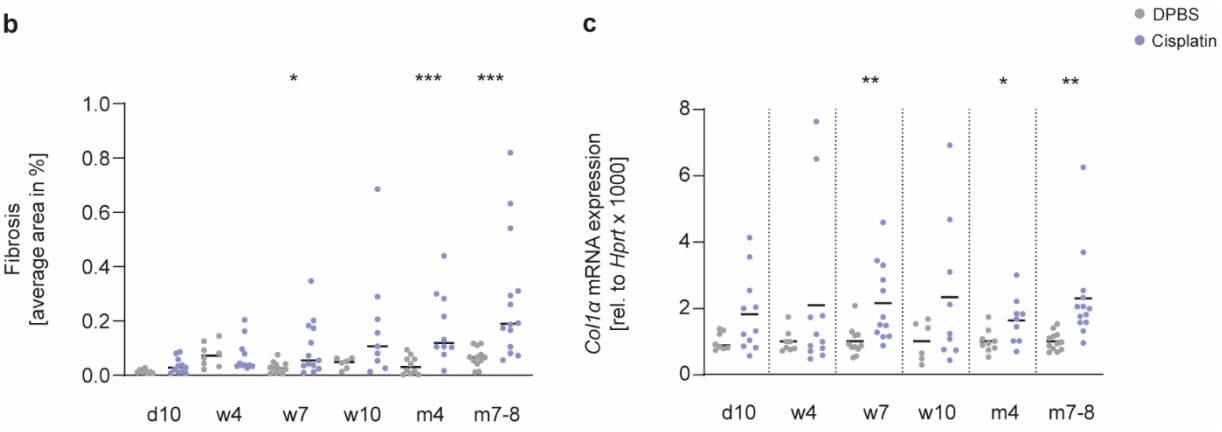

Figure 9: Severe low-dose cisplatin-induced AKI causes long-term consequences.
a Representative photomicrographs of kidney sections from DPBS- and cisplatin-treated B6 mice on day 10, week 4, month 4 and month 7-8 of AKI stained with Sirius Red staining (dark red), 20-fold magnification. **b** Quantification of Sirius Red staining in kidney tissue of DPBS- and cisplatin-treated B6 mice through determination of average percental fibrosis area by ImageJ (d10 DPBS *n* = 8, cisplatin *n* = 11, w4 DPBS *n* = 8, cisplatin *n* = 11, w7 DPBS *n* = 11, cisplatin *n* = 13, w10 DPBS *n* = 6, cisplatin *n* = 9, m4 DPBS *n* = 10, cisplatin *n* = 10, m7-8 DPBS *n* = 12, cisplatin *n* = 14). **c** *Col1α* gene expression in kidney tissue of DPBS- and cisplatin-treated B6 mice, normalised to the housekeeping gene *Hprt* (d10 DPBS *n* = 8, cisplatin *n* = 11, w4 DPBS *n* = 8, cisplatin *n* = 10, w7 DPBS *n* = 11, cisplatin *n* = 12, w10 DPBS *n* = 6, cisplatin *n* = 9, m4 DPBS *n* = 9, cisplatin *n* = 9, m7-8 DPBS *n* = 12, cisplatin *n* = 13). *n* represents number of biologically independent animals, symbols represent individual animals. Bars represent median. Unpaired Student's *t* test was used to compare DBPS-treated mice with cisplatin-treated mice at respective time points.

Quantification of histological images showed increasing fibrosis in cisplatin-injected mice over the time course as compared to DPBS-injected mice (Figure 9b). From week 7 on, the quantified average area of fibrosis was significantly increased, reaching an almost 10-fold increase at the month 7-8 time point. The slight increase in average fibrosis area in DPBS-treated control mice towards the month 7-8 time point is linked to natural aging of the mice, which is accompanied by development of renal fibrosis [149].

The rate of collagen production in transition of clinically resolved AKI to CKD was additionally examined on mRNA level via RT-qPCR analysis of *Col1α* expression (Figure 9c). Overall, the results of *Col1α* expression reflect the pattern of the determined average fibrosis area, although the spread of samples at respective time points is higher in RT-qPCR analysis than in histological quantification.

In summary, analysis of clinical markers and histological images obtained by this newly established model demonstrated that two low-dose cisplatin injections in mice induce severe acute kidney injury that resolves over a period of four weeks. At late time points (after week 7-10) cisplatin-treated mice developed progressive kidney fibrosis, a hallmark of CKD, displaying the suitability of the model to study AKI to CKD transition.

9.4 T cell infiltration in the resolution phase of AKI

To elucidate potential mechanisms initiating AKI to CKD transition in the newly characterised model, the role of immune cells in this process was examined. Mature T cells are identified, among other markers, by presence of the surface marker CD3. Since it is known that $CD3^+$ T cells are activated and migrate to the injured kidney during AKI and subsequently can influence the outcome of acute kidney damage [150, 151], it was decided to have a closer look at $CD3^+$ T cell numbers in transition of AKI to CKD.
An immunohistochemical staining of $CD3^+$ T cells was performed (Figure 10a) and using 10-fold magnification, the average number of $CD3^+$ T cells was counted in 20 fields of vision around the cortex (Figure 10b). Except at week 10, $CD3^+$ T cell numbers were significantly higher in cisplatin-treated mice compared with DPBS-treated control mice at all organ harvest time points. Notably, the difference in $CD3^+$ T cell counts between cisplatin- and DPBS-treated groups was most pronounced at the week 4 and week 7 time points. At week 4, a considerable spread in the data was observed, indicating that some cisplatin-treated mice had a more pronounced infiltration of $CD3^+$ T cells into the kidney than other mice receiving the same treatment. The number of $CD3^+$ T cells in cisplatin-treated mice declined slightly after week 7; however, at the experimental endpoint of 7-8 months, renal $CD3^+$ T cell numbers of cisplatin-treated mice still remained slightly elevated compared with $CD3^+$ T cell numbers observed at day 10 post-cisplatin injections.

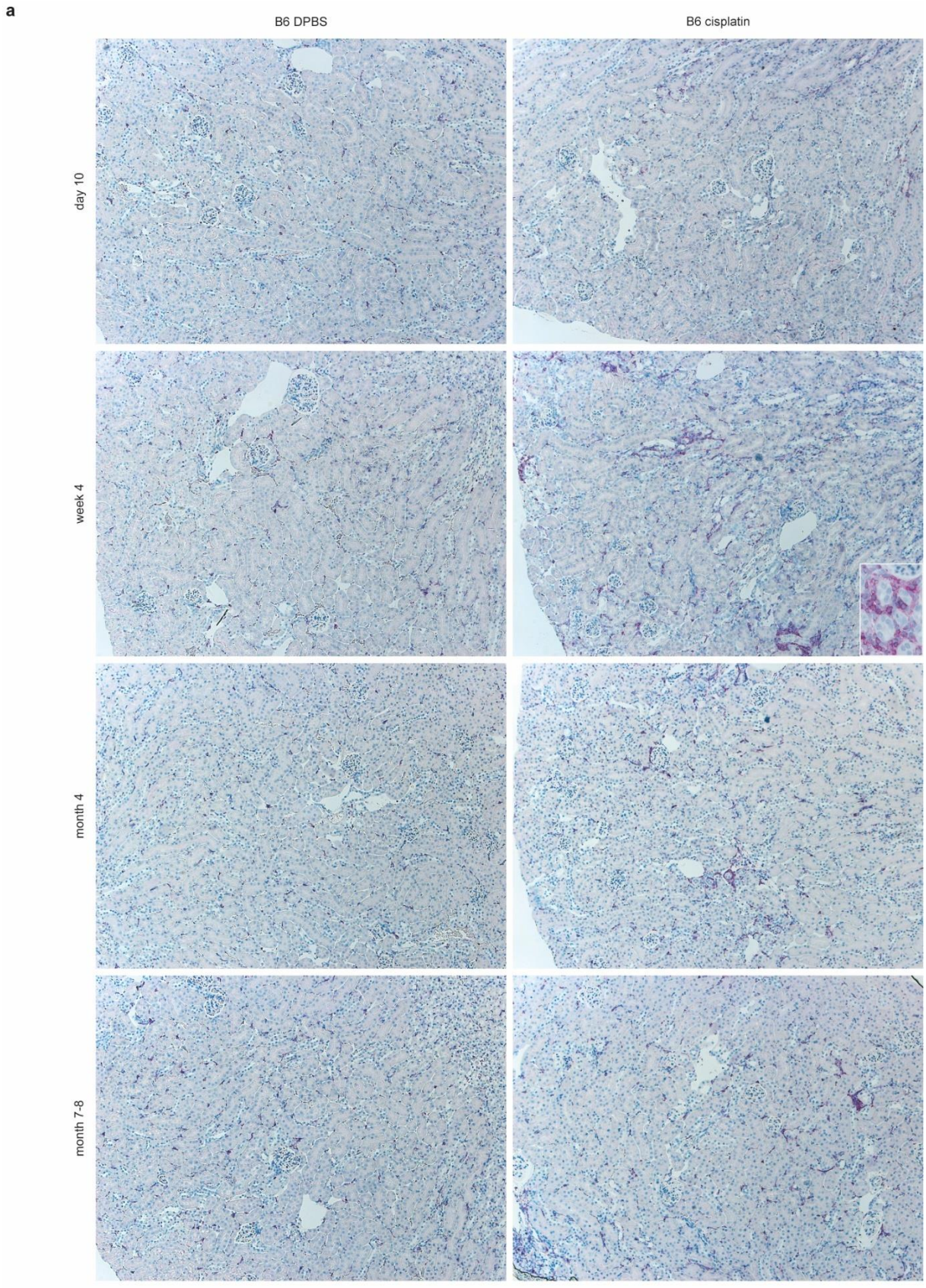
a
B6 DPBS
B6 cisplatin
day 10
week 4
month 4
month 7-8

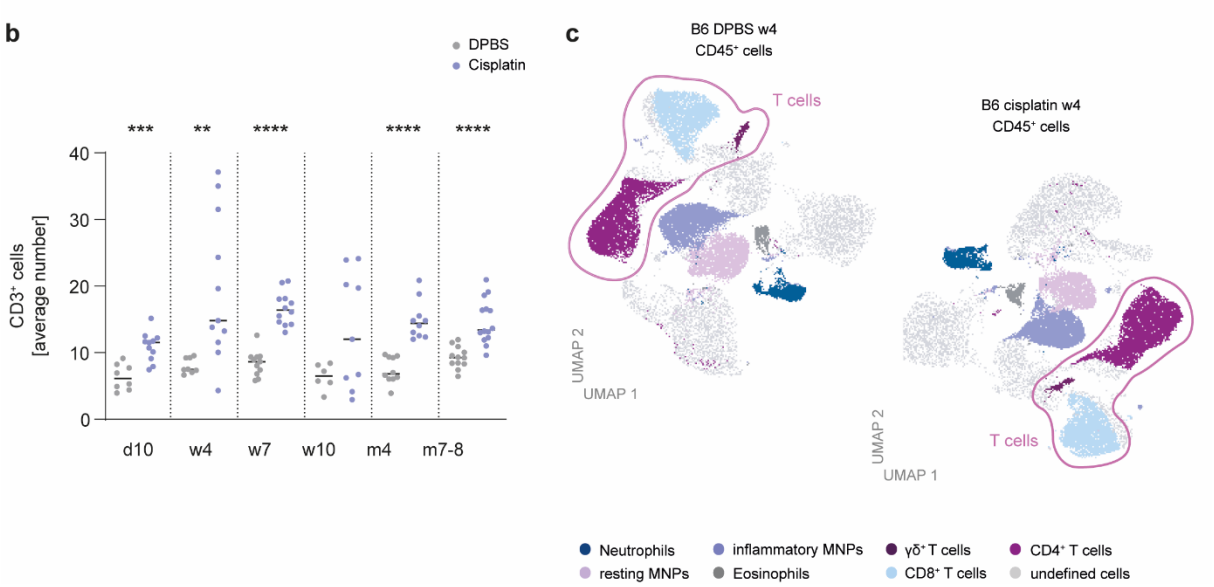

Figure 10: CD3⁺ T cells infiltrate in the resolution phase of AKI.
a Representative photomicrographs of kidney sections from DPBS- and cisplatin-treated B6 mice on day 10, week 4, month 4 and month 7-8 of AKI stained with CD3 staining (dark red), 10-fold magnification, zoomed in section 40-fold magnification. **b** Quantification of CD3 staining in kidney tissue of DPBS- and cisplatin-treated B6 mice (d10 DPBS *n* = 8, cisplatin *n* = 11, w4 DPBS *n* = 8, cisplatin *n* = 11, w7 DPBS *n* = 11, cisplatin *n* = 12, w10 DPBS *n* = 6, cisplatin *n* = 9, m4 DPBS *n* = 10, cisplatin *n* = 10, m7-8 DPBS *n* = 12, cisplatin *n* = 14). **c** UMAP clustering of FACS data from CD45⁺ cells isolated from kidneys of DPBS-treated control (*n* = 5) and cisplatin-treated (*n* = 6) B6 mice at the week 4 time point, T cell populations lined in red. *n* represents number of biologically independent animals, symbols represent individual animals. Bars represent median. Unpaired Student's *t* test was used to compare DBPS-treated mice with cisplatin-treated mice at respective time points.

Since the CD3⁺ T cell staining did not differentiate between different subtypes of CD3⁺ T cells infiltrating the kidney, flow cytometry data from week 4 after cisplatin injection was utilised for a more detailed analysis. UMAP clustering of flow cytometry data from CD45⁺ cells isolated from kidneys of DPBS-treated control and cisplatin-treated B6 mice (Figure 10c) identified seven specific immune cell clusters, including different T cell subtypes. In the cisplatin-treated mice, CD4⁺ T cells accounted for the highest number among all immune cell types and were also the most abundant cell type within the CD3⁺ cell cluster, outnumbering CD8⁺ T cells and γδ⁺ T cells.

In context with the results of the Sirius Red staining for fibrosis (Figure 9), the CD3⁺ T cell staining data indicate that infiltration of CD3⁺ T cells into kidney tissue after cisplatin-induced AKI preceded the onset of kidney fibrosis by weeks. The flow cytometry

data suggested a potential involvement of $CD4^+$ T cells, as a predominant immune cell subset, in the development of CKD after resolution of severe acute kidney damage.

9.5 $CD4^+$ T cell transfer promotes development of fibrosis after AKI

To investigate underlying mechanisms driving progression to CKD following resolution of AKI, a T cell transfer model into *Rag1*$^{-/-}$ mice was established (Figure 11a). *Rag1*$^{-/-}$ mice are homozygous for the *Rag1*^{tm1Mom} mutation and, due to a non-functional *Rag1* gene, lack mature T and B lymphocytes [152]. This lymphocyte deficiency renders transfer of T cells into *Rag1*$^{-/-}$ mice an optimal model to study the specific contributions of T cells in disease development.

In order to examine whether $CD4^+$ T cells are essential for development of fibrosis, one group of *Rag1*$^{-/-}$ mice were injected with 500.000 isolated $CD4^+$ T cells per mouse at day 0. The control group did not receive a T cell transfer. On days 7 and 14 following $CD4^+$ T cell transfer, all *Rag1*$^{-/-}$ mice, including the ones without cell transfer, received cisplatin or DPBS injections. Organ harvest was performed four months after $CD4^+$ T cell transfer. Flow cytometrical analysis of isolated $CD4^+$ T cells before transfer confirmed their purity (Figure 11b), ensuring that any observed effects could be attributed specifically to these cells. Within the population of $CD3^+$ T cells, $CD4^+$ T cells were the only T cell subset detected in *Rag1*$^{-/-}$ mice that had received cell injections, confirming the exclusive presence of the transferred cell population (Figure 11c). Quantification of flow cytometry data demonstrated both the absence of mature T cells in *Rag1*$^{-/-}$ mice and the effective transfer of $CD4^+$ T cells (Figure 11d), validating the mouse model as a suitable system to investigate the role of $CD4^+$ T cells in transition from AKI to CKD.

For characterisation of transferred $CD4^+$ T cells four months post-transfer, T cell surface markers CD62L and CD44 were analysed. CD62L facilitates the recirculation of naïve T cells between blood and lymphatic system [153, 154]. Upon antigen recognition via T cell receptor, T cells differentiate into memory cells, which is accompanied by downregulation of CD62L, and up-regulation of CD44. CD44 serves as an early activation marker and is typically used to distinguish effector T cells from naïve T cells [155]. The vast majority of transferred $CD4^+$ T cells predominantly displayed characteristics

of effector memory T cells (T_{EM}) ($CD62L^{lo}CD44^{hi}$), indicative of prior antigen exposure and capacity for rapid responses upon restimulation [156].

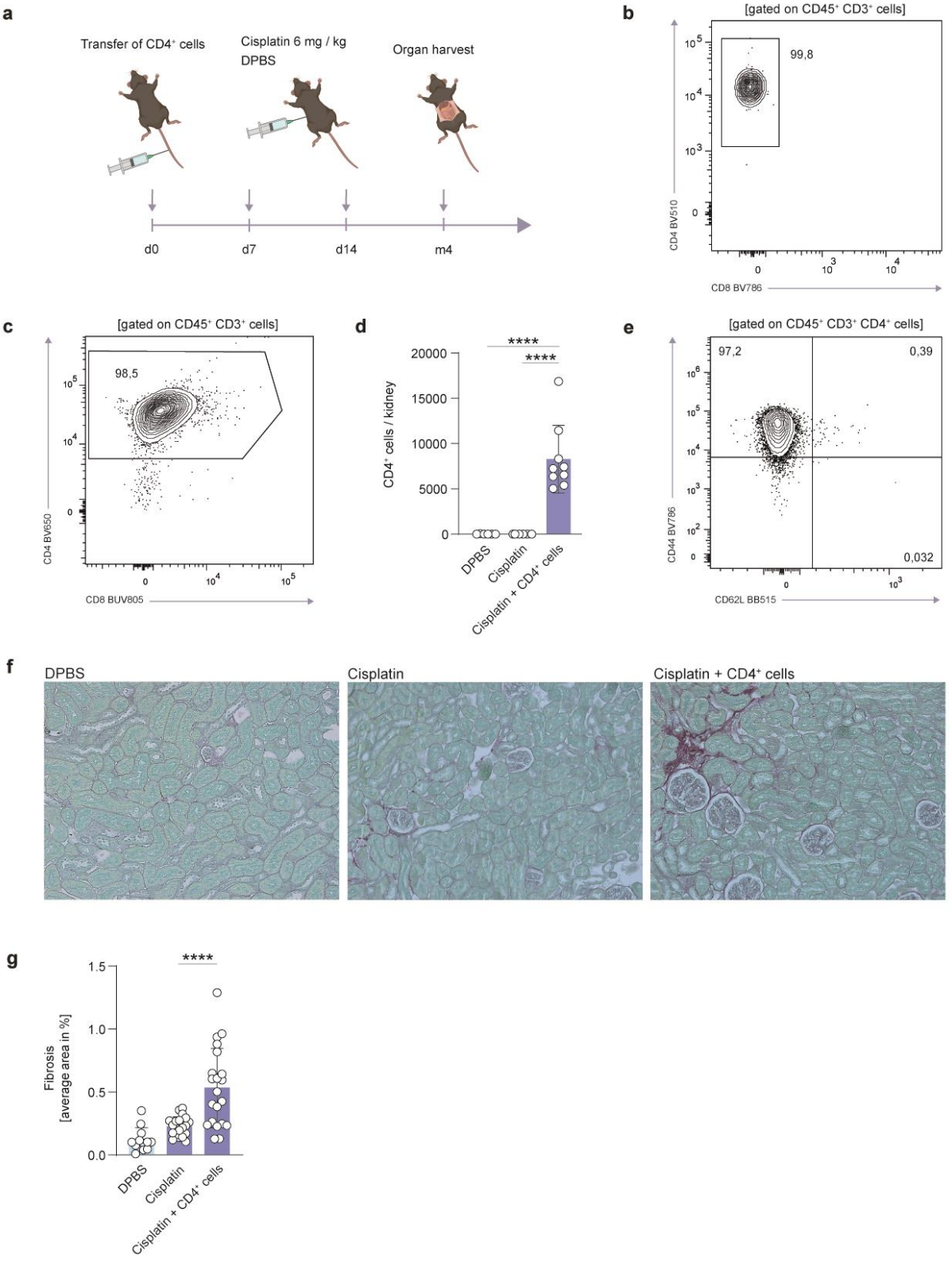

Figure 11: CD4⁺ T cell transfer promotes development of fibrosis after AKI.
a Timeline demonstrating the experimental setup of the *Rag1*$^{-/-}$ mouse model with CD4⁺ T cell transfer at d0 and two cisplatin and DPBS injections at d7 and d14. Organ harvest took place at m4. **b** Representative flow cytometry plot of purity control of transferred CD4⁺ T cells on day 0 of the mouse model. Gating strategy is specified in brackets, numbers indicate percentage of cells in gates. **c** Representative flow cytometry plot of transferred CD4⁺ T cells, isolated from mouse kidneys at the month 4 time point. Gating strategy is specified in brackets, numbers indicate percentage of cells in gates. **d** Quantification of FACS data of CD4⁺ T cell numbers per kidney of different mouse treatment groups (DPBS n = 6, cisplatin n = 10, cisplatin + CD4⁺ T cells n = 9). **e** Representative flow cytometric characterisation of transferred CD4⁺ T cells through activation marker expression, isolated from mouse kidneys at the month 4 time point. Gating strategy is specified in brackets, numbers indicate percentage of cells in gates. **f** Representative photomicrographs of kidney sections from DPBS- and cisplatin-treated *Rag1*$^{-/-}$ mice with or without transfer of CD4⁺ T cells on month 4 of AKI to CKD transition, stained with Sirius Red staining (dark red), 20-fold magnification. **g** Quantification of Sirius Red staining in kidney tissue of DPBS- and cisplatin-treated *Rag1*$^{-/-}$ mice with or without transfer of CD4⁺ T cells in month 4 of AKI to CKD transition through determination of average percental fibrosis area by ImageJ (DPBS n = 12, cisplatin n = 21, cisplatin + CD4⁺ T cells n = 21). n represents number of biologically independent animals, symbols represent individual animals. Bars represent median. Unpaired Student's t test was used to compare different mouse groups at respective time points.

Regarding fibrosis levels after four months, Sirius Red staining of kidney sections (Figure 11f) revealed a significant increase of fibrosis in *Rag1*$^{-/-}$ mice that had received transferred CD4⁺ T cells, compared to cisplatin-injected controls without cell transfer (Figure 11g).

The results of this gain-of-function experiment clearly show that CD4⁺ T cells promote fibrosis development after resolution of AKI.

9.6 Establishment of CD4⁺ T cell depletion

To complement the gain-of-function *Rag1*$^{-/-}$ experiment and further substantiate potential involvement of CD4⁺ T cells in kidney fibrosis development, a loss-of-function approach was established. Antibody-mediated depletion of T cells serves as a valuable strategy to directly evaluate the role of a specific T cell subset *in vivo* and has been widely applied in immunological studies. This intervention technique holds pronounced advantages by allowing for temporal control of cell depletion, which is particularly important for investigating dynamic immune responses and has proven true in several experimental IRI mouse models [157, 158].

Selected depletion of CD4⁺ T cells was achieved in B6 mice via injection of an anti-CD4 monoclonal antibody; the antibody was administered three times prior to the week 4 time point since staining for CD3⁺ T cells indicated a marked influx of CD3⁺ T cells in this period. Consistent with previous experiments, mice received cisplatin injections on days 0 and 7. To validate the suitability of the CD4⁺ T cell depletion strategy and efficacy of the anti-CD4 antibody, a test run of the experiment was conducted in which the organ harvest took place on day 28, immediately following final antibody injection (Figure 12a). Quantification of flow cytometry data (Figure 12b) demonstrated that administration of anti-CD4 antibody led to a significant reduction in the proportion of CD4⁺ T cells among total leukocytes (Figure 12c). Additionally, the absolute number of CD4⁺ T cells per gram kidney tissue was substantially decreased after anti-CD4 antibody administration.

The test run validating the loss-of-function approach confirmed that both the experimental timeline of the animal model and the selected anti-CD4 T cell antibody were suitable to achieve substantial depletion of CD4⁺ T cells at the week 4 time point.

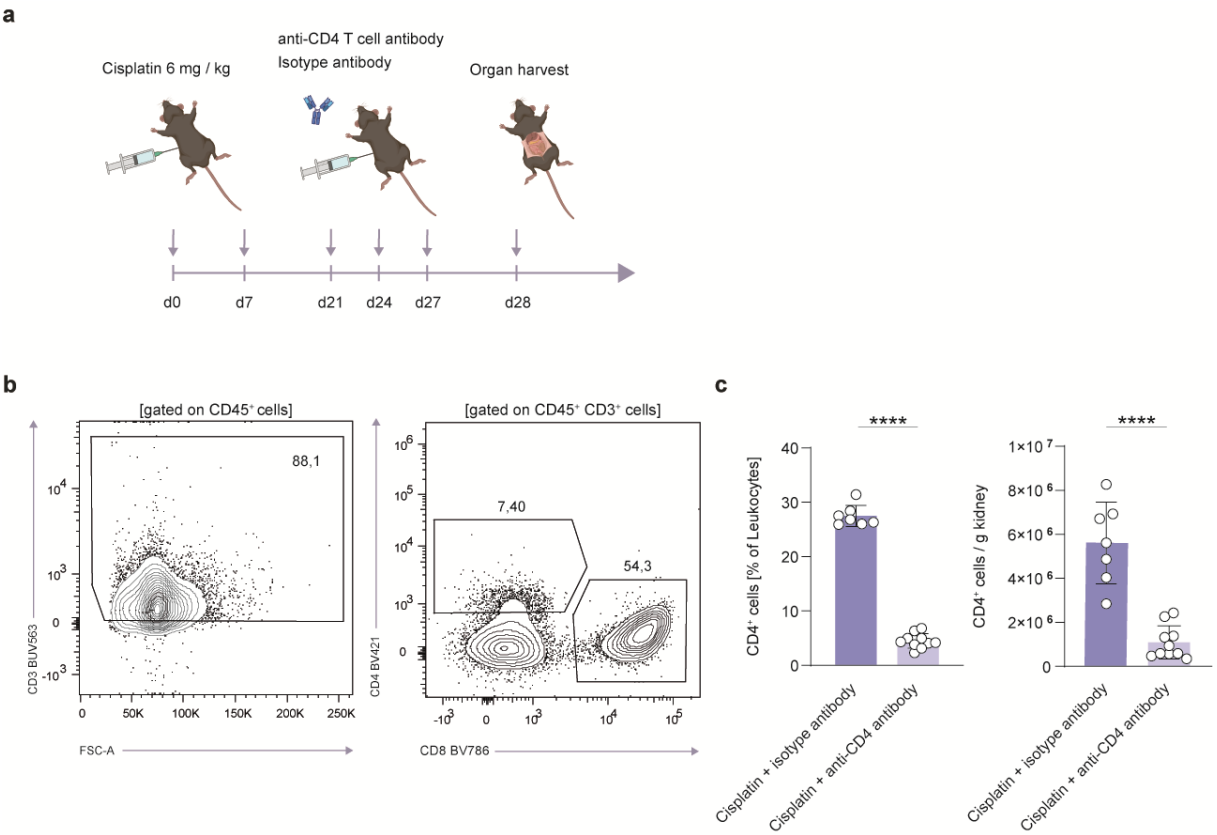

Figure 12: Establishment of CD4⁺ T cell depletion.
a Timeline demonstrating the establishment of the experimental setup of the CD4⁺ T cell antibody depletion mouse model with two cisplatin injections at d0 and d7 and anti-CD4 T cell antibody injections at d21, d24 and d27 in B6 mice. Organ harvest took place at d28. **b** Representative flow cytometry plots of T cells isolated from kidney of a cisplatin- and anti-CD4 T cell antibody-treated B6 mouse at d28. Gating strategy is specified in brackets, numbers indicate percentages of cells in gates. **c** Quantification of FACS data of proportion of CD4⁺ T cells among total leukocytes and absolute CD4⁺ T cell numbers per g kidney of two different treatment groups (cisplatin + isotype antibody *n* = 7, cisplatin + anti-CD4 T cell antibody *n* = 10). *n* represents number of biologically independent animals, symbols represent individual animals. Bars represent median. Unpaired Student's *t* test was used to compare different mouse groups at respective time points.

9.7 Depletion of CD4⁺ T cells reduces development of fibrosis

Following the initial test run of the loss-of-function approach using a CD4⁺ T cell-depleting antibody, the experiment was repeated with a longer time course. Organ harvest was performed after four months in order to assess the long-term impact of CD4⁺ T cell depletion on fibrosis development. The same experimental setup as in the initial test run was employed, with three doses of CD4⁺ T cell-depleting antibody given prior to day 28 (Figure 13a).

Quantification of flow cytometry data (Figure 13b) confirmed that administration of anti-CD4 antibody resulted in a significant and persistent reduction in the proportion of CD4⁺ T cells among total leukocytes even at the late time point three months after T cell depletion (Figure 13c). However, in comparison to the initial test run (Figure 12c), the absolute number of CD4⁺ T cells was decreased to a lesser extent (Figure 13c).
In line with our hypothesis, histological analyses demonstrated a significant fibrosis reduction in T cell-depleted mice compared to isotype-treated mice at the 4 month time point following cisplatin treatment (Figure 13d, e). Notably, mice treated with CD4⁺ T cell-depleting antibody showed fibrosis levels comparable to those observed in age-matched mice without cisplatin treatment.

In summary, the loss-of-function approach corroborated the findings from the gain-of-function experiment, demonstrating that CD4⁺ T cells are essential for development of fibrosis following recovery from acute kidney damage.

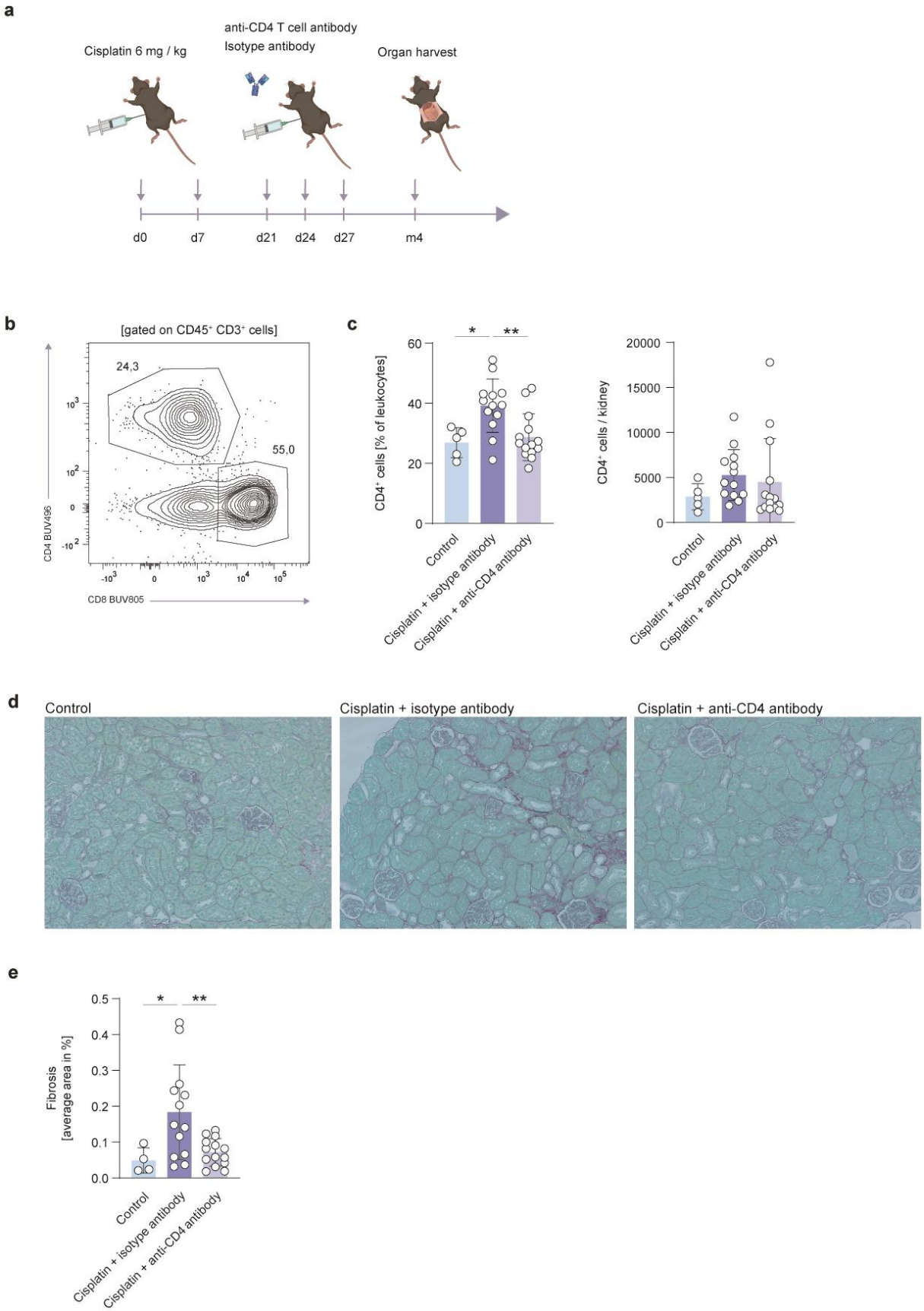
a
Cisplatin 6 mg / kg
anti-CD4 T cell antibody
Isotype antibody
Organ harvest
d0
d7
d21
d24
d27
m4
b
[gated on CD45⁺ CD3⁺ cells]
24,3
55,0
CD4 BUV496
CD8 BUV805
c
CD4⁺ cells [% of leukocytes]
CD4⁺ cells / kidney
Control
Cisplatin + isotype antibody
Cisplatin + anti-CD4 antibody
d
Control
Cisplatin + isotype antibody
Cisplatin + anti-CD4 antibody
e
Fibrosis
[average area in %]
Control
Cisplatin + isotype antibody
Cisplatin + anti-CD4 antibody

Figure 13: Depletion of CD4⁺ T cell reduces development of fibrosis.
a Timeline demonstrating the experimental setup of CD4⁺ T cell antibody depletion mouse model with two cisplatin injections at d0 and d7 and anti-CD4 T cell antibody injections at d21, d24 and d27 in B6 mice. Organ harvest took place at m4. **b** Representative flow cytometry plot of T cells isolated from kidney of a cisplatin- and anti-CD4 T cell antibody-treated B6 mouse at m4. Gating strategy is specified in brackets, numbers indicate percentages of cells in gates. **c** Quantification of FACS data of proportion of CD4⁺ T cells among total leukocytes and absolute CD4⁺ T cell numbers per g kidney of three different treatment groups (control *n* = 5, cisplatin + isotype antibody *n* = 13, cisplatin + anti-CD4 T cell antibody *n* = 14). **d** Representative photomicrographs of kidney sections from control mice, cisplatin- and isotype antibody-treated mice, and cisplatin- and anti-CD4 T cell anti-body-treated B6 mice in month 4 of AKI to CKD transition, stained with Sirius Red staining (dark red), 20-fold magnification. **e** Quantification of Sirius Red staining in kidney tissue of control mice, cisplatin- and isotype antibody-treated mice, and cisplatin- and anti-CD4 T cell antibody-treated B6 mice in month 4 of AKI to CKD transition through determination of average percental fibrosis area by ImageJ (control *n* = 4, cisplatin + isotype antibody *n* = 13, cisplatin + anti-CD4 T cell antibody *n* = 14). *n* represents number of biologically independent animals, symbols represent individual animals. Bars represent median. Unpaired Student's *t* test was used to compare different mouse groups at respective time points.

9.8 Use of single-cell RNA sequencing for investigation of T cell-driven tissue changes in AKI to CKD progression

For in-depth investigation of T cell-driven tissue changes in progression of AKI to CKD, two different single-cell RNA sequencing (scRNA seq) approaches were used. Sequencing was performed 4 and 8 months following cisplatin or DPBS injections. At each time point, both total kidney cells and isolated CD45⁺ leukocytes were subjected to sequencing (Figure 14a).

Sequencing of the entire kidney cell population was performed in order to investigate possible intercellular communication networks, elucidate underlying pathogenic mechanisms, and identify molecular pathways contributing to progression of renal fibrosis. Combination of scRNA sequencing data of a total of 99.546 total kidney cells subjected to unsupervised clustering by the UMAP algorithm enabled identification of 12 distinct clusters based on transcriptional profiles. Clusters were annotated according to cluster-defining genes (Figure 14b).

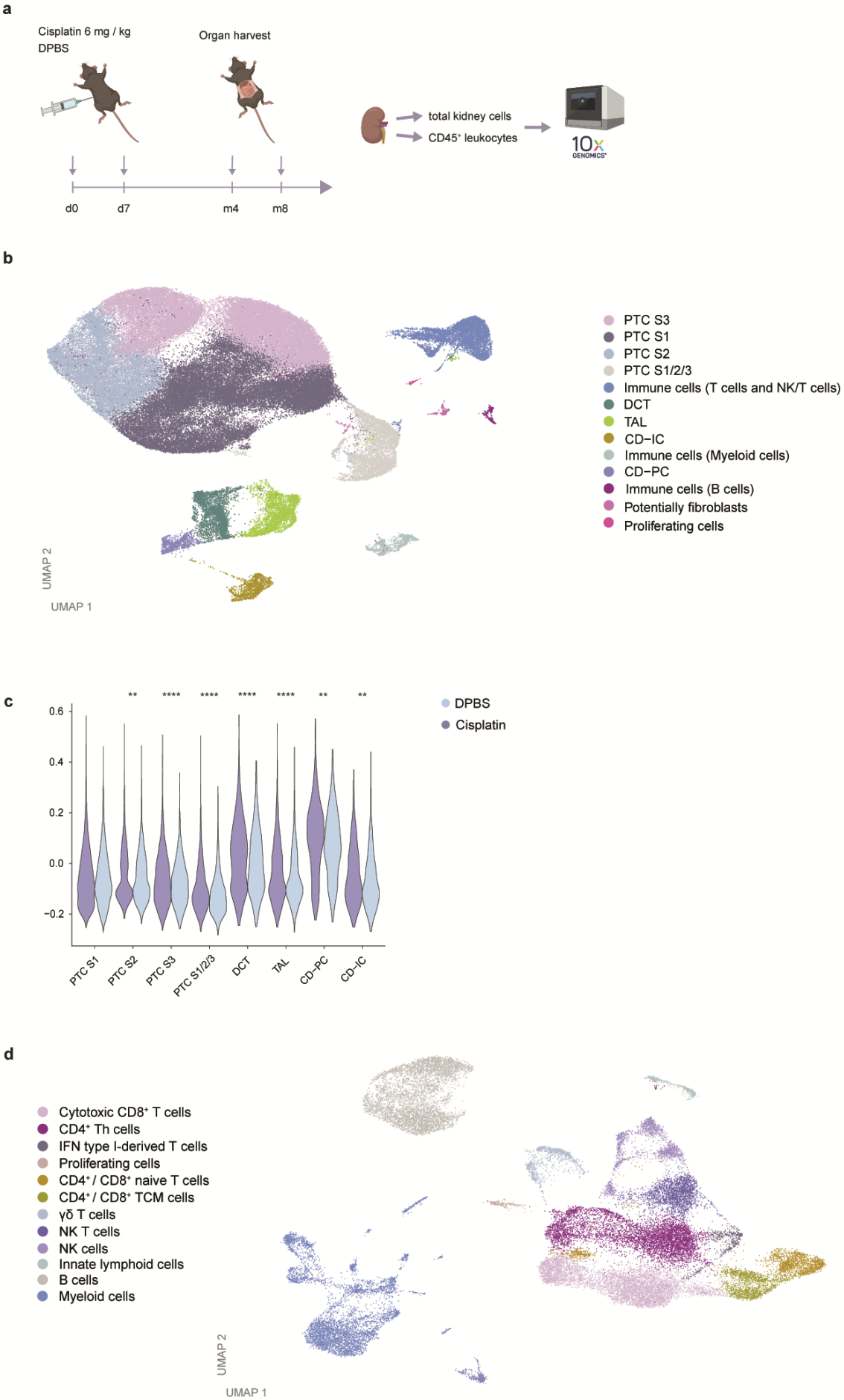
a
Cisplatin 6 mg / kg
DPBS
Organ harvest
d0
d7
m4
m8
total kidney cells
CD45+ leukocytes
10x GENOMICS
b
PTC S3
PTC S1
PTC S2
PTC S1/2/3
Immune cells (T cells and NK/T cells)
DCT
TAL
CD−IC
Immune cells (Myeloid cells)
CD−PC
Immune cells (B cells)
Potentially fibroblasts
Proliferating cells
UMAP 2
UMAP 1
c
DPBS
Cisplatin
0.6
0.4
0.2
0.0
−0.2
PTC S1
PTC S2
PTC S3
PTC S1/2/3
DCT
TAL
CD−PC
CD−IC
d
Cytotoxic CD8+ T cells
CD4+ Th cells
IFN type I-derived T cells
Proliferating cells
CD4+ / CD8+ naive T cells
CD4+ / CD8+ TCM cells
γδ T cells
NK T cells
NK cells
Innate lymphoid cells
B cells
Myeloid cells
UMAP 2
UMAP 1

Figure 14: Use of single-cell RNA sequencing for investigation of T cell-driven tissue changes in AKI to CKD progression.
a Timeline demonstrating the experimental setup for scRNA sequencing of total kidney cells and $CD45^+$ leukocytes. B6 mice were injected two times with cisplatin or DPBS at d0 and d7, organ harvests took place at m4 and m8. **b** Unsupervised UMAP clustering (resolution 0.5) of scRNAseq data from 99.546 total kidney cells isolated from two times DPBS- and cisplatin-treated B6 mouse kidneys at month 4 and month 8 of AKI to CKD progression. 12 clusters were identified and annotated according to cluster defining genes and expression of selected marker genes (m4 DPBS $n = 3$, cisplatin $n = 4$, m8 DPBS $n = 4$, cisplatin $n = 6$). **c** Violin plot showing expression of stress signalling score by different kidney cell types in cisplatin-treated mice as compared to naïve controls. Stress signalling score was calculated based on genes *Havcr1*, *Lcn2*, *Wnt4*, *Hmox1*, *Casp3*, *Trp53*, *Cdkn1a*, *Slc25a21*, *Tead1*, *Cldn16*, *Apobec1*, *Gsta3*, *Ambp*, *Clu*. d Unsupervised UMAP clustering (resolution 0.7) of scRNAseq data from 34.490 $CD45^+$ leukocytes isolated from two times DPBS- and cisplatin-treated B6 mouse kidneys at month 4 and month 8 of AKI to CKD progression. 12 clusters were identified and annotated according to cluster defining genes and expression of selected marker genes (m4 DPBS $n = 3$, cisplatin $n = 4$, m8 DPBS $n = 4$, cisplatin $n = 6$) (TCM = central memory T cells). PTC = proximal tubule cells, DCT = distal convoluted tubule cells, CD PC = collecting duct principal cells, TAL = thick ascending limb cells, CD IC = collecting duct intercalated cells. *n* represents number of biologically independent animals.

For investigation of the long-term impact of two low-dose cisplatin administrations on renal tissue, various kidney cell types were analysed 4 months after the initial nephrotoxic injury for their expression of stress signalling genes. Violin plots comparing DPBS-treated control samples and cisplatin-treated samples (figure 14c) revealed that, across all examined cell types, except for proximal tubular cells segment 1, cisplatin-treated kidney cells exhibited a persistently elevated expression of genes associated with stress signalling pathways relative to controls.

To provide deeper insights into the complexity of the immune landscape in transition of cisplatin-induced AKI to CKD progression, high-resolution transcriptomic profiling of $CD45^+$ kidney leukocytes was additionally performed, allowing for identification of different immune cell subsets, their activation statuses and potential interactions [159].
A total of 34.490 $CD45^+$ leukocytes isolated from DPBS- and cisplatin-treated mice at both time points were combined and subjected to unsupervised clustering by the UMAP algorithm (Figure 14d). This approach identified 12 distinct clusters of $CD45^+$ immune cells characterised by unique mRNA expression profiles, including three $CD4^+$ T cell subclusters. Clusters were annotated according to cluster-defining genes. Analysis of the $CD45^+$ leukocyte dataset confirmed sufficient cell numbers and sequencing depth to support further in-depth investigations.

Based on prior experiments suggesting a role for $CD4^+$ T cells in mediating fibrotic processes associated with CKD progression, a more detailed analysis of their gene expression profiles and potential involvement in exacerbating renal injury was conducted. A total of 7.947 $CD4^+$ T cells extracted from the $CD45^+$ leukocyte UMAP were further subclustered into eight distinct subsets based on their unique mRNA expression profiles. These subclusters were annotated according to cluster-defining genes (Figure 15a, b). Among the $CD4^+$ T cell subclusters, the most abundant subsets included distinct populations of TNF^+ and $IFN\gamma^+$ tissue-resident memory T cells (T_{RM}), alongside effector memory T cells (T_{EM}), and naïve T cells, indicating the presence of both terminally differentiated effector and naïve T cell subsets.

Notably, the composition of $CD4^+$ T cell subsets within the kidney exhibited significant temporal changes between 4 and 8 months post-cisplatin administration (Figure 15c). At four months following initial cisplatin injection, T_{regs} constituted the predominant $CD4^+$ T cell population, followed by type 1 regulatory (Tr1)-like cells and effector memory T cells, compared to the DPBS control group. TNF^+ tissue-resident memory T cells represented the smallest fraction of renal $CD4^+$ T cells at this time point. Conversely, at eight months following initial cisplatin injection, TNF^+ T_{RM} cells emerged as the dominant subset, with $IFN\gamma^+$ T_{RM} cells and T_{EM} cells representing the second and third largest subsets, respectively, in comparison to the control group. Tr1-like T cells made up the smallest proportion of $CD4^+$ T cells. These findings indicate a distinct inversion in the relative abundances of $CD4^+$ T cell subsets over the course of disease progression.

In summary, single-cell RNAseq analyses of $CD45^+$ leukocytes with a particular focus on $CD4^+$ T cells revealed dynamic shifts in the composition of renal $CD4^+$ T cell subsets during progression of CKD. Four months following the initial injury, regulatory and Tr1-like cells dominated in an immunoregulatory environment, whereas eight months after cisplatin administration the amount of pro-inflammatory TNF^+ and $IFN\gamma^+$ tissue-resident memory T cells increased with progression of fibrosis.

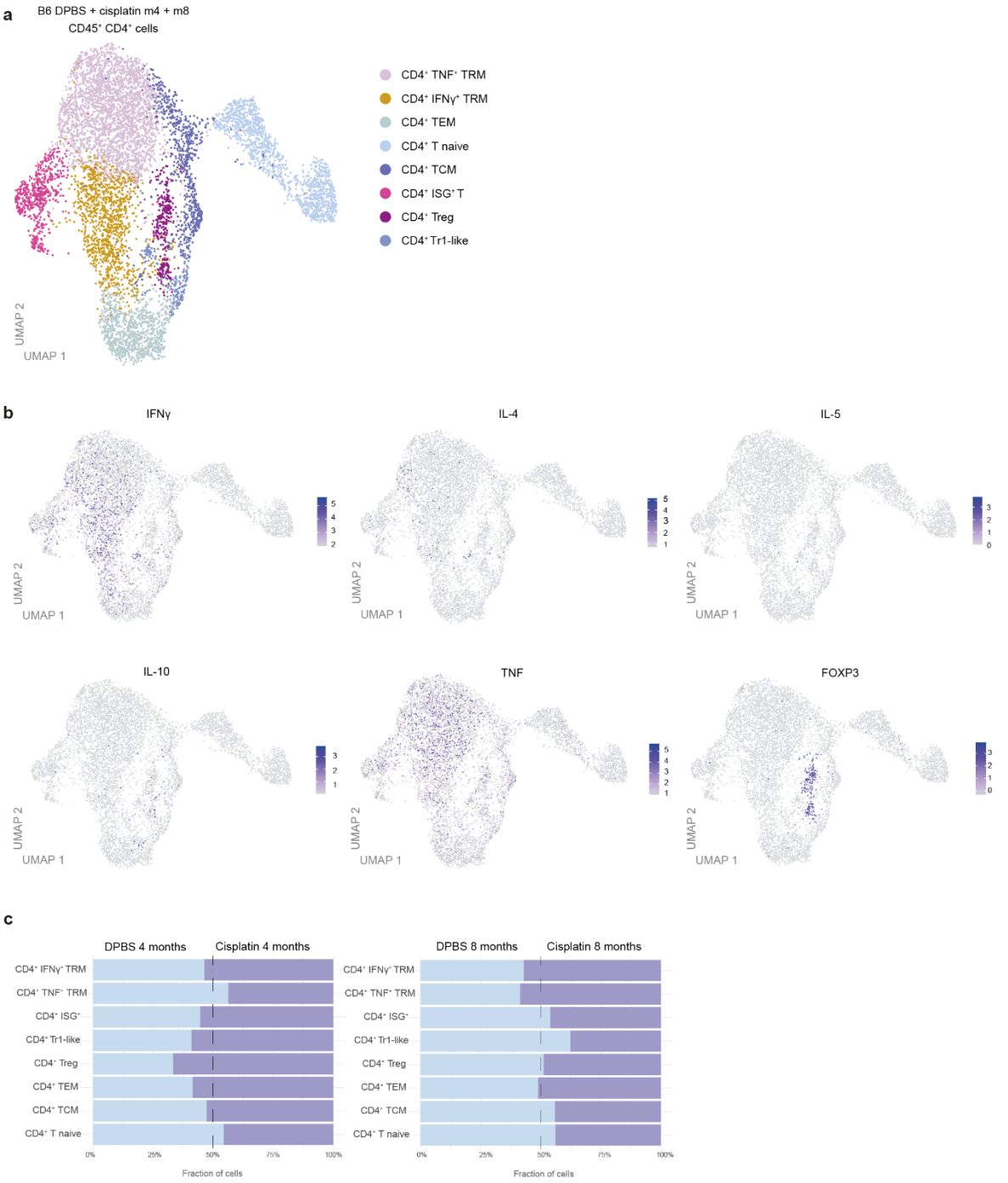

Figure 15: Analysis of single-cell RNA sequencing data from CD4⁺ T cells provides insights into diverse subpopulations.

a Unsupervised UMAP clustering (resolution 0.5) of 7.947 CD4⁺ T cells extracted from scRNAseq data from 34.490 CD45⁺ leukocytes isolated from two times DPBS- and cisplatin-treated B6 mouse kidneys at month 4 and month 8 of AKI to CKD progression. 8 clusters were identified and annotated according to cluster defining genes and expression of selected marker genes (TRM = tissue-resident memory T cells, TEM = effector memory T cells, TCM = central memory T cells, ISG = Interferon-Stimulated Genes, Tr1-like = Type 1 regulatory (Tr1)-like T cells). **b** UMAP plots showing gene expression. Cells exhibiting high expression of respective genes were marked in purple and plotted on the original UMAP plot. **c** Analysis of contribution of different T cell subsets at time points 4 and 8 months in cisplatin- and DPBS-treated mice, shown is the percental fraction of respective subtypes.

Since fibroblasts constitute a key cell type involved in fibrosis progression, they were analysed in detail to enable investigation of potential cell-cell interactions with kidney tissue cells. Expression of the canonical fibroblast markers collagen (genes C*ol1α1* and *Col3α1)* [160-162], vimentin (gene *Vim*) [163, 164], α-smooth muscle actin (α-SMA) (gene *Acta2*) [46], transgelin (gene *Tagln*) [165] and endothelin-1 (gene *Edn1*) [166] in the total kidney cells dataset allowed for identification of a small population of fibroblasts (Figure 16).

However, despite successful identification, the total number of fibroblasts captured was insufficient for robust downstream analyses, such as cell-cell interaction analysis or pathway enrichment studies. The limited cell count reduced the validity of conclusions regarding fibroblast heterogeneity and functional states at different time points, as well as statistical power of analyses.

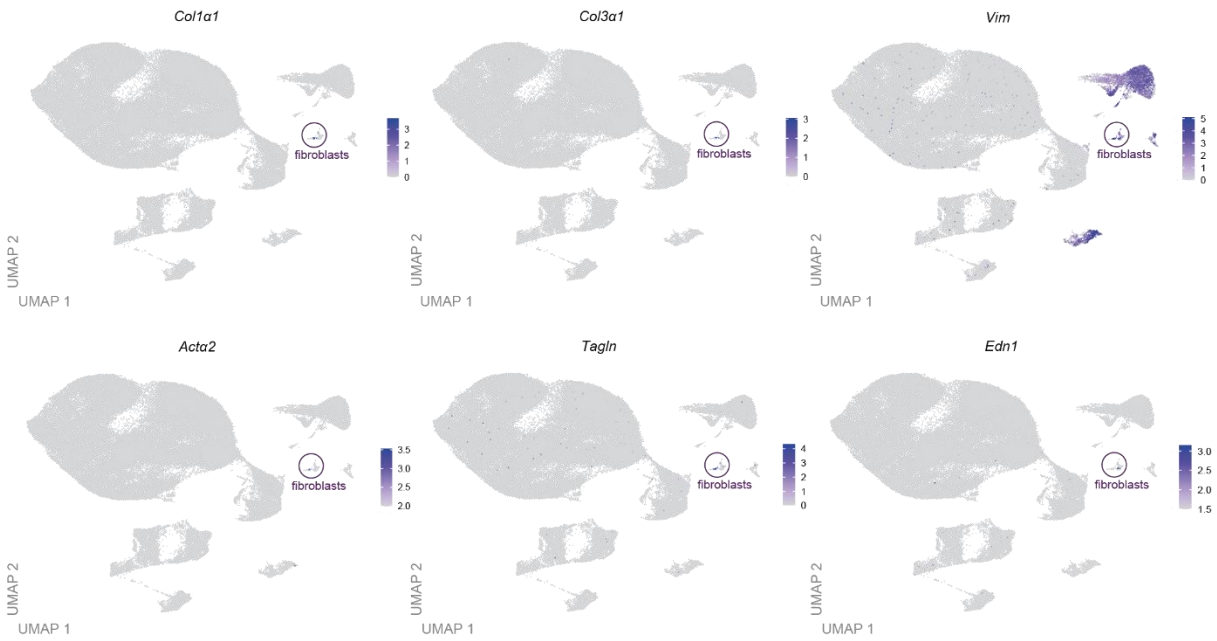

Figure 16: Single-cell RNA sequencing of total kidney cells identified a distinct fibroblast cluster characterised by specific marker expression.

UMAP plots showing expression of fibroblast-defining genes. Cells exhibiting high expression of respective genes were marked in purple and plotted on the original UMAP plot of 99.546 total kidney cells.

In summary, scRNA sequencing successfully identified a stress response in tubular cells and a shift of the composition of kidney-infiltrating $CD4^+$ T cell subsets. Although a distinct fibroblast cluster as a presumed key player in development of fibrosis could also be identified in the scRNA seq data set, further downstream analyses of immune cell fibroblast interactions would require optimisation of the cell isolation protocol to enrich for fibroblasts.

10 Discussion

AKI is characterised by a rapid deterioration of kidney function, primarily manifesting in impaired glomerular filtration [1]. In high-income countries, AKI constitutes a major challenge for the health care system, impacting over 13 million individuals annually.
In recent years evidence emerged indicating that AKI frequently leads to long-term structural damage within the kidney parenchyma, resulting in an increased risk for CKD development, a leading cause of global mortality [2]. Despite current research efforts, reliable biomarkers predicting AKI to CKD transition, as well as effective therapeutic interventions preventing or attenuating this progression are still lacking [44]. This thesis aimed at elucidating the mechanisms that are responsible for fibrosis development after resolution of cisplatin-induced acute kidney damage.

Despite a vast body of literature on cisplatin-induced AKI, only a limited number of published studies have investigated the long-term consequences of cisplatin-induced AKI. Hence, the mechanisms underlying the transition of cisplatin-induced AKI to CKD remain poorly understood.
The standard mouse model investigating cisplatin-induced nephrotoxicity uses a single high dose of cisplatin. Typical doses range from 20 mg/kg BW to extremely high, lethal doses of up to 40 mg/kg BW [167]. The use of high cisplatin concentrations limits the respective experiments to a timespan of three to four days due to mouse mortality. Furthermore, this dosage does not reflect standard treatment regimens used in the clinic, but rather cisplatin intoxication, representing one of the major drawbacks of most published studies on cisplatin nephrotoxicity [167-169]. In addition, in the majority of published cisplatin mouse models, a high mortality persists despite distinct improvements of clinical parameters, thereby destructing the evaluation of potential therapeutic interventions [167]. These limitations were overcome by establishment of the AKI to CKD transition low-dose cisplatin mouse model lacking substantial mortality employed in this thesis.

To date, most of the mouse models used for long-term studies of cisplatin effects still terminate after four to six weeks [146, 167, 170, 171], thereby limiting their suitability for the assessment of long-term consequences following cisplatin-induced AKI. Furthermore, in current models, CKD is typically induced by repeated administration of low doses of

cisplatin over several weeks, modelling chronic nephrotoxicity rather than AKI to CKD transition [172].

To this day, only one study addresses the long-term consequences after apparent complete resolution of AKI in an one-incident ischemia-reperfusion AKI mouse model [173]. In this study, CKD development in response to a single IRI event was evaluated across 10 time points, with the final assessment conducted 12 months after the AKI event. As expected, the initial IRI resulted in markedly elevated levels of serum creatinine, peaking at day two, returning to baseline after two weeks and staying consistently low until the 12 months point, indicating that renal function was restored within two weeks. Histological analyses of kidney sections at early time points (1 day, 2 weeks) following IRI revealed only mild structural tissue damage. However, starting at around 6 months post-IRI, histological signs of tubular injury and interstitial fibrosis became evident and continued to progress over time. By 12 months, the kidneys exhibited severe structural changes, including pronounced scarring indicative of end-stage renal disease. These findings suggest that a single severe initial hit is sufficient to drive the progression from AKI to end-stage renal disease and that clinical parameters, such as serum creatinine, do not sufficiently reflect the underlying structural state of the kidney [173].

In the present study, a novel mouse model of nephrotoxic AKI induced by two low-dose cisplatin injections without substantial mortality was used. This model made it possible to analyse long-term consequences of resolving AKI for up to 8 months. In line with the previous study from Liu *et al*. using an IRI-induced AKI mouse model, it was found that clinical markers, including KIM-1 and BUN, alongside caspase-3 immunostaining, confirmed the validity of the sublethal low-dose cisplatin mouse model in inducing severe AKI. BUN values can be substantially affected by factors unrelated to kidney function, including dietary intake and other physiological variables such as hydration status, and is therefore seen as one of the less sensitive markers of renal failure [174].

Notably, excretory kidney function recovered by week 4, as evidenced by normalisation of clinical parameters, indicating clinical resolution of AKI within this timeframe. This apparent resolution of AKI within a timeframe ranging from a few days to up to two weeks, has been reported in several studies [173, 175-177]. Despite apparent functional recovery by week 4, cisplatin-treated mice developed progressive renal fibrosis between weeks 7 and 10, a hallmark feature of CKD. Therefore, it was successfully shown that AKI to CKD transition can also be observed after nephrotoxic AKI, as it was

demonstrated for IRI-induced AKI [173]. This progression highlights the existence of underlying molecular mechanisms driving ongoing renal damage after AKI which are not detectable by measurement of standard parameters used in the clinic and are therefore often missed, rendering the timely onset of potential preventive therapies for CKD development difficult.

In recent years, numerous studies have utilised mouse models to investigate the transition from AKI to CKD. While IRI remains the predominant method to induce AKI in these models, the contribution of drug-induced nephrotoxicity has received increasing attention [178], despite the fact that suitability of current AKI to CKD mouse models using cisplatin for induction of AKI was limited, as detailed above. However, prior research exploring cisplatin-induced AKI to CKD progression has identified various mechanisms [179].

Different apoptotic pathways contribute to the development of AKI and the ensuing progression towards CKD, including the extrinsic pathway activated via death receptors such as TNF and Fas receptors [37], the intrinsic mitochondrial pathway inducing apoptosis through mitochondrial dysfunction [180], and the endoplasmic reticulum stress pathway [37]. Additionally, reactive oxygen species (ROS) and oxidative stress have been shown to induce apoptotic cell death in renal tubular cells [181]. Enhanced production of the pro-inflammatory cytokine TNF-α not only exerts direct nephrotoxic effects on renal epithelial cells but also regulates a cytokine network that facilitates substantial leukocyte infiltration [182]. Moreover, activation of the p53 tumor suppressor contributes to cell cycle arrest and apoptosis [183], further promoting kidney injury.

With regard to kidney-infiltrating immune cells after AKI, most studies have focused on the early phase after injury, within the first few days following IRI or cisplatin administration. In terms of immune cell involvement during the progression from AKI to CKD, research has predominantly concentrated on the role of monocyte-derived macrophages [146, 184] as well as the involvement of $CD4^+$ and $CD8^+$ T cells [115, 158].

In the present study, immunohistochemical staining and flow cytometry analyses revealed a significant infiltration of $CD3^+$ T cells, particularly $CD4^+$ T cells, into renal tissue weeks prior to the onset of kidney fibrosis. At the time point of $CD3^+$ immune cell infiltration, AKI was resolved, but fibrosis not yet evident, which opens a therapeutic window of opportunity for preventing AKI to CKD transition. While numerous studies

have shown the role of T cells in the acute phase of AKI [151, 185], their involvement in the long-term phase following AKI remains understudied and insufficiently charac-terised. Few studies demonstrate infiltration of $CD3^+$ immune cells during AKI to CKD transition in mice, all of which use an IRI mouse model and examine shorter experimental timelines compared to this thesis. Do Valle Duraes *et al*. [115] showed that following IRI, $CD3^+$ T cells infiltrate damaged kidney tissue from day 14 onwards and express profibrotic gene signatures, providing a first hint that T cells may drive long-term fibrotic tissue changes after AKI. Burne-Taney *et al*. [186] demonstrated $CD4^+$ T cell-infiltration into the kidney 6 weeks post-ischemia, whereas Ascon *et al*. [158] found that both $CD4^+$ and $CD8^+$ T cells infiltrated the injured kidney 6 weeks after IRI. Taken together, these studies support the hypothesis that accumulation of T cells in the kidney tissue after AKI initiates a localised, chronic subclinical inflammatory response that ultimately drives long-term development of CKD. In the present study, this hypothesis was substantiated by showing that $CD4^+$ T cells represent the predominant subset infiltrating the kidney after cisplatin-induced AKI. Importantly, by employing gain- and loss-of-function experiments, first functional evidence was provided that $CD4^+$ T cells are indeed critical drivers of fibrosis development after resolving AKI.
After four months, transferred $CD4^+$ T cells showed differential expression of activation and effector-memory markers CD62L and CD44 indicative of successful adaptation and functional integration of the transferred $CD4^+$ T cells within the immune system of employed *Rag1*$^{-/-}$ mice. This phenotype of effector memory T cells was also reported by Ascon *et al*. [158] 11 weeks after IRI-induced AKI.

In recent years, $CD4^+$ tissue-resident memory T cells (T_{RM} cells) have attracted a lot of attention for playing a pivotal role in shaping the local immune landscape in peripheral organs [187, 188], including the kidney [189-191]. Following AKI, the renal microenvironment undergoes significant remodelling which may lead to establishment of a specialised T_{RM} population that gets imprinted by tissue signals. Under steady-state conditions, a baseline population of resident $CD4^+$ T_{RM} cells is present in the kidney. In response to cisplatin administration, additional $CD4^+$ T cells are recruited from the circulation into the kidney, some of these infiltrating cells might undergo phenotypic and transcriptional changes to adopt a tissue-resident memory phenotype. This AKI-induced $CD4^+$ T_{RM} cell population could contribute to the formation of a specialised inflammatory niche by producing pro-inflammatory cytokines and maintaining activation of the immune

system over several months, worsening tissue injury and exacerbating fibrotic remodelling. By secreting profibrotic cytokines, CD4⁺ T_{RM} cells could directly influence the activation and differentiation of resident fibroblasts into myofibroblasts, the primary effectors of extracellular matrix deposition. This crosstalk between T_{RM} cells and (myo)fibroblasts, combined with persistent inflammation, may drive maladaptive repair processes that occur even after the apparent recovery of initially damaged PTECs, ultimately accelerating the progression towards CKD. This working model of CD4⁺ T_{RM} cell-driven AKI to CKD transition is summarised in figure 17.

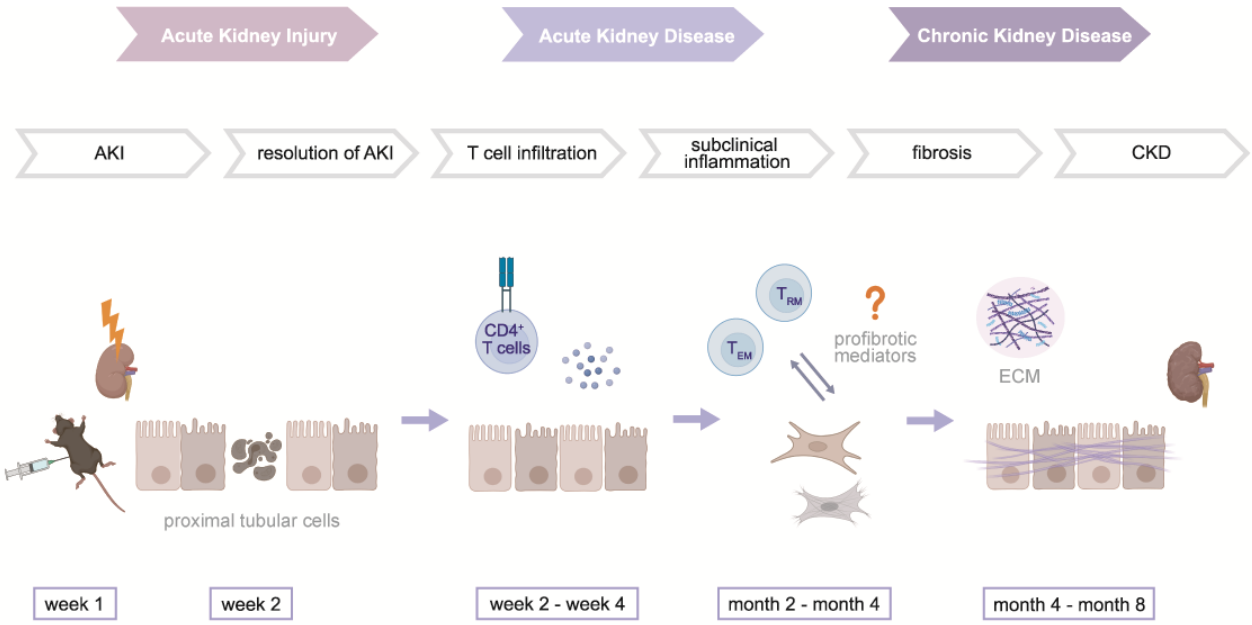

Figure 17: Working model of CD4⁺ T_{RM} cell-driven AKI to CKD transition.
Upon administration of low cisplatin doses in mice, proximal tubular epithelial cells undergo severe injury, resulting in AKI. Although this nephrotoxic damage resolves within two weeks, it is subsequently followed by infiltration of CD4⁺ T cells into the renal interstitium. T_{RM} or T_{EM} cells possibly engage with profibrotic mediators, including (myo)fibroblasts, thereby promoting extracellular matrix (ECM) deposition. This interaction drives renal fibrosis, scarring, and progressive chronic kidney damage, ultimately resulting in renal failure.

To provide evidence for our working model, single-cell profiling of both total kidney cells and isolated CD45$^+$ leukocytes was performed to enable in-depth characterisation of T cell subsets and T cell-driven changes in parenchymal kidney cells during progression of AKI to CKD.

Single-cell RNA sequencing of CD45$^+$ leukocytes allowed for comprehensive analysis of CD4$^+$ T cells which provided insights into subtype distribution of CD4$^+$ T cells. Interestingly, four months after cisplatin-induced injury, regulatory and Tr1-like cells dominate in an immunoregulatory environment, possibly restoring tissue integrity and immune homeostasis, dampening excessive inflammation and participating in the regeneration of injured kidney tissue. It is known that T_{regs} migrate to the kidney during the early phase of cisplatin-induced nephrotoxicity [112], but research regarding the role of T_{regs} at later time points during progression of AKI to CKD, in particular in cisplatin-induced injury, is still scarce [192]. Notably, recent scRNA-seq data from a murine IRI model revealed that T_{regs} exhibit distinct transcriptional profiles depending on the microenvironmental context. Specifically, T_{regs} isolated from kidneys undergoing regeneration displayed upregulation of genes associated with angiogenesis and tissue remodelling and repair, whilst T_{regs} from fibrotic kidneys demonstrated elevated expression of pro-inflammatory and apoptosis-related genes [115]. These results indicate a potential, context-dependent functional plasticity of T_{regs} during the recovery phase following acute kidney damage. The observation that T_{regs} remain dominant in the kidney even four months after cisplatin-induced AKI without preventing the progression of renal fibrosis underscores the need to further investigate the potentially divergent roles of T_{regs} during the later stages of transition of AKI to CKD.

Eight months following cisplatin administration, a distinct expansion of pro-inflammatory TNF$^+$ and IFNγ$^+$ tissue-resident memory T cells was observed, coinciding with the progression of renal fibrosis. This finding confirms the hypothesis that induction of a cisplatin-induced profibrotic CD4$^+$ T_{RM} cell population might contribute to AKI to CKD progression after initial recovery of acute kidney damage.

Although sequencing of the entire kidney cell population was successful and enabled detailed identification of a variety of renal cell types, the number of fibroblasts captured was insufficient for further downstream analyses. The limited representation of fibroblasts within this single-cell sequencing dataset is not reflecting the expected relative

abundance of fibroblasts in kidney tissue samples but is most likely due to technical limitations in the cell isolation procedures used in these experiments. For cell isolation in this thesis, enzymatic digestion of kidney cells was performed with the Multi Tissue Dissociation Kit 2 by Miltenyi for 30 min at 37 °C (see 8.7.1). Several published protocols focus on the isolation of (myo)fibroblasts from kidney tissue by using different enzymes such as collagenase I or II and longer incubation times of up to 4 hours [193-195]. Collagenase I is often preferred for isolating fibroblasts because of its strong collagenolytic activity which helps release fibroblasts embedded in dense ECM. Conversely, collagenase II exhibits higher amidolytic activity, potentially influencing its efficacy in tissue dissociation [196, 197].

Since interactions between fibroblasts and T cells presumably play a central role in fibrosis progression, cell isolation protocols will have to be optimised in future studies to enrich for fibroblasts which would enable detailed cell-cell interaction analyses with other renal and immunological cell types. These analyses will facilitate identification of relevant interaction pathways between immune cells and (myo)fibroblasts to bring the understanding of cellular crosstalk initiating formation of fibrotic tissue in AKI to CKD transition forward.

Immune modulation as a potential therapeutic strategy for AKI to CKD progression

The development of therapeutic strategies specifically targeting the progression from AKI to CKD is limited by incomplete understanding of the molecular pathways underlying subclinical inflammation and fibrosis development persisting after AKI resolution. As a result, there is currently no effective therapy or intervention available that can reliably prevent, halt or reverse AKI to CKD transition [3].

Epigenetic mechanisms are increasingly recognised as major factors in the pathophysiological processes contributing to progression of AKI to CKD. These mechanisms such as DNA methylation, histone modifications, and alterations in micro RNA (miRNA) expression are decisive for the regulation of gene expression and down-stream cellular responses. Given their dynamic and reversible nature, epigenetic modifications represent attractive potential therapeutic targets, particularly for improving inflammation and renal fibrosis, two key drivers of CKD progression [198, 199].

Growth factors have also gained attention as potential therapeutic targets due to their pivotal functions in renal regeneration and repair mechanisms. Epidermal growth factor

(EGF), insulin-like growth factor 1 (IGF-1), transforming growth factor-β1 (TGF-β1), and vascular endothelial growth factor (VEGF) are significantly altered in cisplatin-induced AKI models. Adjusting the activity of these growth factors may enhance recovery and reduce progression to CKD. Moreover, the therapeutic potential of growth factors can be combined with the potential of mesenchymal stem cells (MSCs), as growth-factor modified stem cells show a higher therapeutic efficacy than untreated controls. For example, VEGF165-modified MSCs enhanced renal recovery in cisplatin-induced AKI by reducing apoptosis, improving microcirculation, and promoting proliferation [200, 201]. The growth factor Wnt/β-catenin plays a critical role in renal development and is reactivated following injury. It has been shown that activation of the Wnt/β-catenin pathway confers short-term protection to tubular epithelial cells in various experimental mouse models of AKI by modulation of apoptosis and survival pathways. In contrast to this, in CKD models Wnt/β-catenin signalling seemed to promote renal fibrosis [202].
Studies specifically addressing the long-term consequences of AKI in the kidney tissue on a molecular level are still lacking, emphasising the need for further research into the pathways that are involved in the subsequent transition to CKD after AKI.

The findings presented in this thesis provide new insights into the immunological mechanisms driving the transition from AKI to CKD. Specifically, a marked infiltration of $CD4^+$ T cells into the kidney between week 2 and week 4 post-injury was demonstrated, identifying a potential therapeutic window for targeted interventions. One possible strategy could be to selectively deplete renal $CD4^+$ T cells exhibiting a T_{RM} phenotype, characterised by the expression profile $CD69^+ CD62L^{lo} CD44^{hi}$. These cells may play a critical role in sustaining local inflammation and promoting fibrotic remodelling, and their targeted removal could help mitigate long-term renal damage and delay or abolish CKD progression. Several approaches could be employed to selectively deplete $CD4^+$ T_{RM} cells in the kidney. Antibody-mediated depletion using monoclonal antibodies or nanobodies represents a direct strategy [203]. Alternatively, agents that interfere with T_{RM} survival signals, such as inhibitors of IL-7 signalling, could indirectly diminish T_{RM} cell numbers [204]. Emerging techniques, including tissue-specific delivery of cytotoxic agents via nanoparticles and the use of cell-mediated drug delivery systems (CDDSs) for targeted delivery of immune stimulants, cytokines, and antibodies known from cancer treatment [205-207] increase specificity and safety [208] and

could possibly be adapted for T_{RM} cell depletion. Furthermore gene-editing tools, like CRISPR/Cas9 [209], and personalised immunotherapy, such as chimeric antigen receptor (CAR) T cell therapy [210], offer the potential for localised and selective targeting of different cell types, including pathogenic T_{RM} cells. As a result, the impact on protective immune cells in other compartments and non-target tissues is minimised, reducing the risk of therapy-limiting side effects.

While targeting $CD4^+$ T_{RM} cells in the kidney may offer therapeutic benefits, this approach also carries potential risks. $CD4^+$ T_{RM} cells contribute to tissue immune surveillance and play an important role in maintaining local immune homeostasis. Their depletion could impair host defense mechanisms, increasing susceptibility to opportunistic infections or reactivation of latent pathogens within the kidney. Additionally, systemic depletion strategies may affect beneficial $CD4^+$ T cell subsets in other tissues, potentially leading to unintended immunosuppression, altered mucosal immunity, or impaired vaccine responses. Therefore, any therapeutic strategy aimed at eliminating T_{RM} cells must be carefully designed to minimise off-target effects and preserve protective immunity.

11 List of abbreviations

°C	degree Celsius
α-SMA	α-smooth muscle actin
ACTA2	Actin Alpha 2
ADP	Adenosine diphosphate
AF	Alexa Flour
AKD	Acute kidney disease
AKI	Acute kidney injury
ALP	Alkaline phosphatase
APCs	Antigen presenting cells
ATP	Adenosine triphosphate
BUN	Blood urea nitrogen
BUV	Brilliant Ultraviolet
BW	Bodyweight
CAR	Chimeric antigen receptor
CCL	CC chemokine ligand
CCR	CC chemokine receptor
CDDSs	Cell-mediated drug delivery systems
cDNA	complementary DNA
CKD	Chronic kidney disease
CLP	Common lymphoid progenitor
CMP	Common myeloid progenitor
COL	Collagen
CTGF	Connective tissue growth factor

CTP	Cytidine triphosphate
CXCL	CXC motif chemokine ligand
CXCR	CXC motif chemokine receptor
Dest.	*Destillata*
DNA	Deoxyribonucleic acid
dNTPs	Deoxynucleotide triphosphates
DPBS	Dulbecco’s phosphate buffered saline
ECM	Extracellular matrix
EDTA	Ethylenediaminetetraacetic acid
e.g.	*exempli gratia*, for example
EGF	Epidermal growth factor
ELISA	Enzyme-linked immunosorbent assay
EMT	Epithelial-mesenchymal transition
ESRD	End-stage renal disease
FACS	Fluorescence activated cell sorting
FBS	Fetal Bovine Serum
FC	Fold change
FCS	Fetal calf serum
Fig	Figure
FITC	Fluorescein isothiocyanate
FOXP3	Forkhead box P3
FSC	Forward scatter
FSP1	Fibroblast-specific protein 1
g	gram
g	Relative centrifugal force

GEMs	Gel Beads-in-emulsion
GEX	Gene Expression
GFR	Glomerular filtration rate
GTP	Guanosine triphosphate
h/hrs	hour(s)
HRP	Streptavidin-Horseradish peroxidase
IFN	Interferon
IGF-1	Insulin-like growth factor 1
IL	Interleukin
INS	Intranuclear staining
IRI	Ischemia-reperfusion injury
KDIGO	Kidney Disease Improving Global Outcomes
KIM-1	Kidney injury molecule-1
m	milli
M	Molar
MACS	Magnetic activated cell sorting
MHC	Major histocompatibility complex
miRNA	microRNA
min	minute(s)
MSCs	Mesenchymal stem cells
n	Sample size
NK cells	Natural killer cells
ON	Overnight
PBS	Phosphate buffered saline
PDGF	Platelet-derived growth factor

PDGFR	Platelet-derived growth factor receptor
PD-L1/2	Programmed death ligand 1 and 2
PECAM1	Platelet and endothelial cell adhesion molecule 1
PerCP	Peridinin-chlorophyll-protein complex
PFA	Paraformaldehyde
pH	Potential of hydrogen
PTECs	Proximal tubular epithelial cells
qPCR	quantitative polymerase chain reaction
Rag1	Recombinase activating gene 1
RNA	Ribonucleic acid
RORγt	Retinoic acid-related orphan receptor γt
ROS	Reactive oxygen species
rpm	rounds per minute
RRT	Renal replacement therapy
RT	Real-time
RT	Room temperature
scRNAseq	single-cell RNA sequencing
sec	second(s)
SSC	Sideward scatter
Tab.	Table
T-bet	T-box expressed in T cells
TBM	Tubular basement membrane
TCR	T cell receptor
T_{EM}	Effector memory T cells
TGFβ	Transforming growth factor β

T_h cell	T helper cell
TNF	Tumor necrosis factor
TPP	Thiamine pyrophosphate
T_{regs}	Regulatory T cells
T_{RM}	Tissue-resident memory T cells
Tris-HCl	Tris-hydrochloride
U	Units
uIRI	unilateral ischemia-reperfusion injury
UMAP	Unsupervised uniform manifold approximation and projection
UREAL	Urea molecules in serum
VEGF	Vascular endothelial growth factor
Wnt	Wingless and Int-1
α	alpha
α-SMA	α-smooth muscle actin
β	beta
μ	Micro

12 References

1. Chawla, L.S., et al., Acute kidney disease and renal recovery: consensus report of the Acute Disease Quality Initiative (ADQI) 16 Workgroup. Nat Rev Nephrol, 2017. 13(4): p. 241-257.
2. Hariri, G. and M. Legrand, New drugs for acute kidney injury. J Intensive Med, 2025. 5(1): p. 3-11.
3. Simonini, M. and G. Vezzoli, New Landmarks to Slow the Progression of Chronic Kidney Disease. J Clin Med, 2022. 12(1).
4. Scott, R.P. and S.E. Quaggin, Review series: The cell biology of renal filtration. J Cell Biol, 2015. 209(2): p. 199-210.
5. Kurts, C., et al., Kidney immunology from pathophysiology to clinical translation. Nat Rev Immunol, 2025.
6. Madrazo-Ibarra, A. and P. Vaitla, Histology, Nephron. StatPearls, 2025.
7. Lindstrom, N.O., et al., Conserved and Divergent Features of Human and Mouse Kidney Organogenesis. J Am Soc Nephrol, 2018. 29(3): p. 785-805.
8. Schnell, J., M. Achieng, and N.O. Lindstrom, Principles of human and mouse nephron development. Nat Rev Nephrol, 2022. 18(10): p. 628-642.
9. Reiser, J. and M.M. Altintas, Podocytes. F1000Res, 2016. 5.
10. Menon, M.C., P.Y. Chuang, and C.J. He, The glomerular filtration barrier: components and crosstalk. Int J Nephrol, 2012. 2012: p. 749010.
11. Haraldsson, B., J. Nystrom, and W.M. Deen, Properties of the glomerular barrier and mechanisms of proteinuria. Physiol Rev, 2008. 88(2): p. 451-87.
12. Soriano, R.M., D. Penfold, and S.W. Leslie Anatomy, Abdomen and Pelvis: Kidneys. 2023.
13. Daehn, I.S. and J.S. Duffield, The glomerular filtration barrier: a structural target for novel kidney therapies. Nat Rev Drug Discov, 2021. 20(10): p. 770-788.
14. Camici, M., Renal glomerular permselectivity and vascular endothelium. Biomed Pharmacother, 2005. 59(1-2): p. 30-7.
15. Leatherby, R.J., C. Theodorou, and R. Dhanda, Renal physiology: blood flow, glomerular filtration and plasma clearance. Anaesthesia and Intensive Care Medicine, 2021. 22(7): p. 439-442.
16. Vegt, E., et al., Renal toxicity of radiolabeled peptides and antibody fragments: mechanisms, impact on radionuclide therapy, and strategies for prevention. J Nucl Med, 2010. 51(7): p. 1049-58.
17. Vallon, V., Molecular determinants of renal glucose reabsorption. Focus on "Glucose transport by human renal Na+/D-glucose cotransporters SGLT1 and SGLT2". Am J Physiol Cell Physiol, 2011. 300(1): p. C6-8.

18. Rozansky, D.J., The role of aldosterone in renal sodium transport. Semin Nephrol, 2006. 26(2): p. 173-81.

19. Wang, K. and B. Kestenbaum, Proximal Tubular Secretory Clearance: A Neglected Partner of Kidney Function. Clin J Am Soc Nephrol, 2018. 13(8): p. 1291-1296.

20. Hoste, E.A.J., et al., Global epidemiology and outcomes of acute kidney injury. Nat Rev Nephrol, 2018. 14(10): p. 607-625.

21. Lafrance, J.P. and D.R. Miller, Acute kidney injury associates with increased long-term mortality. J Am Soc Nephrol, 2010. 21(2): p. 345-52.

22. Ostermann, M., et al., Acute kidney injury. Lancet, 2025. 405(10474): p. 241-256.

23. Hsu, R.K. and C.Y. Hsu, The Role of Acute Kidney Injury in Chronic Kidney Disease. Semin Nephrol, 2016. 36(4): p. 283-92.

24. Kellum, J.A., et al., Acute kidney injury. Nat Rev Dis Primers, 2021. 7(1): p. 52.

25. Stevens, P.E., et al., KDIGO 2024 Clinical Practice Guideline for the Evaluation and Management of Chronic Kidney Disease. Kidney International, 2024. 105(4): p. S117-S314.

26. Strauss, C., et al., Biomarkers of acute kidney injury: From discovery to the future of clinical practice. J Clin Anesth, 2024. 95: p. 111458.

27. Washinger, K., Acute Kidney Injury in Adults: An Underdiagnosed Condition. Jnp- the Journal for Nurse Practitioners, 2017. 13(10): p. 667-+.

28. Turgut, F., A.S. Awad, and E.M. Abdel-Rahman, Acute Kidney Injury: Medical Causes and Pathogenesis. J Clin Med, 2023. 12(1).

29. Brown, A., S. Kumar, and P.B. Tchounwou, Cisplatin-Based Chemotherapy of Human Cancers. J Cancer Sci Ther, 2019. 11(4).

30. Galanski, M.S., M.A. Jakupec, and B.K. Keppler, Update of the Preclinical Situation of Anticancer Platinum Complexes: Novel Design Strategies and Innovative Analytical Approaches. Curr Med Chem, 2005. 12(18): p. 2075-94.

31. Dasari, S. and P.B. Tchounwou, Cisplatin in cancer therapy: molecular mechanisms of action. Eur J Pharmacol, 2014. 740: p. 364-78.

32. Latcha, S., et al., Long-Term Renal Outcomes after Cisplatin Treatment. Clin J Am Soc Nephrol, 2016. 11(7): p. 1173-1179.

33. Lim, Y.J., et al., Metabolomic identification of predictive and early biomarkers of cisplatin-induced acute kidney injury in adult head and neck cancer patients. Br J Clin Pharmacol, 2024. 90(8): p. 1790-1803.

34. Sears, S.M., A. Orwick, and L.J. Siskind, Modeling Cisplatin-Induced Kidney Injury to Increase Translational Potential. Nephron, 2023. 147(1): p. 13-16.

35. Oh, G.S., et al., Cisplatin-induced Kidney Dysfunction and Perspectives on Improving Treatment Strategies. Electrolyte Blood Press, 2014. 12(2): p. 55-65.

36. Yao, X., et al., Cisplatin nephrotoxicity: a review. Am J Med Sci, 2007. 334(2): p. 115-24.

37. Miller, R.P., et al., Mechanisms of Cisplatin nephrotoxicity. Toxins (Basel), 2010. 2(11): p. 2490-518.

38. Ahmad, S., Kinetic aspects of platinum anticancer agents. Polyhedron, 2017. 138: p. 109-124.

39. Wang, D. and S.J. Lippard, Cellular processing of platinum anticancer drugs. Nat Rev Drug Discov, 2005. 4(4): p. 307-20.

40. Romani, A.M.P., Cisplatin in cancer treatment. Biochem Pharmacol, 2022. 206: p. 115323.

41. Pervushin, N.V., et al., Cisplatin Resistance and Metabolism: Simplification of Complexity. Cancers (Basel), 2024. 16(17).

42. Eymael, J. and B. Smeets, Origin and fate of the regenerating cells of the kidney. Eur J Pharmacol, 2016. 790: p. 62-73.

43. Chen, H. and L.W. Busse, Novel Therapies for Acute Kidney Injury. Kidney Int Rep, 2017. 2(5): p. 785-799.

44. Rayego-Mateos, S., et al., Molecular Mechanisms of Kidney Injury and Repair. Int J Mol Sci, 2022. 23(3).

45. Beamish, J.A., J.A. Watts, and G.R. Dressler, Gene regulation in regeneration after acute kidney injury. J Biol Chem, 2024. 300(8): p. 107520.

46. Huang, R., P. Fu, and L. Ma, Kidney fibrosis: from mechanisms to therapeutic medicines. Signal Transduct Target Ther, 2023. 8(1): p. 129.

47. Chou, Y.H., T.M. Huang, and T.S. Chu, Novel insights into acute kidney injury-chronic kidney disease continuum and the role of renin-angiotensin system. J Formos Med Assoc, 2017. 116(9): p. 652-659.

48. Ekart, R., et al., Chronic kidney disease progression to end stage renal disease: a single center experience of the role of the underlying kidney disease. Ther Apher Dial, 2013. 17(4): p. 363-7.

49. Hashmi, M., O. Benjamin, and S. Lappin, End-Stage Renal Disease. StatPearls, 2023.

50. Francis, A., et al., Chronic kidney disease and the global public health agenda: an international consensus. Nat Rev Nephrol, 2024. 20(7): p. 473-485.

51. Hsu, C.Y., et al., The risk of acute renal failure in patients with chronic kidney disease. Kidney Int, 2008. 74(1): p. 101-7.

52. Onuigbo, M.A., Syndrome of rapid-onset end-stage renal disease: a new unrecognized pattern of CKD progression to ESRD. Ren Fail, 2010. 32(8): p. 954-8.

53. Mihai, S., et al., Inflammation-Related Mechanisms in Chronic Kidney Disease Prediction, Progression, and Outcome. J Immunol Res, 2018. 2018: p. 2180373.

54. Frak, W., et al., New Insights into Molecular Mechanisms of Chronic Kidney Disease. Biomedicines, 2022. 10(11).

55. Vasyutina, E. and M. Treier, Molecular mechanisms in renal degenerative disease. Semin Cell Dev Biol, 2010. 21(8): p. 831-7.

56. Willis, B.C., R.M. duBois, and Z. Borok, Epithelial origin of myofibroblasts during fibrosis in the lung. Proc Am Thorac Soc, 2006. 3(4): p. 377-82.

57. Luo, L., et al., The role of epithelial cells in fibrosis: Mechanisms and treatment. Pharmacol Res, 2024. 202: p. 107144.

58. Li, M., et al., Epithelial-mesenchymal transition: An emerging target in tissue fibrosis. Exp Biol Med (Maywood), 2016. 241(1): p. 1-13.

59. Mack, M. and M. Yanagita, Origin of myofibroblasts and cellular events triggering fibrosis. Kidney International, 2015. 87(2): p. 297-307.

60. Vivier, E. and B. Malissen, Innate and adaptive immunity: specificities and signaling hierarchies revisited. Nat Immunol, 2005. 6(1): p. 17-21.

61. Wang, R., et al., The interaction of innate immune and adaptive immune system. MedComm (2020), 2024. 5(10): p. e714.

62. Dempsey, P.W., S.A. Vaidya, and G. Cheng, The art of war: Innate and adaptive immune responses. Cell Mol Life Sci, 2003. 60(12): p. 2604-21.

63. Marshall, J.S., et al., An introduction to immunology and immunopathology. Allergy Asthma Clin Immunol, 2018. 14(Suppl 2): p. 49.

64. Petrie, H.T., et al., T cell receptor gene recombination patterns and mechanisms: cell death, rescue, and T cell production. J Exp Med, 1995. 182(1): p. 121-7.

65. Patel, A.A., F. Ginhoux, and S. Yona, Monocytes, macrophages, dendritic cells and neutrophils: an update on lifespan kinetics in health and disease. Immunology, 2021. 163(3): p. 250-261.

66. Kolaczkowska, E. and P. Kubes, Neutrophil recruitment and function in health and inflammation. Nat Rev Immunol, 2013. 13(3): p. 159-75.

67. Bargatze, R.F., et al., Neutrophils roll on adherent neutrophils bound to cytokine-induced endothelial cells via L-selectin on the rolling cells. J Exp Med, 1994. 180(5): p. 1785-92.

68. Lever, J.M., et al., Resident macrophages reprogram toward a developmental state after acute kidney injury. JCI Insight, 2019. 4(2).

69. Lee, S.A., et al., Role of Immune Cells in Acute Kidney Injury and Repair. Nephron, 2017. 137(4): p. 282-286.

70. Deng, B., et al., The leukotriene B(4)-leukotriene B(4) receptor axis promotes cisplatin-induced acute kidney injury by modulating neutrophil recruitment. Kidney Int, 2017. 92(1): p. 89-100.

71. Bolisetty, S. and A. Agarwal, Neutrophils in acute kidney injury: not neutral any more. Kidney Int, 2009. 75(7): p. 674-6.

72. Tadagavadi, R.K. and W.B. Reeves, Neutrophils in cisplatin AKI—mediator or marker? Kidney International, 2017. 92(1): p. 11-13.

73. Dellepiane, S., J.S. Leventhal, and P. Cravedi, T Cells and Acute Kidney Injury: A Two-Way Relationship. Front Immunol, 2020. 11: p. 1546.

74. Tang, P.M., D.J. Nikolic-Paterson, and H.Y. Lan, Macrophages: versatile players in renal inflammation and fibrosis. Nat Rev Nephrol, 2019. 15(3): p. 144-158.

75. Wang, X., et al., The Role of Macrophages in Kidney Fibrosis. Front Physiol, 2021. 12: p. 705838.

76. Li, X., et al., Role of M2 Macrophages in Sepsis-Induced Acute Kidney Injury. Shock, 2018. 50(2): p. 233-239.

77. Lee, S., et al., Distinct macrophage phenotypes contribute to kidney injury and repair. J Am Soc Nephrol, 2011. 22(2): p. 317-26.

78. Chen, S., et al., Macrophages in immunoregulation and therapeutics. Signal Transduct Target Ther, 2023. 8(1): p. 207.

79. Aggarwal, S., et al., SOX9 switch links regeneration to fibrosis at the single-cell level in mammalian kidneys. Science, 2024. 383(6685): p. eadd6371.

80. Cantoni, C., et al., Recent Advances in the Role of Natural Killer Cells in Acute Kidney Injury. Front Immunol, 2020. 11: p. 1484.

81. Artis, D. and H. Spits, The biology of innate lymphoid cells. Nature, 2015. 517(7534): p. 293-301.

82. Vivier, E., et al., Functions of natural killer cells. Nat Immunol, 2008. 9(5): p. 503-10.

83. Kim, H.J., et al., TLR2 signaling in tubular epithelial cells regulates NK cell recruitment in kidney ischemia-reperfusion injury. J Immunol, 2013. 191(5): p. 2657-64.

84. Kim, H.J., et al., Reverse signaling through the costimulatory ligand CD137L in epithelial cells is essential for natural killer cell-mediated acute tissue inflammation. Proc Natl Acad Sci U S A, 2012. 109(1): p. E13-22.

85. Zhang, Z.X., et al., NK cells induce apoptosis in tubular epithelial cells and contribute to renal ischemia-reperfusion injury. J Immunol, 2008. 181(11): p. 7489-98.

86. Victorino, F., et al., Tissue-Resident NK Cells Mediate Ischemic Kidney Injury and Are Not Depleted by Anti-Asialo-GM1 Antibody. J Immunol, 2015. 195(10): p. 4973-85.

87. Lee, K., H.R. Jang, and H. Rabb, Lymphocytes and innate immune cells in acute kidney injury and repair. Nat Rev Nephrol, 2024. 20(12): p. 789-805.

88. Bonilla, F.A. and H.C. Oettgen, Adaptive immunity. J Allergy Clin Immunol, 2010. 125(2 Suppl 2): p. S33-40.

89. Luckheeram, R.V., et al., CD4(+)T cells: differentiation and functions. Clin Dev Immunol, 2012. 2012: p. 925135.

90. Chatzileontiadou, D.S.M., et al., The Many Faces of CD4(+) T Cells: Immunological and Structural Characteristics. Int J Mol Sci, 2020. 22(1).

91. Kunzli, M. and D. Masopust, CD4(+) T cell memory. Nat Immunol, 2023. 24(6): p. 903-914.

92. Wan, Y.Y. and R.A. Flavell, How diverse--CD4 effector T cells and their functions. J Mol Cell Biol, 2009. 1(1): p. 20-36.

93. Groom, J.R. and A.D. Luster, CXCR3 in T cell function. Exp Cell Res, 2011. 317(5): p. 620-31.

94. Sun, L., et al., T cells in health and disease. Signal Transduct Target Ther, 2023. 8(1): p. 235.

95. Sun, S., et al., Immunoregulatory mechanism of acute kidney injury in sepsis: A Narrative Review. Biomed Pharmacother, 2023. 159: p. 114202.

96. Hondowicz, B.D., et al., IL-2 is required for the generation of viral-specific CD4(+) Th1 tissue-resident memory cells and B cells are essential for maintenance in the lung. Eur J Immunol, 2018. 48(1): p. 80-86.

97. De Fanis, U., et al., GATA3 up-regulation associated with surface expression of CD294/CRTH2: a unique feature of human Th cells. Blood, 2007. 109(10): p. 4343-50.

98. Kokubo, K., et al., Conventional and pathogenic Th2 cells in inflammation, tissue repair, and fibrosis. Front Immunol, 2022. 13: p. 945063.

99. Yokota, N., et al., Contrasting roles for STAT4 and STAT6 signal transduction pathways in murine renal ischemia-reperfusion injury. Am J Physiol Renal Physiol, 2003. 285(2): p. F319-25.

100. Acosta-Rodriguez, E.V., et al., Surface phenotype and antigenic specificity of human interleukin 17-producing T helper memory cells. Nat Immunol, 2007. 8(6): p. 639-46.

101. Han, L., et al., Th17 cells in autoimmune diseases. Front Med, 2015. 9(1): p. 10-9.

102. Chung, Y., et al., Critical regulation of early Th17 cell differentiation by interleukin-1 signaling. Immunity, 2009. 30(4): p. 576-87.

103. Pindjakova, J., et al., Interleukin-1 accounts for intrarenal Th17 cell activation during ureteral obstruction. Kidney Int, 2012. 81(4): p. 379-90.

104. Mehrotra, P., et al., Th-17 cell activation in response to high salt following acute kidney injury is associated with progressive fibrosis and attenuated by AT-1R antagonism. Kidney Int, 2015. 88(4): p. 776-84.

105. Burne, M.J., et al., Identification of the CD4(+) T cell as a major pathogenic factor in ischemic acute renal failure. J Clin Invest, 2001. 108(9): p. 1283-90.

106. Liu, M., et al., A pathophysiologic role for T lymphocytes in murine acute cisplatin nephrotoxicity. J Am Soc Nephrol, 2006. 17(3): p. 765-74.

107. Nikolic-Paterson, D.J., CD4+ T cells: a potential player in renal fibrosis. Kidney International, 2010. 78(4): p. 333-335.

108. Sakaguchi, S., et al., Foxp3+ CD25+ CD4+ natural regulatory T cells in dominant self-tolerance and autoimmune disease. Immunol Rev, 2006. 212: p. 8-27.

109. Hori, S., T. Nomura, and S. Sakaguchi, Control of regulatory T cell development by the transcription factor Foxp3. Science, 2003. 299(5609): p. 1057-61.

110. Gandolfo, M.T., et al., Foxp3+ regulatory T cells participate in repair of ischemic acute kidney injury. Kidney Int, 2009. 76(7): p. 717-29.

111. Kinsey, G.R., et al., Regulatory T cells suppress innate immunity in kidney ischemia-reperfusion injury. J Am Soc Nephrol, 2009. 20(8): p. 1744-53.

112. Lee, H., et al., CD4+CD25+ regulatory T cells attenuate cisplatin-induced nephrotoxicity in mice. Kidney Int, 2010. 78(11): p. 1100-9.

113. Sharma, R. and G.R. Kinsey, Regulatory T cells in acute and chronic kidney diseases. Am J Physiol Renal Physiol, 2018. 314(5): p. F679-F698.

114. Jaworska, K., et al., Both PD-1 ligands protect the kidney from ischemia reperfusion injury. J Immunol, 2015. 194(1): p. 325-33.

115. do Valle Duraes, F., et al., Immune cell landscaping reveals a protective role for regulatory T cells during kidney injury and fibrosis. JCI Insight, 2020. 5(3).

116. Shah, K., et al., T cell receptor (TCR) signaling in health and disease. Signal Transduct Target Ther, 2021. 6(1): p. 412.

117. Dhatchinamoorthy, K., J.D. Colbert, and K.L. Rock, Cancer Immune Evasion Through Loss of MHC Class I Antigen Presentation. Front Immunol, 2021. 12: p. 636568.

118. Ascon, D.B., et al., Normal mouse kidneys contain activated and CD3+CD4- CD8- double-negative T lymphocytes with a distinct TCR repertoire. J Leukoc Biol, 2008. 84(6): p. 1400-9.

119. Jiang, W., et al., CD8 T cells induce the peritubular capillary rarefaction during AKI to CKD transition. Int J Biol Sci, 2024. 20(8): p. 2980-2993.

120. Chawla, L.S. and P.L. Kimmel, Acute kidney injury and chronic kidney disease: an integrated clinical syndrome. Kidney International, 2012. 82(5): p. 516-524.

121. Kovesdy, C.P., Epidemiology of chronic kidney disease: an update 2022. Kidney Int Suppl (2011), 2022. 12(1): p. 7-11.

122. Rhee, C.M. and C.P. Kovesdy, Epidemiology: Spotlight on CKD deaths-increasing mortality worldwide. Nat Rev Nephrol, 2015. 11(4): p. 199-200.

123. Courtoy, G.E., et al., Digital Image Analysis of Picrosirius Red Staining: A Robust Method for Multi-Organ Fibrosis Quantification and Characterization. Biomolecules, 2020. 10(11).

124. Digby, J.L.M., et al., Evaluation of cisplatin-induced injury in human kidney organoids. Am J Physiol Renal Physiol, 2020. 318(4): p. F971-F978.

125. Viau, A., et al., Lipocalin 2 is essential for chronic kidney disease progression in mice and humans. J Clin Invest, 2010. 120(11): p. 4065-76.

126. He, Y.X., et al., Wnt4 is significantly upregulated during the early phases of cisplatin-induced acute kidney injury. Sci Rep, 2018. 8(1): p. 10555.

127. Bolisetty, S., et al., Proximal tubule-targeted heme oxygenase-1 in cisplatin-induced acute kidney injury. Am J Physiol Renal Physiol, 2016. 310(5): p. F385-94.

128. Yang, B., et al., Caspase-3 and apoptosis in experimental chronic renal scarring. Kidney Int, 2001. 60(5): p. 1765-76.

129. Chen, C., et al., Genetic Knockout of Fatty Acid Amide Hydrolase Ameliorates Cisplatin-Induced Nephropathy in Mice. Mol Pharmacol, 2023. 103(4): p. 230-240.

130. Gao, Q., et al., CDKN1A promotes Cis-induced AKI by inducing cytoplasmic ROS production and ferroptosis. Food Chem Toxicol, 2024. 193: p. 115003.

131. Su, X., et al., Slc25a21 in cisplatin-induced acute kidney injury: a new target for renal tubular epithelial protection by regulating mitochondrial metabolic homeostasis. Cell Death Dis, 2024. 15(12): p. 891.

132. Tran, M., et al., TEAD1 Prevents Necroptosis and Inflammation in Cisplatin-Induced Acute Kidney Injury Through Maintaining Mitochondrial Function. Int J Biol Sci, 2025. 21(2): p. 565-578.

133. van Angelen, A.A., et al., Cisplatin-induced injury of the renal distal convoluted tubule is associated with hypomagnesaemia in mice. Nephrol Dial Transplant, 2013. 28(4): p. 879-89.

134. Guo, X., et al., APOBEC-1 deletion enhances cisplatin-induced acute kidney injury. Sci Rep, 2023. 13(1): p. 22255.

135. Xiao, Y., et al., GSTA3 regulates TGF-beta1-induced renal interstitial fibrosis in NRK-52E cells as a component of the PI3K-Keap1/Nrf2 pathway. J Int Med Res, 2019. 47(11): p. 5787-5801.

136. Grewal, J.S., J.Y. Tsai, and S.R. Khan, Oxalate-inducible AMBP gene and its regulatory mechanism in renal tubular epithelial cells. Biochem J, 2005. 387(Pt 3): p. 609-16.

137. Vaidya, V.S., M.A. Ferguson, and J.V. Bonventre, Biomarkers of acute kidney injury. Annu Rev Pharmacol Toxicol, 2008. 48: p. 463-93.

138. Yin, C. and N. Wang, Kidney injury molecule-1 in kidney disease. Renal Failure, 2016. 38:10: p. 1567-1573.

139. Han, W.K., et al., Kidney Injury Molecule-1 (KIM-1): a novel biomarker for human renal proximal tubule injury. Kidney Int, 2002. 62(1): p. 237-44.

140. Bailly, V., et al., Shedding of kidney injury molecule-1, a putative adhesion protein involved in renal regeneration. J Biol Chem, 2002. 277(42): p. 39739-48.

141. Garcia-Pastor, C., et al., Apoptosis and cell proliferation in proximal tubular cells exposed to apoptotic bodies. Novel pathophysiological implications in cisplatin-induced renal injury. Biochim Biophys Acta Mol Basis Dis, 2019. 1865(9): p. 2504-2515.

142. Salazar, J.H., Overview of Urea and Creatinine Laboratory Medicine, 2014. 45(1): p. 19-20.

143. Gounden, V., H. Bhatt, and I. Jialal, Renal Function Tests. StatPearls Publishing, 2024.

144. Ponder, K.G. and L.H. Boise, The prodomain of caspase-3 regulates its own removal and caspase activation. Cell Death Discov, 2019. 5: p. 56.

145. Duan, W.R., et al., Comparison of immunohistochemistry for activated caspase-3 and cleaved cytokeratin 18 with the TUNEL method for quantification of apoptosis in histological sections of PC-3 subcutaneous xenografts. J Pathol, 2003. 199(2): p. 221-8.

146. Sharp, C.N., et al., Repeated administration of low-dose cisplatin in mice induces fibrosis. Am J Physiol Renal Physiol, 2016. 310(6): p. F560-8.

147. Zhao, X., et al., New insights into fibrosis from the ECM degradation perspective: the macrophage-MMP-ECM interaction. Cell Biosci, 2022. 12(1): p. 117.

148. Street, J.M., et al., Automated quantification of renal fibrosis with Sirius Red and polarization contrast microscopy. Physiol Rep, 2014. 2(7).

149. Jiao, D., et al., Changes in aging-induced kidney dysfunction in mice based on a metabolomics analysis. Front Endocrinol (Lausanne), 2022. 13: p. 959311.

150. Ma, K., et al., The suppression of sepsis-induced kidney injury via the knockout of T lymphocytes. Heliyon, 2024. 10(1): p. e23311.

151. Lee, K. and H.R. Jang, Role of T cells in ischemic acute kidney injury and repair. Korean J Intern Med, 2022. 37(3): p. 534-550.

152. Mombaerts, P., et al., RAG-1-deficient mice have no mature B and T lymphocytes. Cell, 1992. 68(5): p. 869-77.

153. Yang, S., et al., The shedding of CD62L (L-selectin) regulates the acquisition of lytic activity in human tumor reactive T lymphocytes. PLoS One, 2011. 6(7): p. e22560.

154. Hengel, R.L., et al., Cutting edge: L-selectin (CD62L) expression distinguishes small resting memory CD4+ T cells that preferentially respond to recall antigen. J Immunol, 2003. 170(1): p. 28-32.

155. Schumann, J., et al., Differences in CD44 Surface Expression Levels and Function Discriminates IL-17 and IFN-gamma Producing Helper T Cells. PLoS One, 2015. 10(7): p. e0132479.

156. Sckisel, G.D., et al., Differential phenotypes of memory CD4 and CD8 T cells in the spleen and peripheral tissues following immunostimulatory therapy. J Immunother Cancer, 2017. 5: p. 33.

157. Pinheiro, H.S., et al., Contribution of CD4+ T cells to the early mechanisms of ischemia-reperfusion injury in a mouse model of acute renal failure. Braz J Med Biol Res, 2007. 40(4): p. 557-68.

158. Ascon, M., et al., Renal ischemia-reperfusion leads to long term infiltration of activated and effector-memory T lymphocytes. Kidney Int, 2009. 75(5): p. 526-35.

159. Papalexi, E. and R. Satija, Single-cell RNA sequencing to explore immune cell heterogeneity. Nat Rev Immunol, 2018. 18(1): p. 35-45.

160. Amirrah, I.N., et al., A Comprehensive Review on Collagen Type I Development of Biomaterials for Tissue Engineering: From Biosynthesis to Bioscaffold. Biomedicines, 2022. 10(9).

161. Tarnutzer, K., et al., Collagen constitutes about 12% in females and 17% in males of the total protein in mice. Sci Rep, 2023. 13(1): p. 4490.

162. Genovese, F., et al., Imbalanced turnover of collagen type III is associated with disease progression and mortality in high-risk chronic kidney disease patients. Clin Kidney J, 2021. 14(2): p. 593-601.

163. Arrindell, J. and B. Desnues, Vimentin: from a cytoskeletal protein to a critical modulator of immune response and a target for infection. Front Immunol, 2023. 14: p. 1224352.

164. Cao, Y.H., et al., Urinary vimentin mRNA as a potential novel biomarker of renal fibrosis. Am J Physiol Renal Physiol, 2015. 309(6): p. F514-22.

165. Sun, C., et al., Transgelin promotes lung cancer progression via activation of cancer-associated fibroblasts with enhanced IL-6 release. Oncogenesis, 2023. 12(1): p. 18.

166. Agarwal, S.K., F.K. Tan, and F.C. Arnett, Genetics and genomic studies in scleroderma (systemic sclerosis). Rheum Dis Clin North Am, 2008. 34(1): p. 17-40; v.

167. Perse, M., Cisplatin Mouse Models: Treatment, Toxicity and Translatability. Biomedicines, 2021. 9(10).

168. Freitas-Lima, L.C., et al., PPAR-alpha Deletion Attenuates Cisplatin Nephrotoxicity by Modulating Renal Organic Transporters MATE-1 and OCT-2. Int J Mol Sci, 2020. 21(19).

169. Zha, M., et al., The circadian clock gene Bmal1 facilitates cisplatin-induced renal injury and hepatization. Cell Death Dis, 2020. 11(6): p. 446.

170. Torres, R., et al., Three-Dimensional Morphology by Multiphoton Microscopy with Clearing in a Model of Cisplatin-Induced CKD. J Am Soc Nephrol, 2016. 27(4): p. 1102-12.

171. Fu, Y., et al., Chronic effects of repeated low-dose cisplatin treatment in mouse kidneys and renal tubular cells. Am J Physiol Renal Physiol, 2019. 317(6): p. F1582-F1592.

172. Perse, M. and Z. Veceric-Haler, Cisplatin-Induced Rodent Model of Kidney Injury: Characteristics and Challenges. Biomed Res Int, 2018. 2018: p. 1462802.

173. Liu, J., et al., Molecular characterization of the transition from acute to chronic kidney injury following ischemia/reperfusion. JCI Insight, 2017. 2(18).

174. Zachariah, S., et al., Clinical Pharmacy Education, Practice and Research: Clinical Pharmacy, Drug Information, Pharmacovigilance, Pharmacoeconomics and Clinical Research. Chapter 7 - Interpretation of Laboratory Data and General Physical Examination by Pharmacists, ed. D. Thomas. 2019. 91-108.

175. Wei, Q. and Z. Dong, Mouse model of ischemic acute kidney injury: technical notes and tricks. Am J Physiol Renal Physiol, 2012. 303(11): p. F1487-94.

176. Ganguly, A., et al., Time-course analysis of cisplatin induced AKI in preclinical models: implications for testing different sources of MSCs. J Transl Med, 2024. 22(1): p. 789.

177. Zheng, Z., et al., NLRP3 associated with chronic kidney disease progression after ischemia/reperfusion-induced acute kidney injury. Cell Death Discov, 2021. 7(1): p. 324.

178. Zhang, T., R.E. Widdop, and S.D. Ricardo, Transition from acute kidney injury to chronic kidney disease: mechanisms, models, and biomarkers. Am J Physiol Renal Physiol, 2024. 327(5): p. F788-F805.

179. dos Santos, N.A., et al., Cisplatin-induced nephrotoxicity and targets of nephroprotection: an update. Arch Toxicol, 2012. 86(8): p. 1233-50.

180. Servais, H., et al., Renal cell apoptosis induced by nephrotoxic drugs: cellular and molecular mechanisms and potential approaches to modulation. Apoptosis, 2008. 13(1): p. 11-32.

181. Hosohata, K., Role of Oxidative Stress in Drug-Induced Kidney Injury. Int J Mol Sci, 2016. 17(11).

182. Ramesh, G. and W.B. Reeves, TNF-α mediates chemokine and cytokine expression and renal injury in cisplatin nephrotoxicity. The Journal of clinical investigation, 2002. 110(6): p. 835-842.

183. Wei, Q., et al., Activation and involvement of p53 in cisplatin-induced nephrotoxicity. Am J Physiol Renal Physiol, 2007. 293(4): p. F1282-91.

184. Kim, M.G., et al., The Role of M2 Macrophages in the Progression of Chronic Kidney Disease following Acute Kidney Injury. PLoS One, 2015. 10(12): p. e0143961.

185. Gharaie Fathabad, S., et al., T Lymphocytes in Acute Kidney Injury and Repair. Semin Nephrol, 2020. 40(2): p. 114-125.

186. Burne-Taney, M.J., N. Yokota, and H. Rabb, Persistent renal and extrarenal immune changes after severe ischemic injury. Kidney Int, 2005. 67(3): p. 1002-9.

187. Schreiner, D. and C.G. King, CD4+ Memory T Cells at Home in the Tissue: Mechanisms for Health and Disease. Front Immunol, 2018. 9: p. 2394.

188. Szabo, P.A., M. Miron, and D.L. Farber, Location, location, location: Tissue resident memory T cells in mice and humans. Sci Immunol, 2019. 4(34).

189. Ginsberg, P., U. Panzer, and N. Asada, Tissue-resident memory T cells in renal autoimmune diseases. Front Immunol, 2023. 14: p. 1111521.

190. Asada, N., et al., Tissue-resident memory T cells in the kidney. Semin Immunopathol, 2022. 44(6): p. 801-811.

191. Turner, J.E., et al., Tissue-Resident Lymphocytes in the Kidney. J Am Soc Nephrol, 2018. 29(2): p. 389-399.

192. Alikhan, M.A., et al., Regulatory T cells in renal disease. Clin Transl Immunology, 2018. 7(1): p. e1004.

193. Singh, M., et al., Isolation, culture, and characterization of primary kidney fibroblasts from human patients with chronic antibody-mediated kidney transplant rejection. Indian J Transplant, 2024(18): p. 431-435.

194. Saraswati, S., et al., Renal fibroblasts are involved in fibrogenic changes in kidney fibrosis associated with dysfunctional telomeres. Exp Mol Med, 2024. 56(10): p. 2216-2230.

195. Nakai, T., Y. Iwamura, and N. Suzuki, Efficient isolation of interstitial fibroblasts directly from mouse kidneys or indirectly after ex vivo expansion. STAR Protoc, 2021. 2(4): p. 100826.

196. Duarte, A.S., A. Correia, and A.C. Esteves, Bacterial collagenases - A review. Crit Rev Microbiol, 2016. 42(1): p. 106-26.

197. Eckhard, U., et al., Biochemical characterization of the catalytic domains of three different Clostridial collagenases. Biol Chem, 2009. 390(1): p. 11-8.

198. Morgado-Pascual, J.L., et al., Epigenetic Modification Mechanisms Involved in Inflammation and Fibrosis in Renal Pathology. Mediators Inflamm, 2018. 2018: p. 2931049.

199. Tanemoto, F. and I. Mimura, Therapies Targeting Epigenetic Alterations in Acute Kidney Injury-to-Chronic Kidney Disease Transition. Pharmaceuticals (Basel), 2022. 15(2).

200. Gao, L., et al., Potential targeted therapy and diagnosis based on novel insight into growth factors, receptors, and downstream effectors in acute kidney injury and acute kidney injury-chronic kidney disease progression. Signal Transduct Target Ther, 2020. 5(1): p. 9.

201. Yuan, L., et al., VEGF-modified human embryonic mesenchymal stem cell implantation enhances protection against cisplatin-induced acute kidney injury. Am J Physiol Renal Physiol, 2011. 300(1): p. F207-18.

202. Huffstater, T., W.D. Merryman, and L.S. Gewin, Wnt/beta-Catenin in Acute Kidney Injury and Progression to Chronic Kidney Disease. Semin Nephrol, 2020. 40(2): p. 126-137.

203. Fernandez-Ruiz, D., et al., Liver-Resident Memory CD8(+) T Cells Form a Front-Line Defense against Malaria Liver-Stage Infection. Immunity, 2016. 45(4): p. 889-902.

204. Seddon, B., P. Tomlinson, and R. Zamoyska, Interleukin 7 and T cell receptor signals regulate homeostasis of CD4 memory cells. Nat Immunol, 2003. 4(7): p. 680-6.

205. Diaz-Ruano, A.B., et al., Advances in the use of nanoparticles for specific cell-target delivery of anti-cancer agents. Life Sci, 2025. 371: p. 123604.

206. Riley, R.S., et al., Delivery technologies for cancer immunotherapy. Nat Rev Drug Discov, 2019. 18(3): p. 175-196.

207. Zhang, H., et al., New avenues for cancer immunotherapy: Cell-mediated drug delivery systems. J Control Release, 2024. 375: p. 712-732.

208. Yu, H., et al., Cell-mediated targeting drugs delivery systems. Drug Deliv, 2020. 27(1): p. 1425-1437.

209. Asmamaw, M. and B. Zawdie, Mechanism and Applications of CRISPR/Cas-9-Mediated Genome Editing. Biologics, 2021. 15: p. 353-361.

210. Sterner, R.C. and R.M. Sterner, CAR-T cell therapy: current limitations and potential strategies. Blood Cancer J, 2021. 11(4): p. 69.

13 Declaration of personal contribution

Table 10: Detailed declaration of personal contribution to the doctoral thesis at hand

Tasks carried out	**Persons involved**
Conceptualisation of the project	Jan-Eric Turner, Lena Henneken, Ulf Panzer
Realisation of experiments	Lena Henneken, Virginia Adamiak, Nikhat Shaikh, Anna Kaffke, Nick Rosenkranz, Hans-Joachim Paust, Anett Peters, Pauline Ginsberg
Analysis of experimental data	Lena Henneken
Analysis of single-cell RNA sequencing data	Pauline Ginsberg
Analysis of immunohistochemistry	Lena Henneken
Visualisation of results	Lena Henneken
Writing of the original manuscript	Lena Henneken
Editing of the original manuscript	Jan-Eric Turner
Provision of the funding	Jan-Eric Turner, Ulf Panzer, SFB 1192

14 Eidesstattliche Erklärung

Hiermit versichere ich an Eides statt, die vorliegende Dissertation selbst verfasst und keine anderen als die angegebenen Hilfsmittel und Quellen benutzt zu haben.
Sofern im Zuge der Erstellung der vorliegenden Dissertationsschrift generative Künstliche Intelligenz (gKI) basierte elektronische Hilfsmittel verwendet wurden, versichere ich, dass meine eigene Leistung im Vordergrund stand und dass eine vollständige Dokumentation aller verwendeten Hilfsmittel gemäß der Guten wissenschaftlichen Praxis vorliegt. Ich trage die Verantwortung für eventuell durch die gKI generierte fehlerhafte oder verzerrte Inhalte, fehlerhafte Referenzen, Verstöße gegen das Datenschutz- und Urheberrecht oder Plagiate.

I hereby declare and affirm that this doctoral dissertation is my own work and that I have not used any aids and sources other than those indicated.
If electronic resources based on generative artificial intelligence were used in the course of writing this dissertation, I confirm that my own work was the main and value-adding contribution and that complete documentation of all resources used is available in accordance with good scientific practice. I am responsible for any erroneous or distorted content, incorrect references, violations of data protection and copyright law or plagiarism that may have been generated by generative artificial intelligence.

Hamburg, 10.09.2025

Lena Henneken

15 Acknowledgements

First and foremost, I would like to thank my doctoral supervisor Prof. Dr. Jan-Eric Turner for his support, input and scientific guidance. Your instructions, encouragement and also trust enabled me to successfully continue my thesis autonomously. Thank you for staying my supervisor despite not working at UKE anymore after the first half of my thesis was done and for supporting me in completing this project.

Equally important for the progress and finalisation of my thesis was Prof. Dr. Ulf Panzer. I feel grateful for the possibility to be part of the SFB1192 and for being able to work in an encouraging environment. Furthermore, I really appreciate the smooth and easy takeover from working group Turner to working group Panzer and the opportunity to continue working on my project. Thank you for the chance to discuss results and challenges at every time, for being open-minded to different ideas and for driving the project into a publication-worthy direction.

I also would like to express my gratitude to Prof. Dr. Tobias B. Huber for the possibility to perform my doctoral thesis in the III. Department of Medicine at UKE, to Prof. Dr. Wolfgang Streit for being a reviewer of my thesis and to Prof. Dr. Christian Krebs for critical questions and valuable input.

Furthermore, I want to appreciate all the people who made working in the lab very enjoyable. Nikhat, you know that I couldn’t have done it without you, thank you for endless lunch breaks, deep talks, listening to music on long days in the lab, laughing, crying and growing together. Thank you to Gini for teaching me a multitude of new techniques and for making me want to come to work every day and to Anna for your support, kind words and willingness to always help me. Both of you made the endless hours in the mouse barrier almost fun and definitely go by faster.
Thank you to Hajo for helping me with all my FACS-related questions, to Pauline for supporting me with all single-cell-related work and to Anett for not being annoyed by my endless questions regarding organisation, orders and everything in between.

Lastly, I would like to thank my family and friends. Anna, Anya, Lynn, Sebastian, Rixa and Audrey you made Hamburg feel like home, thank you for all the memories, fun

times and keeping me sane. Lina, Anni, Jana and Mara, thank you for 14 years of friendship and for always having my back.
Thank you to my parents and my sisters for your continuous reassurance, encouraging words, endless support and for making all of this possible.